

EXPLOSIVE BOILING FORCE OF A SINGLE DROPLET ON
SOLID HEATED SURFACES

EXPLOSIVE BOILING FORCE OF A SINGLE DROPLET ON
SOLID HEATED SURFACES

By DENNIS MOGHUL, B.Eng.Biosciences

A Thesis Submitted to the School of Graduate Studies in Partial
Fulfillment of the Requirements for the Degree Master of Applied
Science in Engineering Physics

McMaster University

© Copyright by Dennis K. Moghul, 2013

MASTER OF APPLIED SCIENCES (2013)
McMaster University (Engineering Physics)
Hamilton, Ontario, Canada

TITLE: Explosive Boiling Force of a Single
Droplet on Solid Heated Surfaces

AUTHOR: Dennis Moghul, B.Eng. Biosciences
(McMaster University)

SUPERVISOR: Dr. J. Luxat & Dr. M. Hamed
Department of Engineering Physics
McMaster University

NUMBER OF PAGES: xii, 119

Abstract

Explosive boiling is a phenomenon encountered in severe nuclear reactor accidents during quench cooling, core relocation or through fuel-coolant interactions. The mitigation of accident conditions is important from a safety standpoint since explosive boiling is potentially capable of destructive forces. Explosive boiling occurs when coolant water encounters a hot solid surface and absorbs a high degree of superheat. The resultant boiling mode is violent and features the rapid decomposition of liquid on a microsecond timescale with liquid atomization and ejection. In this study, the explosive boiling force of a single water droplet impacting hot solid surfaces was estimated with secondary droplet analyses using high-speed imaging.

A water droplet at 25°C with a Weber number of 432 impacted perpendicular to solid surfaces at temperatures from 30-700°C. Solid surfaces of copper, brass and stainless steel varied in thermal diffusivity from 3.48×10^{-6} to 1.17×10^{-4} m²/s. Curved and flat impact surfaces were also tested. Explosive boiling was most prominent when the instantaneous interface temperature attained the superheat limit temperature (300°C ±17°C). Maximum boiling force was encountered at the superheat limit with reduced force at surface temperatures in the nucleate boiling regime and near zero force in the film boiling regime. Thermal disintegration dominates over inertial break up of the droplet near the superheat limit region. Thermal diffusivity effects were only distinguishable in the 250-450°C region where increasing thermal diffusivity translated to larger boiling forces. Secondary droplet counts, size, trajectories were dependent on the boiling mode present at the interface with very strong variances caused by thermal break up of the initial droplet. Explosive boiling caused greater fragmentation creating more secondary droplets with smaller sizes and larger ejection trajectories. A curved surface showed slightly higher explosive boiling force in the superheat limit region but with negligible effects on secondary droplet properties.

Acknowledgements

My deepest thank you to Dr. John Luxat and Dr. Mohamed Hamed for their supervision and continued support during the duration of this work. The completion of this work could not have been possible without their guidance and advice during the research process.

I would like to thank the technicians at the Mechanical Engineering Student Workshops; Ron Lodewyks, Mark MacKenzie, Jim McLaren and Michael Lee, for their expertise and advice during the designing and construction of the experimental components.

I would like to thank Peter Jonasson of the Engineering Physics Department at McMaster University and Chris Keay at High Speed Imaging Inc. for their expertise with data acquisition systems.

I would like to thank my colleagues and peers in the Department of Engineering Physics and the Department of Mechanical Engineering at McMaster University.

Lastly, I would like to extend a special thank you to my family members, friends and lovely girlfriend for their continuous support and love throughout this project. This work is dedicated to them for the inspiration and motivation they have provided me.

Table of Contents

Abstract.....	iii
Acknowledgements.....	iv
Nomenclature.....	vii
List of Figures.....	ix
List of Tables.....	xii

Chapter 1: Introduction 1

1.1 Explosive Boiling in Nuclear Accidents.....	1
1.2 Droplet Impingement on a Solid Surface.....	2
1.2.1 Droplet Impact Regimes on Non-Heated Solid Surfaces	2
1.3 Heat Transfer Effects	4
1.3.1 Boiling Regimes	4
1.3.2 Thermal Diffusivity and Effusivity.....	6
1.3.3 Heat Transfer Effects on Droplets	8
1.4 Secondary Droplet Atomization from Explosive Boiling.....	10
1.4.1 Explosive Boiling	10
1.4.2 Secondary Droplet Characteristics.....	11
1.5 Objectives.....	13
1.6 Outline of Study	13

Chapter 2: Literature Review 15

2.1 Explosive Boiling Literature.....	15
2.2 Secondary Droplet Atomization Literature.....	17
2.2.1 Secondary Droplet Atomization Mechanisms and Thermal Effects	17
2.2.2 Secondary Droplet Atomization and Surface Variations.....	20
2.2.3 Secondary Droplet Atomization Correlations.....	22
2.3 Comments on Literature	23

Chapter 3: Experimental Setup and Methodology 25

3.1 Experimental Setup.....	25
3.1.1 Specimens	26

3.1.2	Holder System.....	29
3.1.3	Water Valve and Controller.....	30
3.1.4	High-Speed Camera and Data Acquisition System.....	31
3.2	Test Procedure	32
3.3	Key Parameters and Equipment Uncertainties	33
Chapter 4: Visual Image and Temperature Raw Data Observations.....		35
4.1	Visual Description of Images.....	35
4.1.1	High-Speed Camera Images	35
4.1.2	Image Processing	37
4.1.3	Estimation of Secondary Droplet Properties	39
4.2	Temperature Transient Description	41
4.2.1	Thermocouple Response Time	41
4.2.2	Droplet Impact Cooling Profile	42
4.2.3	Heat Flux Estimation	43
Chapter 5: Results and Discussion		46
5.1	Surface Temperature Regions of Explosive Boiling	46
5.1.1	Spontaneous Nucleation Temperature.....	46
5.1.2	Leidenfrost Temperature.....	48
5.2	Impact Morphology	49
5.2.1	Effect of Surface Temperature.....	49
5.2.2	Effect of Thermal Diffusivity	61
5.2.3	Effect of Surface Shape	67
5.3	Explosive Boiling Force	69
5.3.1	Propagation of Uncertainties in Estimates.....	72
5.3.2	Effect of Surface Temperature.....	73
5.3.3	Effect of Thermal Diffusivity	76
5.3.4	Effect of Surface Shape	80
5.4	Explosive Boiling On Secondary Droplet Characteristics.....	81
5.4.1	Secondary Droplet Count.....	81
5.4.2	Secondary Droplet Size	84
5.4.3	Secondary Droplet Distribution.....	87
Chapter 6: Conclusions		91

Chapter 7: Recommendations	93
Bibliography	95
Appendix A	100
A1: Image Processing	100
A2: Experimental Equipment Details	100
A3: Specimen Holder System Drawings	102
Appendix B – Raw Data	103
Appendix C – Uncertainty Analysis	107
C1: Temperature	107
C2: High-Speed Imaging and Processing	108
C3: Explosive Boiling.....	111
C4: Repeatability Analysis	112
Appendix D – Thermal Penetration Depth.....	115

Nomenclature

a	Acceleration [m/s^2]
A	Area [m^2]
C_p	Heat Capacity [$\text{J/kg}\cdot\text{K}$]
D	Droplet diameter [m]
F	Force [N]
h_{fg}	Latent heat of vapourization [J/kg]
k	Thermal conductivity [$\text{W/m}\cdot\text{K}$]
m	Mass [kg]
m_{vap}	Vapour mass [kg]
\dot{m}_L	Mass flux of liquid [$\text{kg/m}^2\cdot\text{s}$]
\dot{m}_V	Mass flux of vapour [$\text{kg/m}^2\cdot\text{s}$]
Q	Energy [W/m^2]
q''	Heat flux [W/m^2]
t	Time [s]
t^*	Droplet residence time [s]
T	Temperature [$^{\circ}\text{C}$]

$T_{Leidenfrost}$	Leidenfrost temperature [$^{\circ}\text{C}$]
v	Velocity [m/s]
V	Volume [m^3]
We	Weber number
x	Distance [m]
α	Thermal diffusivity [m^2/s]
ϵ_d	Droplet thermal effusivity [$\text{kg/K}\cdot\text{s}^{5/2}$]
ϵ_s	Surface thermal effusivity [$\text{kg/K}\cdot\text{s}^{5/2}$]
μ	Viscosity [$\text{N}\cdot\text{s}/\text{m}^2$]
ρ	Density [kg/m^3]
σ	Surface tension [N/m]

Subscripts

1	Before-impact
2	Post-impact
avg	Average
c	Critical
CHF	Critical Heat Flux
d	Droplet
$evap$	Evaporation
f	Final
i	Initial
int	Interface
liq	Liquid
s	Specimen surface
sat	Saturation
sl	Superheat limit
sv	Superheated vapour
vap	Vapour
w	Wall

Acronyms

CANDU	Canada Deuterium Uranium
CCD	Charge Coupled Device
CMOS	Complementary Metal Oxide Semiconductor
DAQ	Data Acquisition System
FCI	Fuel-Coolant Interaction
fps	Frames Per Second
LWR	Light Water Reactor
tiff	Tagged Image File Format
PDA	Phase Doppler Anemometry

List of Figures

Figure	Description	Page #
Figure 1	Typical boiling curve for water at 1 atm	4
Figure 2	Droplet impact regimes on a heated solid surface	8
Figure 3	Schematic of major components of the WQF	25
Figure 4	Main components of the water quench facility	26
Figure 5	Schematic of typical specimen dimensions	27
Figure 6	Specimen holder with a copper hemisphere	29
Figure 7	Support rod on a moveable track	29
Figure 8	Water valve and water reservoir supported above the metal specimen	30
Figure 9	Droplet impact sequence of a curved brass surface at a surface temperature of $T_s = 250^\circ\text{C}$	36
Figure 10	Boiling effects on droplet illumination for a curved brass surface	36
Figure 11	Image processing of a raw image to visualize droplet impacts	38
Figure 12	A cooling profile of a curved brass surface at $T_s = 250^\circ\text{C}$ with droplet at $T_d = 25^\circ\text{C}$	42
Figure 13	Heat flux of various surfaces into the droplet	44
Figure 14	Instantaneous interface temperatures for various surfaces	47
Figure 15	Water droplet impact on curved brass surface at $T_s = 30^\circ\text{C}$	49
Figure 16	Water droplet impact on a curved brass surface at $T_s = 100^\circ\text{C}$	50
Figure 17	Water droplet impact on a curved brass surface at $T_s = 150^\circ\text{C}$	51
Figure 18	Water droplet impact on a curved brass surface at $T_s = 200^\circ\text{C}$	52
Figure 19	Water droplet impact on a curved brass surface at $T_s = 250^\circ\text{C}$	53
Figure 20	Water droplet impact on a curved brass surface at $T_s = 300^\circ\text{C}$	54
Figure 21	Water droplet impact on a curved brass surface at $T_s = 350^\circ\text{C}$	55
Figure 22	Water droplet impact on a curved brass surface at $T_s = 400^\circ\text{C}$	57

Figure 23	Water droplet impact on a curved brass surface at $T_s = 500^\circ\text{C}$	57
Figure 24	Water droplet impact on a curved brass surface at $T_s = 550^\circ\text{C}$	58
Figure 25	Water droplet impact on a curved brass surface at $T_s = 600^\circ\text{C}$	59
Figure 26	Water droplet impact on a curved brass surface at $T_s = 700^\circ\text{C}$	60
Figure 27	Water droplet impacts on various heated surfaces at $T_s = 150^\circ\text{C}$	62
Figure 28	Water droplet impacts on various heated surfaces at $T_s = 250^\circ\text{C}$	62
Figure 29	Water droplet impacts on various heated surfaces at $T_s = 300^\circ\text{C}$	63
Figure 30	Water droplet impacts on heated surfaces at $T_s = 400^\circ\text{C}$	63
Figure 31	Water droplet impacts on heated surfaces at $T_s = 500^\circ\text{C}$	65
Figure 32	Water droplet impacts on heated surfaces at $T_s = 600^\circ\text{C}$	66
Figure 33	Water droplet impacts on various heated surfaces at $T_s = 700^\circ\text{C}$	66
Figure 34	Water droplet impacts on curved and flat brass surfaces at $T_s = 150^\circ\text{C}$	68
Figure 35	Water droplet impacts on curved and flat brass surfaces at $T_s = 200^\circ\text{C}$	68
Figure 36	Explosive boiling force of a water droplet at $T_d = 25^\circ\text{C}$ impacting surfaces of copper, brass, and stainless steel at various initial temperatures	71
Figure 37	Error bars for estimated explosive boiling force of a water droplet on various surfaces	73
Figure 38	Secondary droplet visualization on a copper surface at surface temperatures	74
Figure 39	Explosive boiling force as a function of thermal diffusivity for the most energetic boiling surface temperatures	76
Figure 40	Explosive boiling force as a function of thermal diffusivity for the surface temperatures with decreased boiling intensity	77
Figure 41	Linear regression line fit plot	78

Figure 42	Image processed sequences of droplet explosion on various heated surfaces at $T_s = 300^\circ\text{C}$ with varying thermal diffusivity	79
Figure 43	Image processed sequences of droplet explosion on various heated surfaces at $T_s = 500^\circ\text{C}$ with varying thermal diffusivity	80
Figure 44	Maximum secondary droplet counts for various surfaces	82
Figure 45	Comparison of secondary droplet counts between various surfaces	84
Figure 46	Average secondary droplet diameters as a function of surface temperature for surfaces	85
Figure 47	Error bars for average secondary droplet diameters for various surfaces	86
Figure 48	Average secondary droplet diameters in the superheat limit region for various hemisphere surfaces	87
Figure 49	Average vertical secondary droplet ejection height as a function of surface temperature for various surfaces	88
Figure 50	Average horizontal distribution of secondary droplets ejected from various surfaces with surface temperature	88
Figure A.1	Design drawings of specimen holder system	102
Figure C.1	Histogram of detectable droplet sizes for surfaces	109
Figure C.2	Explosive boiling force of a water droplet with repeat measurements	113
Figure D.1	Heat conduction in a semi-infinite water droplet	115
Figure D.2	Temperature distribution in droplet for various initial surface temperatures	117
Figure D.3	Temperature distribution for different surfaces and absorption times ($T_s = 300^\circ\text{C}$, SS – Stainless Steel, Cu – Copper)	118

List of Tables

Figure	Description	Page #
Table 1	Summary of droplet impact regimes with temperature regions and Weber number	9
Table 2	Specimen material properties at 25°C	26
Table 3	Liquid water properties at 25°C	27
Table 4	Measurement uncertainty for experimental equipment	34
Table 5	Uncertainties of secondary droplet properties	40
Table 6	Leidenfrost temperature of water on various surfaces	48
Table A.1	Pixel to length ratios of objects in images analyzed by ImageJ	100
Table B.1	Copper hemisphere raw data	103
Table B.2	Stainless steel hemisphere raw data	104
Table B.3	Brass hemisphere raw data	105
Table B.4	Brass plate raw data	106

Chapter 1: Introduction

1.1 Explosive Boiling in Nuclear Accidents

Explosive boiling, also known as a vapour explosion, is the rapid vapourization and violent fragmentation of a liquid when it absorbs a high degree of superheat (Park, Byun, & Kwak, 2005). Superheating occurs when the liquid can be heated above its ambient boiling point without phase transition. Explosive boiling can be attained in situations where a sudden depressurization of a volatile liquid occurs or when a liquid encounters a much hotter surface. In industry, explosive boiling has been observed during the spillage of liquefied natural gases, metal smelting, and during nuclear reactor accidents. In nuclear reactor accidents, explosive boiling phenomena can occur during the late stages of severe core degradation accidents, quenching processes and in fuel-coolant interactions.

In severe accidents the heat transfer from the fuel is significantly impaired. This results in fuel dry out and causes the fuel to heat up leading to a loss of structural integrity of the core. With core temperatures rising, subsequent progression in the accident severity can then extend to core meltdown and relocation. In such a case, extremely high temperature melts the fuel ($>2840^{\circ}\text{C}$) and melts surrounding structures to form a molten mixture known as corium. Progressive failures occur as a result of the corium collapsing to the bottom of the vessel and contacting any coolant below resulting in extremely large vapour generation. Development of vapour can occur very rapidly (100 – 200 μs at atmospheric pressure) and may result in a steam explosion that could challenge containment barriers as well as cause the release of fission products. (Shusser & Weihs, 1999).

In scenarios where coolant water interacts with extremely hot fuel, known as fuel-coolant interactions (FCI), explosive boiling has significance due to the rapid and violent nature of vapour production. A rapid high-pressure pulse can be created and in confined spaces, the shock waves can fragment fuel thereby increasing the heat transfer rate of those fragments and worsen the accident severity (Kudryashov & Allen, 2006; Takashima, 2008).

From a nuclear safety perspective, an understanding of the explosive boiling energy produced during accident conditions is necessary for safety analysis methodology development. Explosive boiling encompasses several complex mechanisms in liquid-solid interactions, transient heat transfer, vapourization of superheated liquid, liquid atomization, fluid mixing, and multi-phase flow (Nguyen, Furzeland, & Iipelaar, 1998). In order to study rapid vapourization of liquids encountering hotter solid surfaces, small-scale experiments can be

selectively designed to remove complexities in fluid mixing and multi-phase flow. Therefore, single liquid droplet experiments on heated surfaces are an attractive area of study and also forms the basis of this present study.

The focus of this study is directed towards quantifying the explosive boiling energy by characterizing secondary droplets that are atomized when a single water droplet impinges normal to a solid heated surface. In order to understand the various mechanisms involved in explosive boiling from single droplet impacts, the following sections have been divided to discuss the major interactions: 1) single liquid droplet impacting a non-heated solid surface 2) heat transfer effects of a solid surface 3) explosive boiling and secondary droplet atomization.

1.2 Droplet Impingement on a Solid Surface

Using solid surfaces offers a clear demarcation of liquid boundaries upon contact and is advantageous for visualizing varying forms of boiling at the contact area. For solid surfaces, surface shape, temperature, roughness, wettability and material type influence droplet interactions.

In terms of the water droplet, its properties will influence the impact characteristics. These include its temperature, size, shape, impact angle, velocity, surface tension, viscosity and compressibility (Rein, 1993). The water droplet, during descent, can be subject to deformation and oscillations due to drag force of the air through which it travels. However, for simplicity, most calculations and theoretical models assume negligible drag effects on the droplet and assume a consistent spherical shape. The impact outcomes when a droplet impacts a solid non-heated surface will be discussed in the next section.

1.2.1 Droplet Impact Regimes on Non-Heated Solid Surfaces

Droplet impacts are characterized by their impact energy and are described by a dimensionless parameter called the Weber number. The Weber number relates a falling droplet's inertial energy to its surface tension and is shown in Equation (1).

$$We = \frac{\rho D v^2}{\sigma} \quad (1)$$

ρ is density of the fluid, D is the diameter of the droplet, v is the fall velocity, and σ is the fluid surface tension. Based on the impact energy or Weber number, three basic impact outcomes are identified: 1) sticking 2) spreading 3) splashing (Bernardin, Stebbins, & Mudawar, 1997; Rein, 1993).

1. Sticking

For very low impact energies or very low Weber numbers, a droplet will stick to a flat surface, only deforming at base of the liquid. The gentle deposition of the droplet on the surface occurs throughout the entire impacting process. Since surface tension dominates over inertial energy, the distorted spherical shape of the droplet is maintained indefinitely without droplet break up (Rioboo, Tropea, & Marengo, 2001).

2. Spreading

As the impact energy increases, the droplet will begin to spread on the surface and is characterized by the formation of the droplet into a thin, flat circular disk. The circular disk radially expands to a maximum diameter as the inertial energy dissipates by viscous forces (Rein, 1993). A recoil phase where the surface area of the spread disk contracts inwards on itself usually exists after the droplet spreads to a maximum diameter. Surface tension forces contract the droplet towards its center, eventually reaching an equilibrium state on the surface. Break up of the droplet may occur on the surface during the recoil phase since insufficient cohesion of the liquid exists due to reduced surface tension forces. Surface roughness affects the recoil break up as the liquid is unable to transverse the microscopic cavities of the surface (Bernardin et al., 1997). A special case exists when sufficient energy remains at the end of the recoil phase, the droplet will rebound. Rebounding is observed as a column of liquid originating from droplet center that jettisons vertically away from the surface then falls back down due to gravity (Rioboo et al., 2001).

3. Splashing

When the impact energy is very high, droplet break up is immediately seen after impact in which a portion of the liquid disintegrates into smaller droplets. This specific morphology is known as splashing. The kinetic energy is large and is conserved in a fashion that viscous forces do not cause it to dissipate. The defining characteristics of break up occurring from splashing compared to break up due to spreading are that smaller secondary droplets are ejected away from the bulk droplet in splashing. Rioboo et al. (2001) have established two types of splashing; prompt splash and corona splash in their research. A prompt splash occurs at the beginning of the spreading phase where secondary droplets are released right at the liquid-solid interface. A corona splash occurs towards the end of the spreading phase in which secondary droplets are ejected from the outer rim of the spreading liquid (Rioboo et al., 2001).

1.3 Heat Transfer Effects

The addition of heat transfer effects from a solid surface in which a droplet impinges adds greater complexities in the observed impact characteristics. Upon liquid-solid contact, an instant thermal gradient is established that draws heat from the surface and is deposited into the liquid. As a result, the hydrodynamic interactions between the droplet and the solid surface are altered. In order to understand the role of surface temperature in droplet impacts, attention is given to varying modes of boiling at the liquid-solid interface. Looking at a boiling curve will help characterize different heat transfer regimes that can exist.

1.3.1 Boiling Regimes

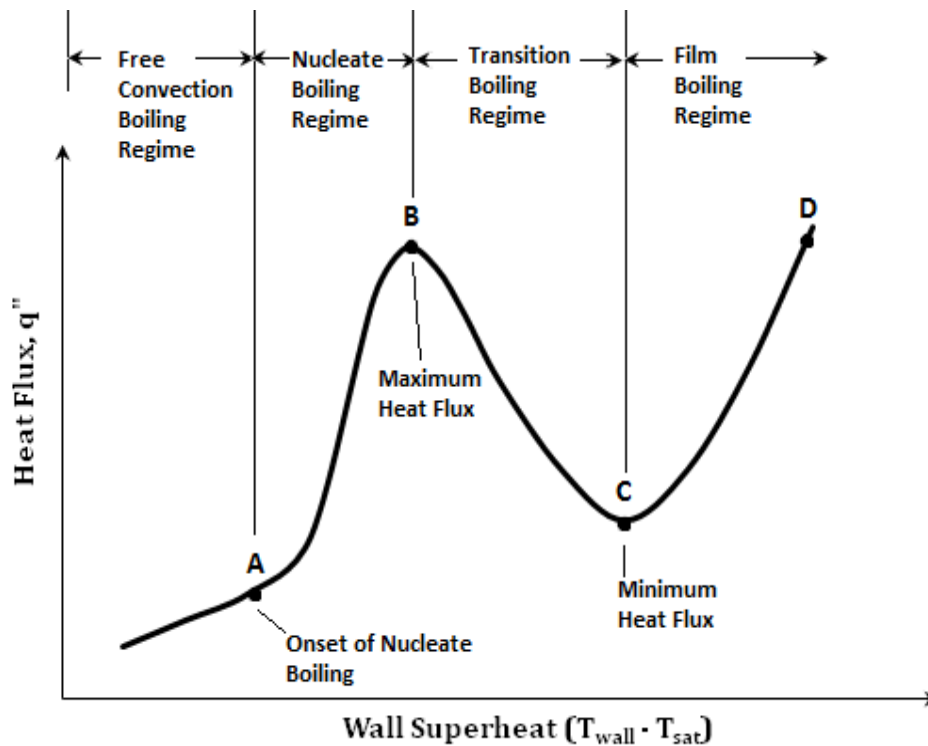


Figure 1 – Typical boiling curve for water at 1 atm

Figure 1 depicts a typical pool boiling curve for water at 1 atm residing on a heated surface. The curve is plotted with the surface heat flux, q'' , as a function of wall superheat temperature. Different boiling regimes are marked according to wall superheat are:

1. Free Convection Boiling

In this region, heat transfer occurs predominately from conduction and free convection in which the liquid heats up without phase change. This occurs up to wall temperatures slightly above the liquid's saturation temperature to point A (the onset of nucleate boiling).

2. Nucleate Boiling

The nucleate boiling region is defined by point A (the onset of nucleate boiling) to point B (critical/maximum heat flux). This regime is noted for its high heat transfer rates resulting from small changes in surface temperature that dramatically increase the heat flux. In this region, microscopic surface cavities provide nucleation sites from which vapour bubbles evolve and detach from the surface. As the surface temperature increases towards the maximum heat flux point, more nucleation sites become active and increased vapour bubble formation leads to the coalescence of larger bubbles. This nucleation type is known as heterogeneous nucleation and is characterized by multiple vapour bubbles arising from surface impurities containing gas pockets (Blander & Katz, 1975). Homogeneous nucleation is a process where a single vapour nucleus grows within a metastable superheated liquid (Shusser et al., 1999). This nucleation type can be achieved when heterogeneous nucleation is suppressed. However, it is rarely seen independently on its own in liquid-solid surface type interactions. Finally, the maximum heat flux is a point where vapour production significantly begins to reduce the liquid's ability to wet the surface.

3. Transition Boiling

The transition boiling regime is the region between point B and point C. Here, bubble formation is so rapid that a vapour layer unstably blankets the surface from the liquid. The instability of the vapour layer is due to the intermittent wetting the surface. Since the thermal conductivity of the vapour layer is less than that of the liquid, the heat flux decreases towards point C, known as the minimum heat flux point or the Leidenfrost point.

4. Film Boiling

Film boiling exists beyond the minimum heat flux point (Point C). This point represents the onset of stable film boiling where the surface temperature is hot enough to maintain a vapour layer that insulates the surface from the liquid. As the surface temperature increases, so too does

the vapour layer thickness. Heat transfer from the surface to liquid occurs by conduction and radiation through the vapour layer. As surface temperature is increased, the radiation component becomes significant and results in the increase of the heat flux.

1.3.2 Thermal Diffusivity and Effusivity

The heat transfer rate from a hot solid surface into a droplet is governed by thermophysical properties, namely the thermal diffusivity and thermal effusivity.

Thermal diffusivity, α , is given in Equation (2) as the ratio of thermal conductivity, k , to the volumetric heat capacity (product of the density, ρ , and the heat capacity, C_p).

$$\alpha = \frac{k}{\rho C_p} \quad (2)$$

Thermal diffusivity measures the rapidity at which a material is able to propagate thermal energy relative to its ability to store it (Incropera & DeWitt, 2002). Thermal diffusivity represents a material's thermal inertia where a high thermal diffusivity means a material will respond quickly to temperature fluctuations while materials with low thermal diffusivity will take longer to reach a new equilibrium (Incropera et al., 2002; Cossali, Marengo, Santini, & Fest, 2006).

Thermal effusivity, ε , is given by Equation (3) as the square root of the thermal conductivity, density and heat capacity.

$$\varepsilon = \sqrt{k\rho C_p} = \frac{k}{\sqrt{\alpha}} \quad (3)$$

Thermal effusivity describes the ability of a material to exchange thermal energy with the surroundings. Thermal effusivity is a relevant parameter used in droplet impacts due to its influence on the transmittance of thermal energy through an interface that is established upon liquid contact with a heated surface (Sreekumar & Vaidyan, 2007). At the instant a droplet contacts a heated surface, a thermal gradient is established where the surface temperature of the heated solid undergoes a stepwise change. Solving the homogeneous heat diffusion equation and by applying Fourier's law of conduction for a semi-infinite solid, the heat flux at the surface of the solid is given by Equation (4).

$$q'' = \frac{k(T_{sf} - T_{si})}{\sqrt{\pi\alpha t}} \quad (4)$$

k is the solid surface thermal conductivity, T_{sf} is the final surface temperature after droplet impact, T_{si} is the initial surface temperature, α is the surface thermal diffusivity, and t is the time duration of the temperature drop. Equation (4) can be written in terms of thermal effusivity by using Equation (3) (Marin, 2007).

$$q'' = \frac{\varepsilon(T_{sf} - T_{si})}{\sqrt{\pi t}} \quad (5)$$

Equation (5) shows that the heat flux at the surface of the solid material is proportional to its thermal effusivity. Consider that both the droplet and the solid surface are semi-infinite solids, at T_d and T_s respectively where ($T_s > T_d$), and contact each other at $t = 0$ with negligible contact resistance. There is a mutual interface temperature, T_{int} , for which both surfaces assume upon contact where $T_d < T_{int} < T_s$ (Fujimoto, Oku, Ogihara, & Takuda, 2010; Incropera et al., 2002; Marin, 2007). From Equation (5), the heat flow from the hotter solid surface equals the heat flow into the water droplet. Rearranging for the interface temperature yields Equation (6) with ε_s and ε_d as the thermal effusivities of the surface and droplet respectively (Incropera et al., 2002; Marin, 2007).

$$T_{int} = \frac{T_s \varepsilon_s + T_d \varepsilon_d}{\varepsilon_s + \varepsilon_d} \quad (6)$$

In terms of water droplet impacts with solid heated surfaces, the above equations have specific roles in heat transfer during different stages of the impact. From Equations (5) and (6), the thermal effusivity is the relevant thermophysical property that governs heat transport through the liquid-solid interface at the instant of contact (Sreekumar & Vaidyan, 2007). Thermal effusivity determines whether the instantaneous interface temperature will approach the initial solid surface temperature or the initial droplet temperature more. In Section 5.1, the interface temperature will be used to establish temperature regions where spontaneous nucleation is most likely to occur in a droplet-surface combination.

Upon establishment of the thermal gradient, the heat transfer rate within the solid surface and the droplet are governed by the thermophysical property of thermal diffusivity. Both the thermal diffusivity and thermal effusivity are important parameters that define the boiling regime that is expected to occur in the liquid upon contact with the surface. The next section will discuss common droplet impact morphologies observed when heat transfer effects are considered.

Since the driving force of heat transfer to the droplet is due to the presence of a temperature gradient, thermal diffusivity is a more relevant parameter to use in thermal energy transfer than thermal effusivity. The heat diffusion equation utilizes thermal diffusivity as well, and thus it is an appropriate choice to describe the heat inertia within a test specimen's body. In order to study explosive boiling in this present study, the initial water droplet temperature is fixed, meaning that the droplet thermal diffusivity will be held constant. Variances in the solid surface thermal diffusivity on explosive boiling will be studied by varying the surface material type.

1.3.3 Heat Transfer Effects on Droplets

With the introduction of heat effects on impinging droplets, the surface temperature becomes a key influencing parameter, along with the droplet impact velocity in characterizing droplet impacts. The temperature dependence of parameters such as surface tension and viscosity alter droplet impact outcomes. Several authors have studied droplet impacts on heated surfaces and their results have been characterized as a generalized impact regime map in **Figure 2** (Akhtar & Yule, 2001; Fujimoto et al., 2010; Rein, 1993; Rioboo et al., 2001; Wang, Lin, & Cheng, 2005).

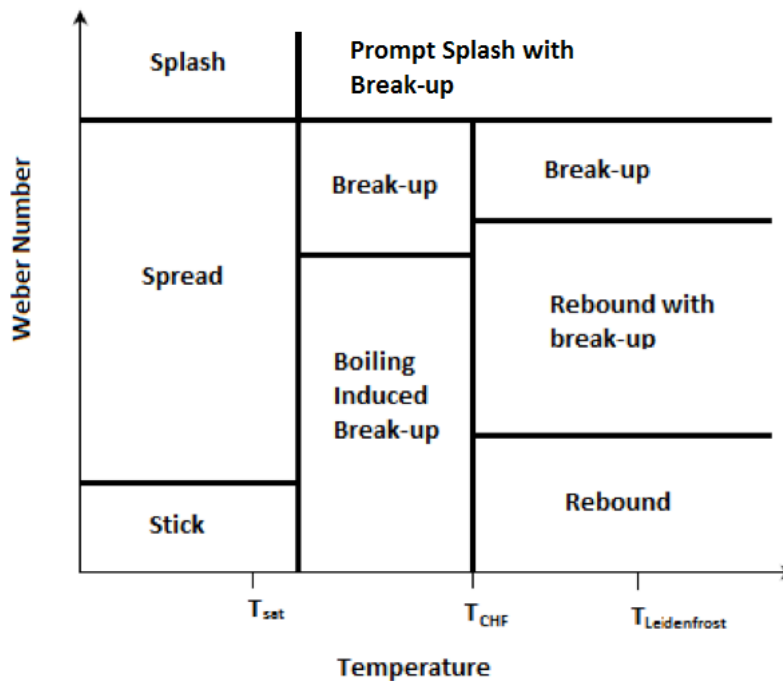


Figure 2 – Droplet impact regimes on a heated solid surface

Due to variations in the experimental conditions between the authors, defining a unified threshold between the different impact regimes with respect to Weber number and surface temperature is difficult. Summaries of the studies that make up **Figure 2** are presented below in **Table 1**¹.

Table 1 – Summary of droplet impact regimes with temperature regions and Weber number

Study	Experimental Conditions	Temperature Region	Weber Number
Wahcters & Westerling (1966)	- Water droplet, diameter = 2-3 mm - Gold dry surface - Impact angle at 60°	Film boiling $T_s > 400^\circ\text{C}$	- Spreading & rebound: $We < 30$ - Rebound & break-up: $30 < We < 80$ - Splashing from rim with break-up: $We > 80$
Araki & Moriyama (1982)	- Water droplet, diameter = 1.8-4.5 mm - Dry surface of copper & stainless steel - Impact angle at 90°	Film boiling $T_s > 500^\circ\text{C}$	- Spreading & rebound: $We < 60$ - Rebound & break-up: $60 < We < 100$ - Splashing from rim with break-up: $We > 100$
Akhtar et al., 2001	- Water droplet, diameter = 20-160 μm - Dry surface of stainless steel	Near critical heat flux $T_s = 140-160^\circ\text{C}$	- Stick: $We < 15$ - Spread: $20 < We < 300$ - Break-up: $We > 300$
		Transition Boiling $T_s = 160-200^\circ\text{C}$	- Rebound: $We < 15$ - Boiling induced break-up: $20 < We < 60$
		Film Boiling $T_s = 260-400^\circ\text{C}$	- Break-up: $60 < We < 350$ - Prompt splash: $We > 350$

In the single phase heating regime (up to and slightly above T_{sat}) the mechanisms of droplet impact are similar to those occurring on the non-heated solid surface impact scenario. Rebounding is a droplet impact phenomena characterized at high temperatures above the maximum heat flux. An immediate vapour layer is created at initial droplet-surface contact which functions as a cushion to which the droplet kinetic energy is dissipated in. The compression of the vapour layer acts as a spring and catapults the droplet upwards from the surface. The mechanisms that support spreading and splashing of a droplet is also observed in the film boiling regime where such phenomenon occurs atop a vapour layer.

¹ Table collated by Moreira, Moita, & Pano (2010)

The phenomenon of droplet break up is one where the initial droplet disintegrates into smaller secondary droplets. It is observed for surface temperatures above the onset of nucleate boiling extending into transition and film boiling regimes for a large range of Weber numbers. Boiling induced break up is the result of the formation and collapse of vapour bubbles. The aggregating force of tiny vapour bubbles as they collapse when reaching the liquid surface is responsible for tearing the liquid layers and creating smaller droplets from the initial one. The break up of a liquid that ejects smaller secondary droplets from the surface from boiling effects is known as secondary droplet atomization or thermal atomization. Secondary droplet atomization is the most explosive and violent in a region known as the superheat limit of the liquid. The next section will describe vapour explosions and secondary droplets atomization in detail.

1.4 Secondary Droplet Atomization from Explosive Boiling

1.4.1 Explosive Boiling

Explosive boiling is most commonly observed when the liquid-solid interface temperature is in the range of the superheat limit but below the critical temperature (Inada & Yang, 1996). The superheat limit of a liquid, at constant pressure, represents the highest attainable temperature below the critical point that a liquid can achieve without undergoing a phase transition (Avedisian, 1985). Several authors; Avedisian 1985, Shepherd & Sturtevant 1982, and Glod, Poulikakos, Zhao, & Yadigaroglu, 2002; estimated the superheat limit of water at atmospheric pressure to be ~10% below the critical temperature ($T_{critical} = 374^{\circ}\text{C}$). They estimated it to be from 283-313°C.

In this boiling mechanism, molecular density fluctuations create nuclei and a rapid phase change occurs where the evaporative fluxes and fluid acceleration is far greater than normal boiling modes (Yushen, Zhilgilei, Winograd, & Garrison, 2001). Morphologically, an explosive boiling event features the rapid disintegration of liquid that atomizes smaller liquid droplets that project outwards with great velocity. Explosive boiling of a liquid droplet as discussed in this current study is a physical explosion due to boiling effects and phase change.

The mechanism of bubble nucleation influences the phase change of a liquid and forms a basis of understanding explosive boiling. The classical theory of homogenous bubble nucleation developed by Blander et al. (1975) qualitatively described the initiation of growth of vapour bubble nuclei in a liquid. In order for a liquid to vapourize and support vapour bubble growth, a vapour nucleus must attain a critical size by overcoming an energy barrier. A minimum work formation of the bubble is required to sustain its growth and achieve a critical size.

In heterogeneous nucleation, vapour nuclei are created at the interface of the liquid and solid from microscopic surface cavities. As the temperature of surface increases, more nucleation sites are activated from which bubbles are created. This is because increasing the temperature provides vapour nuclei a greater amount of energy to attain a critical size. In homogeneous nucleation, vapour bubbles are created spontaneously within the bulk liquid (Shepherd et al., 1982). The bubble nucleation rate exhibits an exponential relationship with respect to temperature (Reid, 1983). The study by Reid (1983) showed the sensitivity of this relationship. The example demonstrated that 1 m³ of ethyl ether at 137°C would result in an average wait time of 10²¹ years to observe a vapour bubble to nucleate. If the temperature was increased to 147°C, then the average wait time becomes 10⁻¹⁴ s. For a liquid that experiences such a rapid nucleation rate, phase change is considered spontaneous and explosive boiling is an inevitable result. However, in the context of liquid droplets on heated solid surfaces, heterogeneous nucleation is unavoidable. Both heterogeneous and homogeneous nucleation can occur in a liquid that explosively boils at the superheat limit.

The theory by Blander et al. (1975) helped establish early characteristics and morphology of explosive boiling. The rupture process of a liquid droplet was driven by large amplitude roughening of the vapour bubble surface. This roughening phenomenon is a result of the bubble oscillating with a violent acceleration such that it breaks up under Rayleigh-Taylor instabilities (Shepherd et al., 1982).

Early experiments quantifying explosive boiling characteristics involved suspending a volatile test liquid in another non-volatile host liquid. This condition was ideal since heterogeneous nucleation could be suppressed in favour of homogeneous nucleation to induce explosive boiling at the superheat limit. It also meant that evaporation rates or homogeneous bubble nucleation rates could be measured with fewer complications. Through a review of literature, much of the studies have used bubble columns, pulse heating methods or rapid decompression to induce and study explosive boiling. Another method to study explosive boiling has recently emerged by analyzing secondary droplet formation after a droplet explosively boils. This interaction is characteristic of when a cooler liquid droplet suddenly contacts a hot surface. Atomization characteristics of secondary droplets can infer the evaporative fluxes or the explosive forces produced when a droplet comes in contact with a hot surface. This will be discussed in the next section.

1.4.2 Secondary Droplet Characteristics

A defining characteristic of explosive boiling is that rapid atomization creates a large number of smaller sized droplets. The nature of the break up of the droplet

influences secondary droplet formation. In other words, secondary droplet formation is strongly dependent on surface temperature and impact velocity. As a result, the intensity explosive boiling can be studied in terms of secondary droplet production. Several authors have focused on analyzing secondary droplet production by studying their properties, most commonly their count, size, velocity and distribution area.

Varying Surface Temperature

In the nucleate boiling regime, initial droplet disintegration occurs by the bursting of vapour bubbles at the liquid-solid interface. Vapour pressure forces disrupt the balance between the surface tension and viscous forces with the inertial forces (Moita & Moreira, 2009). Studies by Moita et al. (2009) showed that the initiation of secondary droplet atomization was influenced by a liquid's surface tension and latent heat of vapourization. Liquids with low surface tension and heat of vapourization atomized quicker than liquid's with larger values. The cohesive forces of the droplet are reduced when the surface tension is smaller and therefore droplet atomization is more likely to occur. As the surface temperature is increased in the nucleate boiling regime, surface tension decreases while superheating increases, contributing to more violent phase change leading to greater atomization and more forceful ejection of secondary droplets (Cossali, Marengo, Santini, & Watanabe, 2002; Moita et al., 2009). With surface temperature increases, secondary droplet counts have been reported to increase while their sizes (diameters) decrease (Cossali et al., 2002; Moita et al., 2009; Richter, Dullenkopf, & Bauer, 2005). The evolution of a vapour layer from film boiling results in secondary droplets decreasing in count and increases the probability of droplets with flatter trajectories (Moita et al., 2009).

Secondary droplet atomization is expected to be the most violent at the early instants of initial droplet impact with the surface near the superheat limit, where explosive boiling is most likely (Moreira & Moita, 2007). As a result, secondary droplet production is expected to be the highest due to the rapid liquid break up. The analysis of secondary droplet properties and formation is often overlooked in the region where explosive boiling is concerned, and is therefore necessary to investigate.

Varying Surface Thermal Diffusivity

In droplet interactions, the thermal diffusivity of the hot solid surface will dictate the heat deposition rate into the droplet and influence atomization characteristics. For high thermal diffusivity surfaces the heat transfer rate into the droplet will occur more rapidly and therefore quicker initiation of nucleate boiling or stable film boiling is expected to occur at a given surface temperature. The timescale of heat deposition due thermal diffusivity variances will also effect secondary

droplet formation. Increasing thermal diffusivity of a solid surface will drive more energetic secondary droplet atomization resulting in secondary droplet sizes to decrease (Cossali et al., 2006). The influence of thermal diffusivity also extends to other secondary droplet properties including count and escape trajectories. Limited studies have investigated surface thermal diffusivity effects on secondary droplet properties that span large surface temperature variations. These effects will also be investigated and discussed in this study along with the atomization force responsible for secondary droplet formation.

1.5 Objectives

Studies of secondary droplet atomization on heated surfaces primarily have focused on characterizing mechanisms of secondary droplet evolution and secondary droplet characteristics including droplet count, diameter, and ejection distribution. The Literature Review section will discuss these studies in detail.

Limited attempts have been made to utilize secondary droplet formation to quantify the intensity of explosive energy of droplet impacts with a heated surface. Specifically, estimating the explosive force with respect to surface temperature and surface material type is necessary. The objective of this experimental study is to contribute knowledge towards explosive boiling phenomena of water droplets impacting heated solid surfaces by accomplishing the following:

- Experimentally measure surface temperature of a solid surface during droplet impacts. The temperature data will be used to determine heat flux into a droplet and define boiling regimes.
- Visualize explosive boiling and secondary droplet characteristics when a droplet impacts a heated surface using a high-speed camera.
- Develop a model to describe the explosive energy during vapour explosions in terms of force from data obtained on secondary droplet properties.
- Analyze secondary droplet counts, size, distribution and acceleration, and their variance with surface temperature and material type (varying thermal diffusivity) using imaging software.

1.6 Outline of Study

This dissertation contains the following chapters pertaining to explosive boiling and secondary droplet atomization.

Chapter One: Introduction – Background information is given on the explosive boiling energy and its relevance to nuclear reactor accidents. Definitions and descriptions of the main influencing parameters on explosive boiling and secondary atomization are given. The objectives of this study are also identified.

Chapter Two: Literature Review – A review of studies focusing on the quantification and description of explosive boiling and secondary droplet atomization.

Chapter Three: Experimental Setup and Methodology – Description of the experimental components and design are given in this section. Specifications of the materials, operating conditions, and the desired data obtained are outlined. A procedure to obtain the measurements of interest is given with measurement uncertainties.

Chapter Four: Visual Image and Temperature Raw Data Observations – The description of the raw data and how it was processed is outlined for the high-speed camera images and temperature measurements.

Chapter Five: Results and Discussion – This section includes screen shots and analysis of trends with supporting discussion. Interfacial temperatures, morphological analyses, explosive boiling force estimation and secondary droplet characteristics are presented.

Chapter Six: Conclusions – The main conclusions in this study are reported.

Chapter Seven: Recommendations – Future considerations for improving and extending the current study are given.

Appendix – Details on the experimental components, raw data tables, uncertainty analyses, and thermal distribution profiles are presented.

Chapter 2: Literature Review

In this chapter, the literature review will cover research involving the characterization and quantification of 1) explosive boiling energy and 2) secondary droplet atomization. Focus was given towards experimental studies, however studies that performed simulations and developed empirical correlations are also addressed.

2.1 Explosive Boiling Literature

Yushen et al. (2001) provided a microscopic description and simulation of the water film at a solid surface during explosive boiling by using a gold surface heated to 1000K and thicknesses of water molecule layers of 528 – 2112 molecules. Stationary bulk water layers resided over a plate that was rapidly heated. It was shown that the water molecules closest to the surface are at explosive boiling temperature while the molecules at the top were only at the saturation temperature. The molecules at the surface undergo rapid phase explosion and provides the acceleration for moving water molecules in the top layers outwards from the surface. The ejection velocity of the upper water molecule layers decreased as the initial thickness of water molecules residing on the surface before phase explosion increased. This study showed that the initial water thickness on a heated surface limits the force at which explosive boiling contributes to the outward ejection of secondary droplets.

The experimental study by Nematollahi (2008) is notable for its similarity to this present study with a setup congruent with fuel rod orientation in a Light Water Nuclear Reactor (LWR). The study characterized the intensity of explosive boiling on a heated surface by estimating its force. The experimental setup featured a long, thin rod of stainless steel (diameter = 10 mm, length = 50 cm) vertically oriented in a column through which coolant water was passed. The coolant temperature was varied from 25-75°C, the coolant velocity varied from 0.16-0.53 m/s and the linear power rating of the rod varied from 100-600 W/cm. An estimated force of 10^{-4} N was created per vapour bubble as it was formed. The force increased with bubble size. The rate of vapour bubble formation and the bubble size increased and decreased respectively when the power rating was higher or when the coolant subcooling was decreased. Importantly, this study only considered the force associated with vapour bubble growth and did not include the force resulting from vapour bubble collapse (rupture). It is the collapsing force that is of interest as well and requires quantification since it contributes to the blow out and ejection of secondary droplets.

The study by Zhao, Glod, & Poulidakos (2000) quantified explosive boiling during the growth and collapsing phases of vapour bubbles in terms of measuring an acoustic pressure wave that was emitted when a vapour layer expands rapidly. A thin-film microheater ($100\ \mu\text{m} \times 110\ \mu\text{m} \times 1\ \mu\text{m}$) resided under a layer of water. The surface was heated rapidly in $6\ \mu\text{s}$ by an electrical pulse varying in voltage from 19-37V (representing a surface temperature from the onset of explosive boiling to the maximum explosive boiling scenario). The acoustic pressure waves were recorded with a pressure transducer. A positive pressure was generated as the vapour bubbles grew to a maximum size and represented the highest acceleration and growth of the vapour layer. The pressure then decreased to a minimum point as vapour growth decelerated. About $5\ \mu\text{s}$ after growth stopped, the vapour bubble ruptured and smaller vapour bubbles remained on the heated surface. The author reported higher peaks and deeper troughs of the pressure wave occurring at earlier times as the microheater pulse heat was increased. The intensity of explosive boiling was higher and occurred quicker as the surface temperature was increased. In the highest surface temperature, the vapour bubble growth front reached a maximum velocity of 17 m/s. An increase in 15% above the minimum temperature for the onset of explosive boiling generated a 500% increase in the acoustic pressure wave.

Similarly, a study by Park et al. (2005) also measured the acoustic pressure waves generated during explosive boiling. This study used single droplets of hydrocarbons that boiled explosively in a heated column of a denser host liquid of glycerin. Similar acoustic pressure wave patterns were observed much like the study by Zhao et al. (2000). Pressure wave dampening occurred meaning that after the first explosive boiling event where smaller droplets were produced from break up underwent subsequent explosive boiling again. It is interesting to note whether this researcher uniquely obtained explosive boiling of smaller secondary droplets or if it is a phenomenon that also occurs in droplet impacts with solid heated surfaces.

The study by Zhilin, Zeigarnik, Ivochkin, Oksman, & Belov (2009) not only quantified pressure waves from explosive boiling but also included surface material conductivity effects. Relevance can be drawn from the work of Zhilin et al. (2009) to this present study since focus is given to the thermal properties of the surface. Zhilin et al. (2009) used a 10 mm diameter cylindrical rod with a hemispherical end surface that was heated to 500°C and submerged in a water bath to visualize and record pressure waves of explosive boiling. The pressure waves occurred from the collapse of vapour in stable film boiling. A pressure fluctuation of up to 1 MPa could be attained during an explosive boiling event. The surface material was also varied in thermal conductivity where copper was the highest, then brass, and the lowest with stainless steel. The study noted that a high thermal conductivity material has more thermal inertia and therefore resists the change in boiling modes more than a lower thermal conductivity material. The

high conducting material promoted quicker transition into different boiling modes or in other words the quicker progression from film boiling to nucleate boiling occurred. The conclusions drawn from this study will be adapted towards the results and discussion section in this present study.

Explosive boiling energy can often be quantified in terms of the vapour bubble nucleation rate. The study by Glod et al. (2002) used acoustic pressure wave data to estimate the nucleation rate of vapour bubbles close to the superheat limit where explosive boiling occurred. The experiments featured a thin platinum wire that was submerged in a pool of water with a fill height of 80 mm. A short and intense current was applied to the platinum wire that heated it to a maximum temperature of 400°C. The pressure measurements were used to develop an upper limit to the superheating rate as well as the maximum attainable homogeneous nucleation rate. The study showed that superheating was initiated by heterogeneous nucleation and further wire heating pushed boiling towards a homogeneous nucleation mechanism. The limiting liquid superheat temperature was 309-314°C with a predicted nucleation rate of 10^{21} - 10^{28} nuclei/m³-s. Though a rough calculation was reported, it was consistent with predictions made by the homogeneous nucleation theory. This study also shows that explosive boiling is initiated through a combination of heterogeneous and homogeneous nucleation.

2.2 Secondary Droplet Atomization Literature

2.2.1 Secondary Droplet Atomization Mechanisms and Thermal Effects

The study by Wahcters, Smulders, Vermeulen, & Kleiweg (1966) set the early framework for modern studies of secondary droplet atomization. Wahcters used a spray of water droplets (diameters of 50-75 µm) impacting on various heated surface materials (gold, platinum, stainless steel and copper) at 200-400°C. The author inferred the evaporation rate by measuring the decrease in droplet volume after impact with surface. A method involving mist sprays where the water amount was recollected after impact was used. Multi-droplet complexities and liquid-liquid interactions were therefore introduced in the results. Nonetheless, the author reported an exponential decrease in the droplet evaporated weight as the surface temperature increased. At 400°C a stable film layer was developed in which the weight loss of the droplet from evaporation was less than 0.5%. Unfortunately, the authors did not attempt to characterize secondary droplets with respect to boiling regimes despite having the data available to them.

A deeper investigation into the secondary droplet atomization was accomplished in the study of Watanabe, Suzuki, Harada, Matsushita, Aoki, & Miura (2010). The

author investigated the break up characteristics of secondary droplet atomization during an explosive boiling event. The amount of vapour mass produced and the break up time during an explosive boiling event were reported. A single emulsified fuel drop containing 10% water was suspended from a thin platinum wire and then heated from room temperature to the temperature of vapour explosion at 172°C. It was reported that break up occurred within the first 2 ms of attaining the vapour explosion temperature. However, it should be noted that this time frame was based on a camera capture rate of 1000 frames/s, representing only 1 ms degree of accuracy. Vapour explosions typically occur much quicker in the order of microseconds rather than milliseconds. Despite this limitation, there was a strong dependence of the surface temperature on droplet break up time. Break up times decreased by a factor of three for an increase in wall superheat of 20°C. About 50-70 wt% of water in the emulsified fuel droplet instantaneously vapourized when explosive boiling was first initiated.

A very detailed study by Richter et al. (2005) reported the morphology of secondary droplet formation due to thermal effects ranging from the initiation of nucleate boiling to the film boiling. The effect of wall surface temperature on the diameter and trajectory of atomized secondary droplets was also investigated. The mechanisms of secondary droplet atomization are well documented and provide the basis of understanding of the interactions in this present study. Isooctane droplets of sizes between 60-100 μm were impinged, with a velocity of 3.8-30 m/s, on an aluminum alloy surface ranging in temperature from 99-270°C. It should be noted this study was done with multiple droplets impacting a surface one after. Therefore, liquid-liquid interactions were present and skew some of the visual interpretation of the secondary droplets characteristics.

At surface temperatures at the saturation point of the liquid, no secondary droplets were produced. Instead, deposition of primary droplets residing on the surface occurred. As the surface temperature was increased, secondary droplets were produced and became smaller in size with trajectories that were perpendicular to the surface, in combination with droplet ejection occurring radially outwards from the surface. Greater break up and larger vertical distribution of secondary droplets was due to the collapse of a greater number of vapour bubbles at the liquid-solid interface as surface temperature was increased. A temperature limit was reached where secondary droplet sizes and distribution were at a minimum and a maximum respectively. Beyond this temperature, film boiling was observed and resulted in an increase in secondary droplet size. With a stable vapour layer underneath, droplet break up is not as prominent, hence larger sized secondary droplets. The velocity of the secondary droplets was the highest when the break up was the most significant. The velocity of secondary droplets decreased sharply once the surface temperature attained the Leidenfrost point.

The influence of the initial droplet Weber number was that secondary droplet sizes decreased with increasing Weber number. The greater kinetic energy of the

initial droplet creates waves upon impact from which secondary droplets are driven out of the liquid. Similarly, the velocity of the secondary droplets is increased as a result of a higher initial droplet Weber number. It should be noted that due to experimental limitations of this experiment (multiple drops impact the surface in succession so that the Weber number was tied to the impacting frequency of droplets), the variance of the Weber number on secondary droplet characteristics is greatly influenced by liquid-liquid interaction. Disparities exist in the reported measurements of secondary droplet size and velocity due to the complexities regarding multi-drop experiments.

Cossali et al. (2002) investigated secondary droplet atomization characteristics: size and distribution on a heated aluminum alloy surface. A single water droplet, with diameter of 2.1 mm and an impact velocity of 3.13 m/s, was impacted on a surface at 150°C and 260°C, representing the nucleate and film boiling regime respectively. They observed that the characteristic times at which secondary droplet atomization began differed with the boiling regime. In the nucleate regime, secondary droplet formation occurred a few milliseconds after impact and was due to thin liquid jets protruding from the liquid layer and from rupture of vapour bubbles. This result is expected for low wall superheats in the nucleate boiling regime. However, wall superheats can attain high values within the nucleate boiling regime towards the critical heat flux, and secondary droplet atomization can occur in microseconds instead. In the film boiling regime, the author reported that atomization occurred immediately after impact due to the break up of the vapour film layer that was instantaneously formed to levitate the droplet. The results of break up time should be carefully assessed since only two surface temperatures were studied by Cossali et al. (2002). More surface temperatures are required within each boiling regime to draw accurate analyses.

Coassali, Marengo, & Santini (2003) studied secondary atomization produced by multi-drop interactions on a heated wall. The study characterized and compared the impacts of three water droplets simultaneously impacting a wall representing a nucleate boiling regime at 145°C and a film boiling regime at 260°C. Further, an attempt to estimate secondary droplet number, diameter and total mass removed after impact was quantified. The droplets were 2 – 4 mm in diameter impacting an aluminum alloy surface with a velocity of 6 m/s. For both single and multi-drops, the authors observed that the maximum secondary droplet count was higher in the nucleate boiling regime than the film boiling regime. The main finding was that multi-drops produced a less number of secondary droplets than single drop tests. This was due to the liquid-liquid interaction in multi-drops tests in which the liquid bulk droplet coalesced together after impact thereby creating a liquid jet. Because of liquid-liquid interactions, the average size of the secondary droplets in nucleate regime tended to be as big as the droplets in the film boiling region at early time stages. Furthermore, it was not noted whether splashing occurred given that the impact velocity of the initial droplet was high and could produce

secondary droplet sizes inconsistent with those evolved from thermally induced atomization.

A second study by Cossali, Marengo, & Santini (2005) analyzed the effect of varying the primary droplet size from 1.80-4.60 mm and liquid viscosity on secondary droplet characteristics. The experiment used either a single droplet of pure water (viscosity = 1.076×10^{-3} kg/m·s) or a water-glycerine mixture (viscosity = 1.243×10^{-3} kg/m·s) on an aluminum alloy disk. The author reported that secondary droplet sizes depend linearly on the primary droplet size. Larger primary droplets produced larger secondary droplets in the nucleate boiling regime but no mention of the effect in the film boiling region was reported. The study also showed that increasing the liquid viscosity resulted in atomization occurring at a later time in the nucleate boiling regime. A possible reduction in the Reynolds number functions to depress the convective heat transfer from the solid surface to the liquid.

The study by Moita & Moreira (2007) investigated variances in surface tension and latent heat of vapourization of the initial liquid droplet on secondary droplet characteristics. The two test fluids were HEE7100 and pure water with initial velocity of 2.5 m/s. HEE7100 had a surface tension and latent heat of vapourization of 13.6×10^{-3} N/m and 122.6 kJ/kg respectively, while water was 73.75×10^{-3} N/m and 2272 kJ/kg respectively. The droplets impacted a surface of stainless steel at respective nucleate and film boiling temperatures of each liquid. Initiation of atomization occurred quicker in the nucleate boiling regime when the surface tension and latent heat of vapourization were lower. Mention of the film boiling regime was not reported but would follow a similar trend. The vapour cushion would be created quicker for the liquid with lower heat of vapourization.

2.2.2 Secondary Droplet Atomization and Surface Variations

The study by Wahcters et al. (1966), mentioned earlier in this section, also provided the groundwork to study the effect of variances in surface thermal conductivity. Surface thermal effusivity would be a more accurate term to use here since it accounts for not only thermal conductivity but also the material density and heat capacity. Nonetheless, the author provided reasoning for the time scale differences in boiling modes. Wahcters et al. (1966) showed that for low conductivity surfaces of platinum and stainless steel, the progression into transition boiling regime was much more gradual than high conductivity surfaces of gold and copper. This was due to low thermal conductivity materials having lower response time to variances in temperature gradients and therefore underwent greater temperature decreases during droplet impact. As a result, the boundaries defining heat transfer regimes will differ depending on the liquid-solid surface properties and ultimately influence the secondary droplet characteristics.

This realization provided further motivation for studies investigating thermal effusivities on secondary droplets.

Cossali et al. (2006) altered the thermal effusivity of a heated surface by using two different materials (at nucleate or film boiling temperatures) with varying thermal conductivities and investigated the effect on secondary droplets. In this study, increasing thermal conductivity is equivalent to saying an increase in thermal effusivity or an increase in thermal diffusivity. These terms are interchangeable here. A single droplet of water normally impacted an aluminum alloy surface with a higher thermal effusivity of $20.7 \times 10^3 \text{ kg/Ks}^{5/2}$ than the stainless steel surface at $7.19 \times 10^3 \text{ kg/Ks}^{5/2}$. The study showed that thermal effusivity primarily influences the time domain of droplet heating. Quicker formation of vapour bubbles in the nucleate boiling regime lead to quicker atomization initiation and in the film boiling region vapour cushion formation occurred quicker. The time scale of impact and heating therefore heavily influenced secondary droplet formation. Secondary droplets were larger in diameter in the high surface effusivity material than the lower one. It should be noted that only two surface temperatures were used; 136°C and 232°C , and represented the nucleate and film boiling regimes respectively. Data involving surface temperatures in the transition boiling regime or where atomization can be the strongest close to explosive boiling conditions were missing in this study. A greater range of surface temperatures is required to accurately quantify secondary droplet characteristics including count, diameter, velocity and ejection trajectories.

An extension of the previous study by Cossali et al. (2006) also considered the impact angle of droplets on the heated surface. The previous discussion considered impacts at 90° only. Varying the impact angles from $6-60^\circ$ showed that droplets favoured bouncing away from the surface at lower impact angles for both temperature regimes. Secondary droplet diameters decreased as impact angle was lowered and was the most prominent in the film boiling regime. It was proposed that lower impaction angles reduced the droplet compression on the surface and inhibited the break up of the droplet that is responsible for creating large diameter secondary droplets.

Impact angle studies on secondary droplets atomization have also been studied by Moreira, Moita, & Cossali (2007) who used single isooctane droplets impacting a stainless steel surface ($100-300^\circ\text{C}$) varied in tilt angle from $15-90^\circ$. The author reported secondary droplet counts that were small during the spreading phase of the bulk droplet on the surface and then increased during the intense period of boiling. Also, lowering the impaction angle increased the mean velocity of the secondary droplets. The influence of impaction angle was greater in the nucleate boiling regime compared to the film boiling regime. In order to minimize

variances due to boiling regime on droplet atomization, this dissertation only considered initial droplet impacts that were 90° to the surface.

Surface roughness effects have been studied by Cossali et al. (2005). Their second study analyzed the effect of varying heated surface roughness on secondary droplet characteristics. The experiment used either a single droplet of pure water or a water-glycerine mixture on an aluminum alloy disk, varied in surface roughness of $R_z = 1.6 \mu\text{m}$ or $14.5 \mu\text{m}$. Increasing the surface roughness caused quicker initiation of atomization in the nucleate boiling regime. As for the mean secondary droplet diameters, the sample size for the nucleate boiling was too small and accurate trends due to surface roughness could not be established. However, for the film boiling regime, secondary droplet size were reported to slightly decrease with greater roughness.

Drastic alterations to the heated surface topography were made by Moita, Sauer, & Moreira (2012) by creating controlled microstructure pillars on a silicon wafer and observing the effect on secondary droplet atomization. Essentially, this study controlled and varied the roughness of the surface on a micrometer scale. The pillar width, height and separation distances varied from $0\text{-}307 \mu\text{m}$, $0\text{-}23.9 \mu\text{m}$ and $0\text{-}405 \mu\text{m}$ respectively. A single droplet of either water or ethanol was impacted with an initial velocity of 1.4 m/s . The author reported that varying the pillar height could optimize the roughness value and therefore narrow or widen the distribution secondary droplet sizes. The application of this study could be used to enhance cooling performance on micro-textured surfaces that contact liquid coolant and has applicability within the nuclear industry as well.

2.2.3 Secondary Droplet Atomization Correlations

The correlations for secondary droplet characteristics evolved from droplet impacts with a solid, non-heated surface are well developed and noted in literature (Arcoumanis, Whitelaw, & Whitelaw, 1997; Trujillo, Matthews, Lee, & Peters, 2003; Yarin & Weiss, 1995). The inertial energy in droplet splashing contributed to the production of secondary droplets in those studies rather than thermally induced atomization. For example, the correlations developed by Samenfink, Elsaber, Dullenkopf, & Wittg (1999) provided models for the deposited mass fraction and composition ratio of the secondary droplets during impacts with solid surfaces. Droplet splashing was induced with high impact velocity and with shear-driven break up on a tilted solid surface. The author reported power law relationships for secondary droplet composition, diameter, velocity, and angle with respect to dimensionless quantities of initial droplet momentum, impaction angle, liquid film height and the Laplace number. The author also reported good agreement with the predictions and experiments. These correlations serve as a

basis to extend thermal considerations when a droplet impacts a solid heated surface.

To the knowledge of this author, correlations involving secondary droplet atomization from thermally induced heating effects are limited. Specifically, those characterizing secondary droplet properties such as the diameter, velocity, and trajectory.

Moita & Moreira (2009) used their previous experimental studies to develop empirical correlations to describe secondary droplet diameters in the nucleate and film boiling regime. The bases of the correlations were through their own experimental work that investigated the influence of a range of factors including; initial droplet diameter, impact velocity, viscosity, latent heat of vapourization, impact angle and surface topography. The correlations featured dimensionless quantities describing the liquid-solid surface impacts with heat effects. In the nucleate boiling regime, the author proposed a power law relationship for the mean secondary droplet diameter as a function of the Reynolds number, Weber number and Jakob number. A correlation, obtained from Akhtar et al. (2001), for the film boiling regime was proposed where the secondary droplet diameter was defined as polynomial expression of the Weber number only. Additionally, film boiling secondary droplet count was reported as a linear relationship of the Weber number.

Previous secondary droplet correlations were limited to only the film boiling regime since the large size of secondary droplets could be measured accurately with imaging software. Correlations in the nucleate boiling regime were only first attempted in this study and no known correlations exist for secondary droplet characteristics in the transition boiling regime or for temperatures near the superheat limit. Beyond secondary droplet diameters, there have been limited attempts at modeling secondary droplet counts and velocities. Development of not only models but experimental studies focusing in the transition boiling regime where droplet atomization is the most violent due to explosive boiling are also required.

2.3 Comments on Literature

From the literature review presented above, it can be seen that notable attempts to measure explosive boiling energy has come primarily in the form of measuring acoustic pressure waves. The study Nematollahi (2008) estimated the force of growing vapour bubbles during rapid boiling. The calculations were based in momentum transfer of bubble radius, mass and surface tension and provided a rough estimation at best. It is this type of quantification of force that will be attempted in this study.

For the literature on secondary droplet atomization, the majority of the studies focused solely on a narrow range of heated surface temperatures. The selection of temperatures solely in the nucleate and film boiling regimes are numerous but do not give consideration to surface temperatures near the superheat limit nor the transition boiling regime. Furthermore, the emphasis of these studies focused their analyses on the time and spatial scales rather than on the surface temperature. More attention to the secondary droplet characteristics as a means to describe explosive boiling energy with respect to wall superheat is thusly required and attempted in this study.

Chapter 3: Experimental Setup and Methodology

In this chapter, detailed description of the main experimental components and their function is provided with a testing methodology and equipment uncertainties.

3.1 Experimental Setup

An experimental setup was designed and built in order to investigate explosive boiling characteristics over a wide range of surface temperature ranges. A pre-existing setup termed the “Water Quench Facility” was built at McMaster University for quench cooling experiments. This setup was inherited for this study with modifications made specific to single droplet interactions rather than quench cooling interactions.

The main components of facility are the furnace, water valve and specimen holder. A simple schematic featuring the main components of the facility is shown in **Figure 3** while **Figure 4** shows the actual setup. This set up allows for quick withdrawal of specimens from the furnace so that heat losses of test surface are minimized during the removal period.

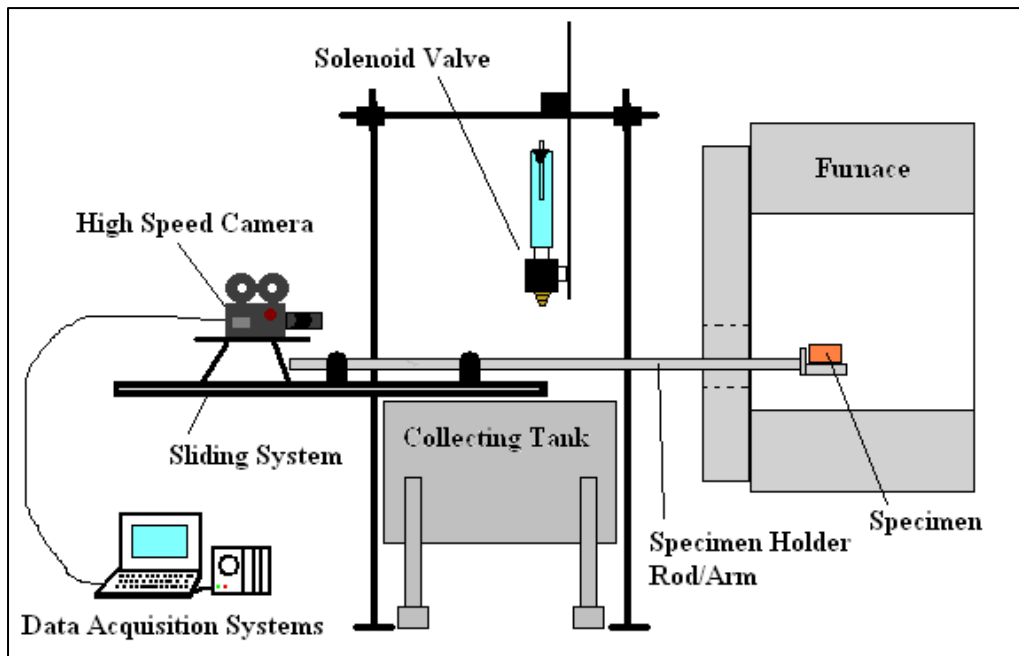


Figure 3 – Schematic of major components of the Water Quench Facility

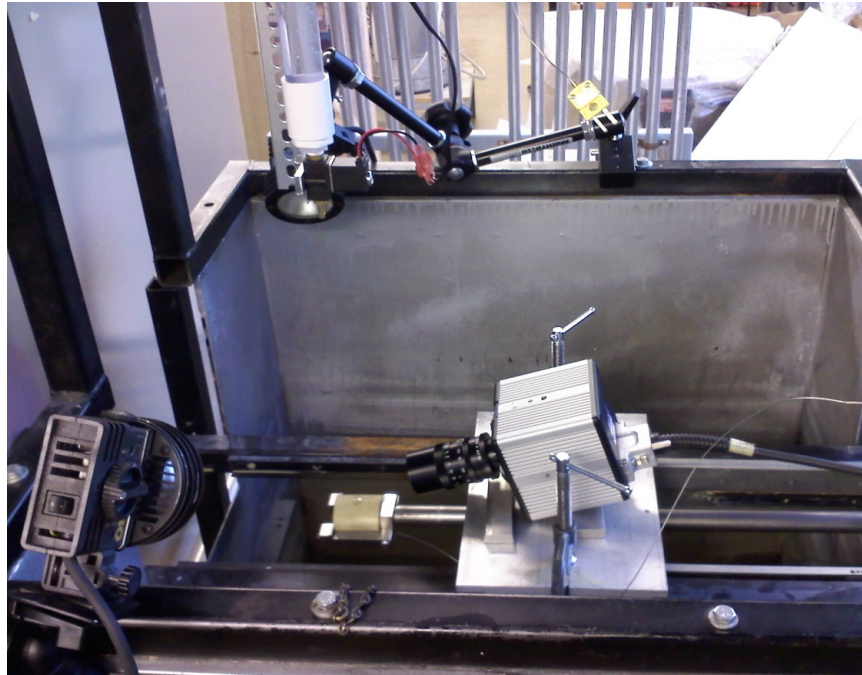


Figure 4 – Main components of the water quench facility (shown are high-speed camera, two halogen lights, specimen, holder and water valve)

3.1.1 Specimens

Materials of copper, brass and stainless steel were chosen for the investigation of water droplet interactions. Their surface temperatures were varied from ambient conditions of 30°C to 700°C. The materials were selected to represent a range of thermal conductivities in order to investigate the heat transfer effects on droplet impacts and explosive boiling. **Table 2** and **Table 3** summarize key properties of the specimen materials and liquid water respectively used in this study.

Table 2 – Specimen material properties at 25°C (Park et al., 2005)

Specimen Material	Density, ρ [kg/m ³]	Heat Capacity, C_p [J/kg·K]	Thermal Conductivity, k [W/m·K]	Thermal Diffusivity, α [m ² /s]
Copper C1100	8933	385	401	1.17 x 10 ⁻⁴
Brass C360	8530	380	110	3.39 x 10 ⁻⁵
Stainless Steel AISI 316	8238	468	13.4	3.48 x 10 ⁻⁶

Table 3 – Liquid water properties at 25°C (Park et al., 2005)

Density [kg/m ³]	997
Heat of Vapourization [kJ/kg]	2442
Specific Heat [J/kg·K]	4180
Viscosity [N·s/m ²]	897 x 10 ⁻⁶
Thermal Conductivity [W/m·K]	610 x 10 ⁻³
Surface Tension [N/m]	72.1 x 10 ⁻³
Critical Temperature [°C]	374

The highest thermal conductivity material was copper, followed by brass. The lowest was stainless steel. Since stainless steel has a low thermal conductivity, comparable to that of Zr-2.5%-Nb pressure tubes used in CANDU reactors, it is a suitable candidate to investigate droplet impacts and draw parallels towards cases involving interactions with water and fuel clad material.

Half rods (hemispheres) and flat plates were the surface shapes of interest in this study. Hemispheres were of copper, brass and stainless steel, while only a plate of brass was used in this study. For the hemispheres, 2" (5.08 cm) diameter rods for each material were cut in half axially and then milled to a length of 2" (5.08 cm) with an accuracy of ± 0.0005" (± 0.013 mm). The brass plate had dimensions of 2" x 2" x 1" (5.08 cm x 5.08 cm x 2.54 cm). **Figure 5** depicts a schematic and photos of typical hemispheres and a flat plate with embedded thermocouples used in this study.

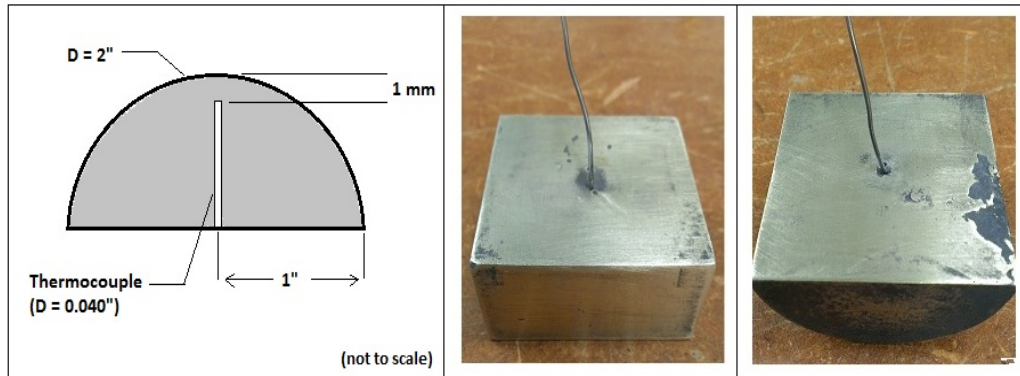


Figure 5 – Schematic of typical specimen dimensions (left), brass flat plate (middle) and brass hemisphere (right)

A K-type thermocouple (Omega Super Omegaclad XL) with a maximum deviation of ± 0.8°C at 650°C was selected to take temperature measurements due

to its stability at high temperatures. The sheath diameter of the thermocouple was 0.040" (0.102 cm) and was small enough to minimize heat losses through it and to reduce measurement response times. The thermocouple tip was located at a depth of 1 mm from the outer surface where the water droplet was to impact at the center of the specimen. A minimal clearance of 0.001" (0.0254 mm) existed between the thermocouple and the drilled hole in the metal specimen. The thermocouple was then inserted in the hole and small punches were created on either side of the thermocouple to close the space around it and to secure it in place.

Other thermocouple mounting techniques such as high temperature cements and soldering filler were considered in this study. High temperature cements are known to fracture after repeated heating and cooling cycles and were not appropriate in this current study given the number of tests performed on each specimen over a high temperature range.

A preliminary thermocouple mounting technique known as brazing was initially attempted and used silver solder to fill the gap between the hole and the thermocouple. The silver solder and flux material were Braze051 and Hi-Temp095 respectively, purchased from Lucas-Milhaupt Inc. The silver solder was chosen so that its melting point was greater than the maximum test surface temperature of 700°C but below the specimen's melting point. The Braze051 silver solder had a melting point around 880°C, just below the melting point of brass, which had the lowest value of the three specimens. From initial brazing tests, it was found that the silver solder had difficulty in reaching the proper brazing temperature that would allow it to flow into the clearance hole. Using a torch allowed for greater localized and intense heat application to the specimen and silver solder. Heat was applied to the underside of the specimen but it was found that the heat would dissipate too quickly around the joint. This was because the thickness of the specimen made it difficult to maintain a uniform brazing temperature and thus the silver solder would not flow. Direct torch heat application to the joint was found to damage the thermocouple wire. Furnace heating was also attempted because a uniform temperature environment could be achieved. However, the long heating cycle of the furnace resulted in oxide formation that impaired the ability of the silver solder material to flow into the clearance hole.

Ultimately, holding the thermocouple in place with punches was sufficient given that both the specimen and thermocouple metal would expand into the negative space during heating. Material expansion serves to minimize the clearance gap but more importantly improves the physical contact at the interface of the thermocouple tip and the specimen. In this study, temperature measurements were accurately obtained across all temperature ranges for all materials.

3.1.2 Holder System

The metal specimens were secured on a movable holder system and heated in a box furnace of dimensions 3 ft x 3 ft x 3 ft with a maximum attainable temperature of 1000°C. A 4" (10.2 cm) diameter port on the furnace side door allowed insertion and removal of the metal specimens. The holder system featured a stainless steel arm piece in which the metal specimen rested and was clamped into place as seen in **Figure 6**.



Figure 6 – Specimen holder shown with a copper hemisphere clamped in place

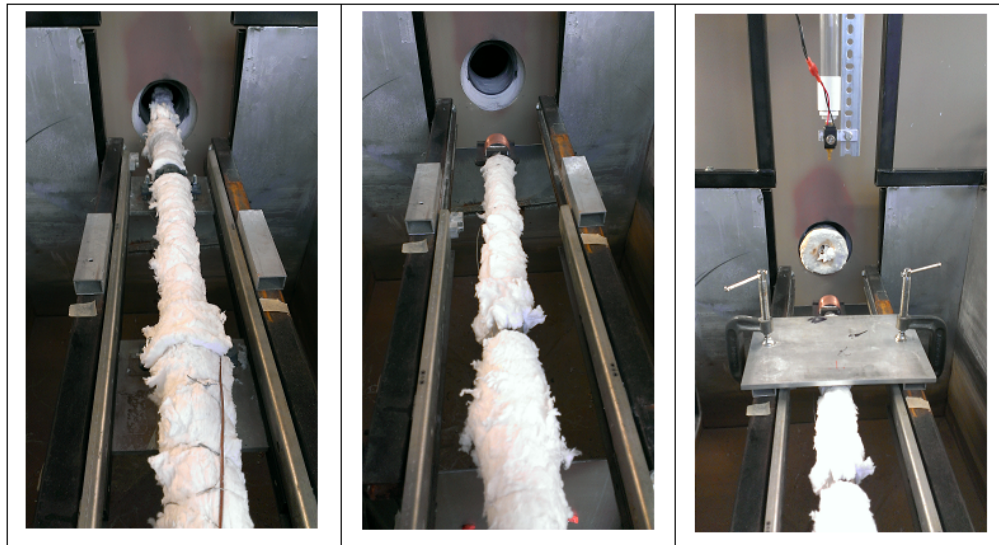


Figure 7 – Support rod on a moveable track. Rod inserted in furnace (left), fully withdrawn position (middle) and shown relative to water valve position (right)

The arm piece components were held together by ¼”-20 UNC stainless steel screws. The arm piece was attached to a 5.5 ft long, 1” (2.54 cm) diameter steel rod that was secured on a movable track by two base-mounted bearings. The steel rod was covered in an aluminosilicate high temperature insulator to prevent thermal damage to the thermocouple connectors and camera equipment. The holder system was moved manually, in which the fully withdrawn position allowed the water valve to reside directly above the surface of the heated metal specimen. The support rod on the moveable track is shown in **Figure 7**.

3.1.3 Water Valve and Controller

A solenoid valve was chosen to produce the water droplets due to the sensitivity of the valve orifice being able to open and close quickly from a controllable electrical pulse. The water valve is shown in **Figure 8**.

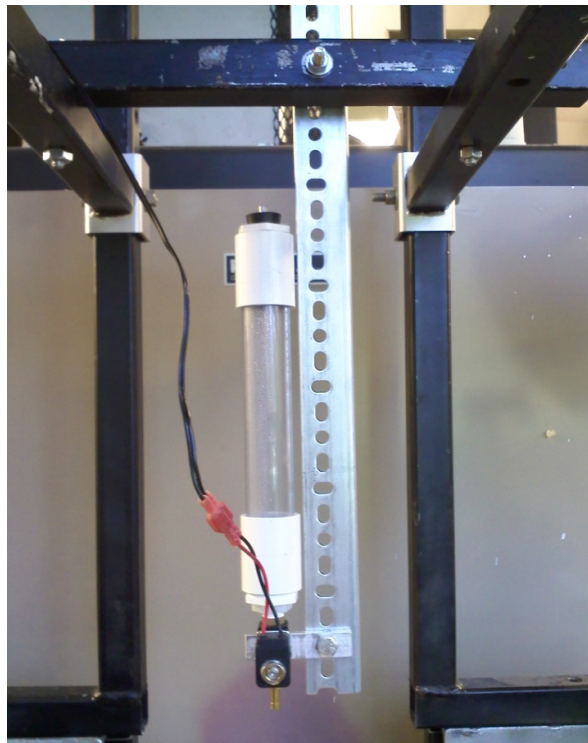


Figure 8 – Water valve and water reservoir supported above the metal specimen

A two-way, direct acting, normally closed solenoid valve was chosen for this study. This valve featured an orifice size of 2 mm and had a quick response time of less than 20 ms, which allowed droplets to be released quickly when a current

was applied. The valve was supplied with water at 25°C from a reservoir that resided above it. The reservoir was a 1” diameter, 12” long PVC pipe that features a siphon that was open to the atmosphere. The purpose of the siphon was to ensure a constant pressure of water was fed to the valve inlet in order to produce a consistent droplet size and release. A brass nozzle was connected to the valve outlet with an inner diameter of 0.1585” (4.03 mm). The valve was located at a height of 12.5” (31.75 cm) above the surface of the metal specimen resulting in a droplet impact velocity of 2.5 m/s. Its corresponding Weber number, based on water droplet properties at 25°C was $We = 432$.

An electronic timing device manufactured by StopShot controlled the solenoid valve. This device was capable of producing a maximum pulse count of 1000 with selectable pulse durations from 100 μ s to 24 hrs. In order to produce one water droplet, StopShot was programmed to generate one pulse initiated by a manual button press from the user. The pulse duration was an influencing factor in water drop release and size. A pulse that was too quick would result in the valve orifice being open for too short of a period and had the consequence of not releasing a droplet. A pulse that was too long resulted in a droplet being released trailed by several smaller droplets. It was found that a range of pulse durations from 6 ms to 26 ms released one clean droplet consistently with a droplet volume range of 0.0155 cm³ to 1.382 cm³. Small droplets had difficulty showing up on the camera and were especially difficult when fragmentation into smaller droplets occurred after impact. The spherical shape of large droplets would deform on descent due to aerodynamic forces and would cause varying contact areas upon impact due to an ellipsoidal shape. For these tests, a pulse duration of 10 ms was chosen, representing an average initial droplet volume of 0.065 cm³.

3.1.4 High-Speed Camera and Data Acquisition System

The FASTCAM-X PCI 1024 high-speed camera provided by High Speed Imaging Inc. captured the images and videos of the water drop interactions with the solid surfaces.

The camera features a CMOS (complementary metal oxide semiconductor) light sensor and has advantages of low cost, low power consumption with high data processing speeds suited for continuous, high frame rate video capture. This camera features a maximum recording resolution of 1024x1024 pixels at 60 frames/s and up to a maximum frame rate of 109,500 frames/s at a limited resolution of 128x16 pixels. The amount of available recording time was dependent on the resolution and frame rate chosen. A high resolution and frame rate allocated less recording time compared to low resolution and low frame rate.

Careful selection of resolution and frame rate was required to visualize the droplet fall and impact clearly while allocating sufficient recording time to capture the entire process. A resolution of 512x512 pixels at a frame rate of 1000 frames/s, yielding 6.4 s of recording time, were used in these tests. Tied to the resolution was the aspect ratio of the recording window. The chosen resolution gave a rectangular viewing window of approximately 9 cm x 9 cm and was sufficient to capture the post-impact outcomes where secondary droplets can have potentially large escape trajectories. The necessity to track every secondary droplet's position with respect to the impact point also factored into the resolution choice.

Two halogen lights were located above the collecting tank walls on either side of the specimens. Back lighting was not appropriate in this study due to the large amount of background noise created from the light reflection off the metal surfaces of the Water Quench Facility. Directing the lights downwards at an angle above the specimen surface provided the best visual images. For the majority of tests, a 1/16000s camera shutter speed was selected in order to darken the background and to reduce the reflection of the halogen lights off of the collecting tank walls while keeping the specimen and water droplet adequately lit. In a few tests at high temperatures ($> 400^{\circ}\text{C}$), surface oxidation of the specimen darkened the field of view rendering droplets difficult to see. The camera shutter speed was increased to account for any darkening effects that occurred. The camera sat on a platform above the specimen support rod with the lens at a distance 2" (5.08 cm) from the specimen surface.

Temperature measurements were recorded by a NI SCXI-1000 data acquisition system at a sampling rate of 1000 samples/s. Temperature measurements and camera recording were initiated simultaneously through a manual software trigger and were synchronized during the process. The water droplet release occurred by a manual button press of the valve controller immediately after the camera/data logger combination was initiated.

3.2 Test Procedure

The experimental data in this study were obtained by the following procedure:

1. Before each test, the outer surface of each metal specimen was polished with Emery paper with grit number 600 to the desired surface finish.
2. The specimen was placed in the holder and adjusted to the correct position. Once in the correct position, the specimen was clamped in place by tightening the clamp end screws.

3. The thermocouple wire extending from the specimen was secured along the length of the holder arm and connected to the Data Acquisition Device (DAQ).
4. Water was poured in to the solenoid valve reservoir and closed by securing a rubber stopper on the top.
5. The solenoid valve was initially purged of air. A small volume of water was then purged into a waste beaker to ensure the reservoir water pressure was sufficient to produce a clean droplet release and consistent size.
6. The specimen was inserted into the furnace and then heated to the desired specimen surface temperature. The DAQ was programmed to track the heating cycle of the specimen.
7. Once the specimen surface temperature reached the desired level and was at steady state, the camera lights were turned on and the camera and DAQ were put into a ready mode prior to specimen removal from the furnace.
8. The specimen was removed from the furnace to the desired position underneath the water valve.
9. A manual software trigger button was pressed which initiates camera recording and temperature readings to start simultaneously. Immediately after the software trigger was clicked, a manual button on StopShot was pressed which released one water droplet.
10. The recording length for both the camera and DAQ were sufficient to cover the water droplet fall and the resulting impact. The camera images and video with temperature data were obtained and saved for analysis.

3.3 Key Parameters and Equipment Uncertainties

Listed below is a summary of the parameters that were varied and fixed in this study.

1. Varied parameters:

- Surface material/thermal diffusivity: Copper, Brass, Stainless Steel
- Surface shape: Flat plate or hemisphere
- Surface Temperature: 30°C to 700°C

2. Fixed parameters:

- Droplet temperature: 25°C
- Droplet size: diameter = 0.5 cm
- Droplet impact velocity: 2.5 m/s
- Droplet Weber number: 432

The raw data obtained from the droplet-surface interaction in this study were: i) surface temperature profiles ii) high-speed camera images. **Table 4** outlines the absolute uncertainty associated with data acquisition devices, image processing software and specimen dimensions. Further discussion on the propagation of measurement uncertainty on secondary droplet properties and explosive boiling force estimation is provided in Section 5.2.4 and in Appendix C.

Table 4 – Measurement uncertainty for experimental equipment

Measured Variable	Uncertainty
Specimen dimensions	± 0.013 mm
Surface temperature	Maximum deviation of thermocouple: $\pm 0.8^\circ\text{C}$ at 650°C
Time (from DAQ)	$\pm 5 \times 10^{-4}$ s
Time (from High-Speed Camera)	$\pm 5 \times 10^{-4}$ s
Initial droplet size from water valve	± 0.36 mm
Length measurements in image analysis software	± 0.175 mm

Chapter 4: Visual Image and Temperature Raw Data Observations

This section describes the visual images and the specimen surface temperature raw data. A description of how the data is interpreted is also given. The discussion of results and trends is reserved for the next chapter.

4.1 Visual Description of Images

A high-speed camera was used to capture images of the water droplet fall, impact, and post-impact phenomena. The images were recorded using software unique to the high-speed camera called PFV Ver.4, developed by Photron High Speed Cameras Inc. The high-speed images were analyzed using image analysis software to determine trends in droplet count, size, distribution, and position.

4.1.1 High-Speed Camera Images

The camera recorded the events of the droplet fall from the valve, droplet impact on the surface, and the impact outcome until the specimen surface was cleared. For the purpose of presentation of image sequences in this dissertation, the images were cropped to remove the excess area above the specimen surface but left enough area to visualize the droplet impact and result. A typical high-speed image sequence is shown in **Figure 9**, where each frame represented 1 ms in time. All image sequences were centered at the instant the droplet contacted the surface at $t = 0$ ms. The time markings in each frame represented the time after initial impact with the surface.

As the droplet descended onto the specimen surface, its shape was slightly distorted due to the drag resistance of the air it travelled through. The falling droplet's edges were clearly defined by the light reflecting off of it, as seen in **Figure 9** at $t = -4$ ms. Some regions within the droplet appeared brighter than others. This was due to the droplet shape deformation causing light to be reflected irregularly into the camera.

The moment the droplet impacted the surface is shown in **Figure 9** at $t = 0$ ms. The droplet compressed on the surface then spread radially outwards. The intensity of droplet illumination during the spreading phase was dependent on the type of boiling present at the interface as depicted in **Figure 10**.

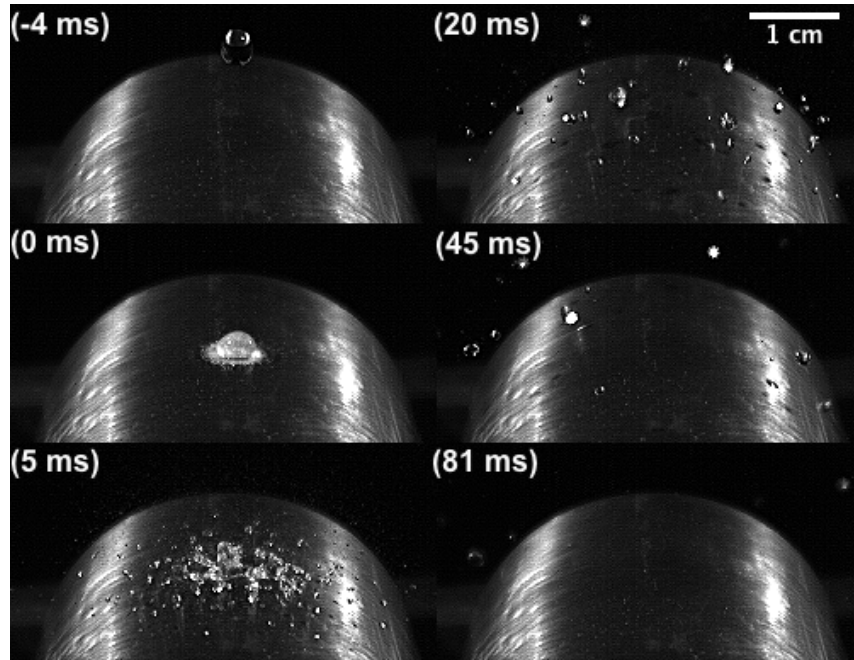


Figure 9 – Droplet impact sequence of a curved brass surface at a surface temperature of $T_s = 250^\circ\text{C}$

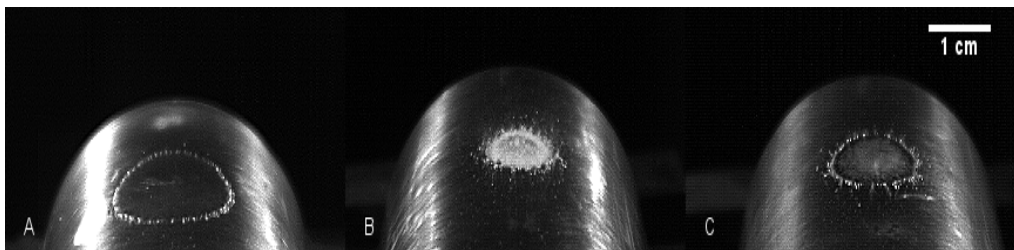


Figure 10 – Boiling effects on droplet illumination for a curved brass surface at surface temperatures; Frame A – 30°C , Frame B – 250°C , Frame C – 400°C

When boiling does not occur, the droplet was transparent on the surface (**Figure 10** Frame A). When a high degree of nucleate boiling was present in the droplet, it was observed to be brighter than the surface (**Figure 10** Frame B). This was due to the high nucleation rate creating tiny bubbles that collectively reflected greater amounts of light within the bulk droplet. **Figure 10** Frame C shows a case with increased surface temperature but a reduced influence of boiling on the droplet that is typical of the transition and film boiling regime. The center of the droplet appears slightly lighter than the surface signifying a region of wetting where the influence of boiling created a vapour layer cushion. The non-wetting region was

observed as the dark regions within the spreading droplet, signifying a vapour layer that separated the liquid from the specimen surface.

Referring back to **Figure 9**, after the droplet spread on the surface, secondary droplets were created and seen to develop through frames $t = 5$ ms, 20 ms, 45 ms and were dependent on initial surface temperature. The temperature dependence of post-impact phenomena will be discussed in the next chapter. Large secondary droplets were easily distinguished after droplet impact with the surface. However, inspecting the images closer revealed that a fine mist of secondary drops was also produced. They are not seen in the images above because their size was so small (about one pixel² or equivalently 0.033 mm²) that the intensity of light reflection off of them was very faint. In order to visualize their presence in these images, image processing was required to distinguish them.

Additionally, from **Figure 9**, two light bands on either side of the specimen were due to reflection of the light sources. Surface reflection was evident for all specimens at lower surface temperatures but was non-existent at higher surface temperatures beginning around 400°C because of surface oxidation. The light source intensity and shutter rate were adjusted accordingly to give the best illumination of the droplets and specimen surface. Treating the specimen surface as a background and removing it from all subsequent images during processing mitigated the interference of surface reflection on droplet analyses.

4.1.2 Image Processing

An open source software developed by the National Institutes of Health USA called ImageJ 1.46r was used to process the images recorded by the high-speed camera. Image J 1.46r is a Java-based program that can display, edit, process and analyze various images formats. Image processing was necessary to visualize the entire scope of secondary droplet sizes and to remove background noise. Furthermore, the isolation of the initial droplet and secondary droplets extracted data about droplet counts, size and distribution over the lifetime of an impact event. The raw images amassed from each droplet impact sequence were saved as a lossless file format. Image quality losses due to image compression were avoided by using a “.tiff” file extension. In this way, the highest quality images were used by ImageJ to accurately analyze and measure elements within a given image.

In order to accomplish analyses on the droplets, the raw images from the high-speed camera were converted into a software readable format, known as a binary image (white and black image). A binary image was required in order to highlight only the droplets as foreground objects (white elements) for image analyses while

ignoring everything else in the image that was not a droplet as a background object (distinguished as black).

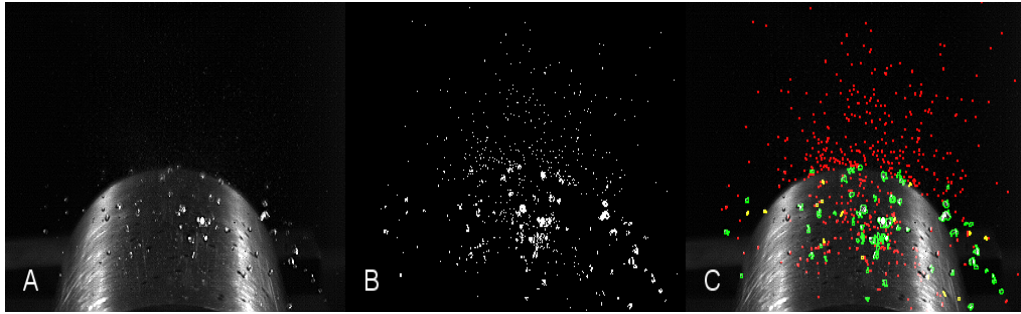


Figure 11 – Image processing of a raw image to visualize droplet impacts. Frame A – raw unprocessed image, Frame B – binary image of droplets, Frame C – re-combined and coloured processed image

The droplets from the raw image, **Figure 11** Frame A, were isolated by first subtracting the background image of the metal specimen from each frame, leaving behind only the images of the illuminated droplets. Since the water droplets reflect the greatest amount of light, the intensity of droplet illumination can be detected by the software and used to differentiate droplets from the background. ImageJ uses the illumination intensity of image elements in a process known as “thresholding” which results in creation of a binary image, seen in **Figure 11** Frame B.

Thresholding works by defining a pixel intensity cutoff. Elements in the image whose illumination intensity was below the cutoff level became black (i.e., part of the background) and those above became white (i.e., defined as droplets). Careful selection of the pixel intensity cutoff point was two-fold; to visualize both large and small secondary droplets while minimizing background noise. The cutoff was selected to be a value of 13 out a pixel intensity scale of 255 and was constant for all specimen surfaces, at all temperatures.

In the binary image, the white elements represented the secondary droplets. It is evident from **Figure 11** Frame B that there are a greater number of secondary droplets than observed in the raw image once thresholding was applied. Using the "Analyze Particle" function in ImageJ, the software can detect the white elements of the binary image and give information about each secondary droplet in every frame. Information such as droplet area, position, count, center of mass, shape and descriptors could be obtained. Both the raw image and the binary image could then be re-combined and manipulated to visualize the different sizes and number of the secondary droplets (**Figure 11** Frame C). Application of colour schemes

was used to differentiate between small and large secondary droplets, shown in red and green respectively.

4.1.3 Estimation of Secondary Droplet Properties

In every frame the apparent area, position and circularity² for each individual droplet was reported along with total droplet counts. Secondary droplet counts below a surface temperature of 150°C had an uncertainty of ±1% since disintegration was inertially dominated and produced large secondary droplets. The background noise particles, minimized as best as possible, represented a size of 1 pixel squared. These could be excluded from the analyses of secondary droplets for surfaces temperature below 150°C. When the surface temperature was at or above 150°C, thermally induced disintegration produced a larger range of secondary droplet sizes, with the smallest being the same size as the background noise particles. Image processing techniques minimized background noise as best as possible however some noise carried through to droplet analyses. The droplet tracking feature of the software therefore counted the background noise particles that remained. Because of this, droplet count uncertainties can increase up to ±10% for impacts on surface temperatures at or above 150°C. It should be noted that this uncertainty concerns secondary droplets that were fully developed after the initial impact. Typically, secondary droplet formation took 3-10 ms to be distinguishable by the software depending on the initial surface temperature. At early impact stages, droplet edges would merge and be identified as a single droplet rather than two or more by the software. Inaccuracies in count were most prominent in this time but could be discounted since maximum secondary droplet counts were of interest and occurred later than the 3-10 ms time frame.

Secondary droplet diameters, D , were calculated from the apparent areas of the two dimensional particles, A , measured by ImageJ and by using an appropriate pixel/length ratio³ shown in Equation (7).

$$D = 2\sqrt{\frac{A}{\pi}} \quad (7)$$

Secondary droplets with diameters less than 0.2 mm (less than 1 pixel squared in area) were excluded from the analysis since their sizes could not be detected by the high-speed camera nor through post image processing techniques.

² Circularity is a shape descriptor of a 2-D element in ImageJ;

$Circularity = 4\pi * area / perimeter^2$

³ Pixel/length ratios for each specimen surface material are reported in **Table A.1**.

Through image processing, the apparent areas of the secondary droplets were not always circular due to the irregularity of reflected light off the droplets. The circularity of the secondary droplets was measured by ImageJ and describes the roundness of an object in relation to a perfect circle. A value of 1.0 for circularity indicated a perfect circle while values approaching 0.0 described an increasingly elongated shape. Circularity refers to the roundness of an object in two dimensions and is the ratio of area to perimeter. This differs from the term sphericity, which concerns the roundness of an object in three dimensions and is the ratio of the surface area to volume. Since one camera was used in this experiment, imaging of objects is therefore in two dimensions and the definition of circularity to describe object roundness is applied over sphericity. Circularity was applied to the estimation of secondary droplet volume in order to represent a non-circular object in terms of an equivalently shaped sphere with a diameter determined by Equation (7). In this study, the circularity of small sized droplets was 1.0 – perfect circles in their 2-D apparent areas. The size of these small droplets was 0.2-0.4 mm in diameter and had no errors associated in estimating their volume or mass. As droplet sizes increase, there is an increasing likelihood that their shapes become distorted circles and therefore their circularities are smaller than 1.0. This typically occurs for large droplets with sizes greater than 0.4 mm in diameter. The resulting effect is that the volume and mass of those larger droplets are underestimated. Because of this, the relative uncertainty for secondary droplet sizes as a whole was determined to be $\pm 13\%$.

The position of the individual secondary droplets was tracked on an x-y coordinate scale where the bottom left corner represented the origin. Positive values of the position were taken to the right and upwards from the origin. Tracking by the software was accurately measured with an absolute error of only ± 0.175 mm. In terms of the x,y-direction trajectories, relative error only amounted to $\pm 2.2\%$ of the estimated distances. The velocities and accelerations of the secondary droplets were inferred by manually tracking the position of a single distinct secondary droplet evolved after impingement. Due to image processing, some secondary droplets would disappear in some frames due to background noise reduction methods and therefore necessitated manual investigation of the droplet position in each frame.

Table 5 – Uncertainties of secondary droplet properties

Property	Relative Error
Secondary droplet count	$\pm 1\%$ for surface temperatures $< 150^\circ\text{C}$ $\pm 10\%$ for surface temperature $\geq 150^\circ\text{C}$
Secondary droplet size	$\pm 13\%$
Secondary droplet position	$\pm 2.2\%$

A summary of the relative uncertainties of measured secondary droplet properties is presented in **Table 5** with additional remarks regarding uncertainties made in Appendix C.

4.2 Temperature Transient Description

Temperature transients were measured by a data-acquisition device and by Omega-XL K-type thermocouples. The information obtained from these temperature transients will be discussed.

4.2.1 Thermocouple Response Time

In these experiments, the measurement response time of the thermocouple imbedded in a material 1 mm from the impact surface was required to determine how fast temperature changes could be detected. The thermocouple sheath response time and the specimen material response time comprise the total delay time of the system.

The thermocouple sheath response time was determined experimentally. A subcooled water droplet of 6°C was dropped on a bare thermocouple tip varying in temperature from 34-43°C. Temperature measurements were recorded with corresponding high-speed images. An exponential decay of the temperature profile due to cooling was assumed. The moment the droplet impacts the thermocouple tip to the time when the temperature changes reaches 63.2% of its initial value determined the sheath response time. It was found that the sheath response time was 0.203 s.

Next, the material response time for the thermocouple to detect a temperature change at the surface and travel a depth of 1 mm to the thermocouple sheath tip was required. This was determined by using a model that assumed one-dimensional transient heat conduction with surface convection. The specimen surface temperature was varied and assumed to give off heat to the surrounding air at 25°C. A lumped capacitance analysis was applied to determine the response time of the material. It was found that material response time decreased as initial surface temperature increased. Stainless steel had an average material response time of 0.018 s while both copper and brass were 0.012 s. The total average response time was calculated to be 0.221 s for stainless steel and 0.215 s for both copper and brass. This result was in good agreement with the response time of about 0.25 s reported by the thermocouple manufacturer for an undergrounded thermocouple in water.

4.2.2 Droplet Impact Cooling Profile

Figure 12 shows a typical cooling profile of a metal specimen as it was drawn out of the furnace with a droplet impact test was performed on it. The temperature profile represents the raw measurements taken by the thermocouple over the duration of a test.

The specimen was heated slightly above the desired surface temperature to account for the temperature drop as the surface cooled after leaving the furnace and placed into position underneath the water valve. The removal of the specimen from the furnace to the desired position and initiation of the drop sequence with data devices took 4 s. In that time the temperature of the surface would decrease with as much of a maximum drop of 15°C for the highest initial surface temperature of 700°C. Temperature drops due to air cooling of the surface was less pronounced at lower surface temperatures.

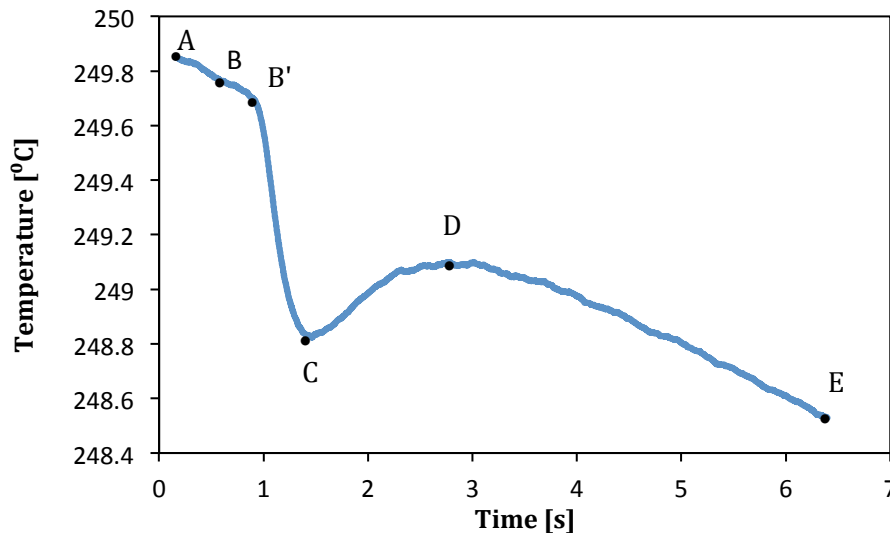


Figure 12 – A cooling profile of a curved brass surface at $T_s = 250^\circ\text{C}$ with droplet at $T_d = 25^\circ\text{C}$

The temperature drop due to surface cooling during the specimen removal process meant that the actual initial surface temperature just before droplet impact would be less than the desired value. Heating the specimen slightly above the desired surface temperature in the furnace minimized large variances caused by surface air cooling. Referring to **Table B.1** to **Table B.4** in Appendix B, the desired surface temperatures are listed under T_s , while the actual initial temperatures of the surface just before droplet impact are listed under T_i and shows very good

agreement to the desired value. T_i values represent the raw measurement of the thermocouple at that instant in time.

From **Figure 12**, point A was the moment three events were initiated simultaneously; i) water droplet release from the valve ii) camera recording iii) temperature measurement initiation. A moving average of 75 temperature measurements was implemented to reduce thermocouple noise. Because of this, the cooling profile starts at 0.152 s as the average reaches a steady state up to that point. The linear decrease in temperature from point A to point B to point B' represents the cooling of the surface by the surrounding air as the droplet descended onto the surface.

Point B was when the droplet impacted the surface and was determined by referring to the time stamp on the corresponding high-speed image. Because of the response time of the thermocouple, the temperature measurements began to see the effect of the droplet 0.215 s after it first impacted the surface at point B'. At high surface temperatures, point B and B' were equivalent due to the faster response of the thermocouple at higher temperatures. A sharp decrease in temperature was seen from point B' to a minimum, point C, as the droplet cooled the surface. The temperature drop from point B' to point C is indicative of a localized quench phenomenon.

The region on the profile from point C to point D represents the specimen's internal heat flow back into the localized region of the thermocouple. Heat flow back into the localized area of the thermocouple resulted in the slight increase in the profile. As the initial surface temperature was increased, heat flow back into the thermocouple region was overtaken by the high surface cooling rate with air resulting in a minimal increase from point C to point D. For example, the highest surface temperature case of 700°C, point C to point D was non-existent since the surface transfers its heat more readily with the surroundings. Finally, point D to point E represents the specimen surface cooling due to convective effects with air until the measurements were terminated at point E.

4.2.3 Heat Flux Estimation

The heat flux from the heated surface into the droplet was estimated by modifying Equation (4) from Section 1.3.2. Referring to the cooling profile in **Figure 12**, the temperature drop due to the droplet contacting the surface occurs in a time from point B' to point C. However, from the high-speed images, the droplet losses contact with the surface much quicker, in the order to several milliseconds. Since heat transfer can only occur during the duration the droplet resides on the surface, the time variable in Equation (4) must therefore be the residence time, t^* .

$$q'' = \frac{-k(T_{sf} - T_{si})}{\sqrt{\pi\alpha t^*}} \quad (8)$$

The residence time interval was determined from the high-speed camera images. The frame at which the droplet first contacts the surface defines the starting point from which residence time is determined. The end point of the residence time interval was taken to be the frame where majority of the secondary droplets have significantly moved away from the thermocouple location. The interpretation of this end point definition varied with the boiling regime. For cases where secondary droplets resided on the surface quiescently or fell off due to gravity, the end point frame was taken as the moment where majority of the droplets have spread radially away from the thermocouple region. For cases where secondary droplets have ejected from the surface, the end point frame was taken to be the instant the majority of the secondary droplets have lifted off the surface. This is a reasonable criterion for impacts in the film boiling regime as well. Though a vapour layer separates the liquid layer from the surface, heat transfer can still occur from the surface through the thin vapour layer to the liquid. It is only until the majority of the secondary droplets have ejected away from the surface that the heat transfer to the liquid completely ceases.

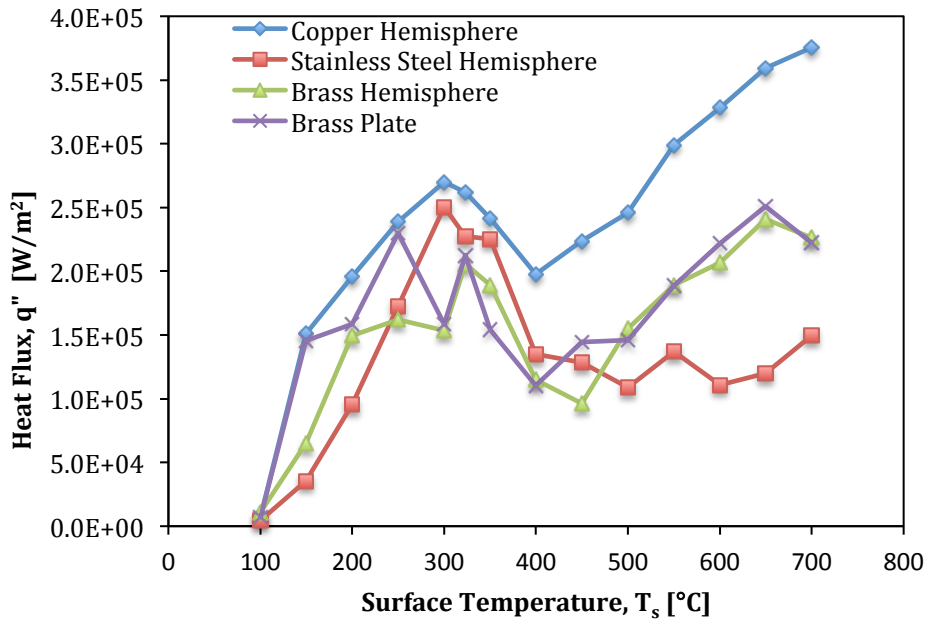


Figure 13 – Heat flux of various surfaces into the droplet

Residence times for all surfaces at various surface temperatures are reported in Appendix B, **Table B.1** to **Table B.4**. The temperature dependence of the residence time was expected and observed. It is seen to decrease as temperature increases towards the superheat limit then rise once transition and film boiling begin to occur.

The heat flux calculation assumes that the droplet absorbs the energy loss of the surface during its residence time on the surface. Equation (8) therefore represents the heat flux into the droplet. Though the heat flux equation presented here is an idealization, it provides an estimate necessary for analysis of explosive boiling force. The heat flux was plotted with surface temperature, shown in **Figure 13**. The heat flux curve will help determine the boiling regimes where explosive boiling was expected to be the most vigorous and is discussed thoroughly in the next section.

Chapter 5: Results and Discussion

Section 5.1 will give insight to the temperature regions where explosive boiling is expected to occur for the droplet-surface combinations in this study. This chapter will also describe the morphology of a droplet impact as specimen surface temperature was increased (Section 5.2.1), as the surface thermal diffusivity was varied (Section 5.2.2) and surface shape effects (Section 5.2.3) using raw image sequences. Section 5.3 will describe the set of equations and method used to estimate the explosive boiling force on a droplet. Analysis and discussion of the boiling force is made with respect; to surface temperature (Section 5.3.1), surface thermal diffusivity (Section 5.3.2), and surface shape (Section 5.3.3). The effect of the boiling force on how secondary droplets are created is discussed in Section 5.4 with emphasis on secondary droplet count, size and trajectory distribution.

5.1 Surface Temperature Regions of Explosive Boiling

Discussed in this section are the expected temperature regions where explosive boiling is encountered. The superheat limit temperature, also known as the spontaneous homogeneous nucleation temperature, and the Leidenfrost point define this region.

5.1.1 Spontaneous Nucleation Temperature

The instantaneous interface temperature of a droplet contacting a hot surface can be calculated by Equation (6) from Section 1.3.2. The interface temperature is relevant since it defines the boiling mode that is present upon droplet contact with the surface. If the interface temperature is at the superheat limit temperature then homogeneous nucleation is likely to occur in the droplet spontaneously and that explosive boiling would follow (Inada et al., 1996).

It follows from Equation (6) that the interfacial temperature is one that is higher than the initial droplet temperature but below the initial specimen surface temperature. **Figure 14** shows the respective interfacial temperatures for a given initial surface temperature for all material types. Also shown, as dotted horizontal lines in **Figure 14**, are the estimated bounds of the superheat limit temperature (T_{sl}) as reported by several authors; Avedisian 1985, Glod et al., 2002 and Shepherd et al., 1982. The bounds of the superheat limit temperature are 283-313°C.

From the **Figure 14**, if the interfacial temperature for a given droplet-surface combination is within the area bound between the upper and lower superheat limit

temperature values, then explosive boiling is expected to occur. For example, a copper hemisphere surface initially at $T_s = 300^\circ\text{C}$, impacted by a droplet at $T_d = 25^\circ\text{C}$, gives an instantaneous interface temperature of $T_{int} = 289^\circ\text{C}$ and would explosively boil. This is later confirmed in Section 5.2 when observing the morphological characteristics of impacts.

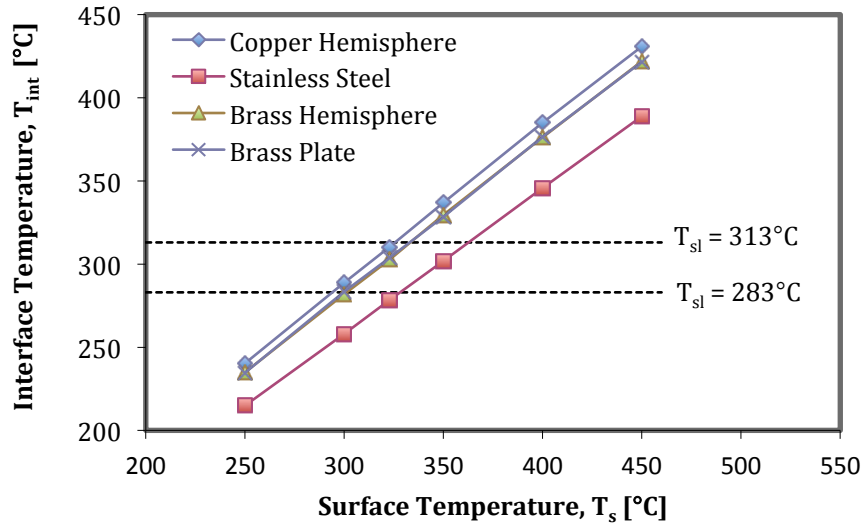


Figure 14 – Instantaneous interface temperatures for various surfaces

By interpolating the superheat limit bounds to each surface material trend line, explosive boiling is expected to occur when the initial surface temperatures are between $294\text{--}326^\circ\text{C}$ for copper, $300\text{--}333^\circ\text{C}$ for brass and $321\text{--}355^\circ\text{C}$ for stainless steel. These ranges show that; i) lower effusivity surfaces such as stainless steel require greater surface temperatures to initiate explosive boiling compared to high effusivity surfaces like copper; ii) a greater surface temperature range exists for lower effusivity materials for which explosive boiling is possible.

An additional consideration is given to the wettability of the liquid at the interface of the solid. Cronenberg (1980) proposed that the spontaneous nucleation temperature can be reduced due to imperfect wetting. For perfect wettability, the contact angle is 0° and gives a spontaneous nucleation temperature similar to those reported in **Figure 14** of $283\text{--}313^\circ\text{C}$ (Fletcher & Theofanous, 1997). Increasing the contact to 80° can result in the spontaneous nucleation temperature to reduce to 209°C . This example shows the dependence of spontaneous nucleation on surface wetting characteristics. The next section considers the wetting characteristics of the transition and film boiling regimes as it pertains to the discussion of explosive boiling conditions.

5.1.2 Leidenfrost Temperature

The Leidenfrost temperature point is significant regarding the superheat limit temperature because it functions as the upper temperature bound from which explosive boiling will not occur.

For a surface that has an interface temperature above the superheat limit temperature but below the Leidenfrost temperature, the droplet will initially boil in the transition boiling regime. However, the interface temperature decreases with time due to convection and phase changes (Fujimoto et al., 2010). If the liquid wets the surface sufficiently long enough for the interface temperature to reduce, then the droplet can enter the superheat limit temperature region. Initiation of an explosive boiling event can potentially occur despite the droplet having less wettability at the interface with the solid due to transition boiling.

If the droplet achieves the Leidenfrost temperature, the vapour layer that is formed underneath the liquid is effective at preventing liquid superheating on a scale conducive to explosive boiling. It is prudent to identify the Leidenfrost temperature for which film boiling becomes stable enough to prevent explosive boiling conditions. Identifying the Leidenfrost temperature is difficult due to its dependence on a variety of parameters such as; pressure, mass of liquid, impact velocity, liquid subcooling, heated surface thermal properties, and surface roughness (Bernardin et al. 1997). As a result, a wide variation in the Leidenfrost temperature for water have been reported in literature. Application of existing correlations would yield inaccuracies because of varying experimental conditions. In this current study, the Leidenfrost temperature is identified at the minimum heat flux point and is simply determined from the heat flux curve, **Figure 13**. The values are summarized below in **Table 6** for the different surfaces.

Table 6 – Leidenfrost temperature of water on various surfaces

Surface Material	Leidenfrost Temperature [°C]
Copper Hemisphere	400
Brass Hemisphere	450
Brass Plate	400
Stainless Steel Hemisphere	500

For comparison, Borishansky (1953) estimated the Leidenfrost temperature of a water droplet (diameter = 4.5 mm, subcooling = 20°C) at 250°C and 222°C on a copper and brass surface respectively. The values reported in this current study are much higher and are attributed to high impact velocity that the droplet

impinges on the surface. A study by Gradeck, Seiler, Ruyer, & Maillet (2013) showed that the Leidenfrost temperature of water increased as the Weber number was increased but did not attribute a mechanism to explain the dependence. For this current study, the morphological characteristics presented in the next section will provide visualization and validity of the expected temperature regions of explosive boiling.

5.2 Impact Morphology

5.2.1 Effect of Surface Temperature

This section will focus on visual characteristics of droplet impacts as the specimen surface temperature was increased from $T_s = 30^\circ\text{C}$ to 700°C . For simplicity, the droplet impact characteristics with respect to temperature will be described using the curved brass specimen. The effect of varying the surface material type on impact morphology will be discussed in Section 5.2.2 and 5.2.3.

The droplet impact at an ambient surface temperature of $T_s = 30^\circ\text{C}$ is depicted in **Figure 15**. The compression of the droplet was due to the dissipation of droplet kinetic energy into the radially outward spreading of the droplet as a thin circular disk on the surface at $t = 1$ ms.

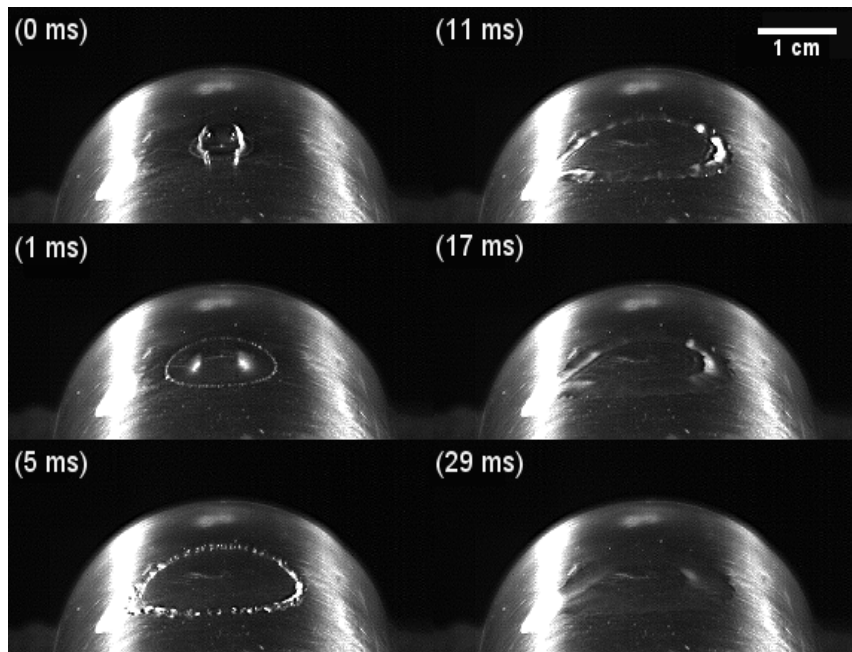


Figure 15 – Water droplet impact on curved brass surface at $T_s = 30^\circ\text{C}$

A ridge formed on the outer edge of the spreading droplet and had a thicker layer than the center of the droplet. Liquid layer thickness cannot be measured from these experiments directly, however it can be inferred that a thicker layer was present at the droplet edge due to the brighter reflection of light in the outer ridge compared to the center. The spreading of the droplet advanced until it reached a maximum diameter of 2.23 cm at $t = 5$ ms in which surface tension acts to restrict the spreading of the droplet. After spreading ceases, the droplet began to contract inwards as its surface area lessens. The outer ridge began to flatten as the droplet reached a static state on the surface at $t = 29$ ms. The surface temperature was well below the incipience of boiling for water and thus the droplet appeared transparent on the surface.

Figure 16 depicts the droplet interaction when the surface temperature was just to the point of boiling initiation at $T_s = 100^\circ\text{C}$. The increase in temperature from ambient conditions showed that the maximum spread diameter reduced to 2.15 cm at $t = 5$ ms.

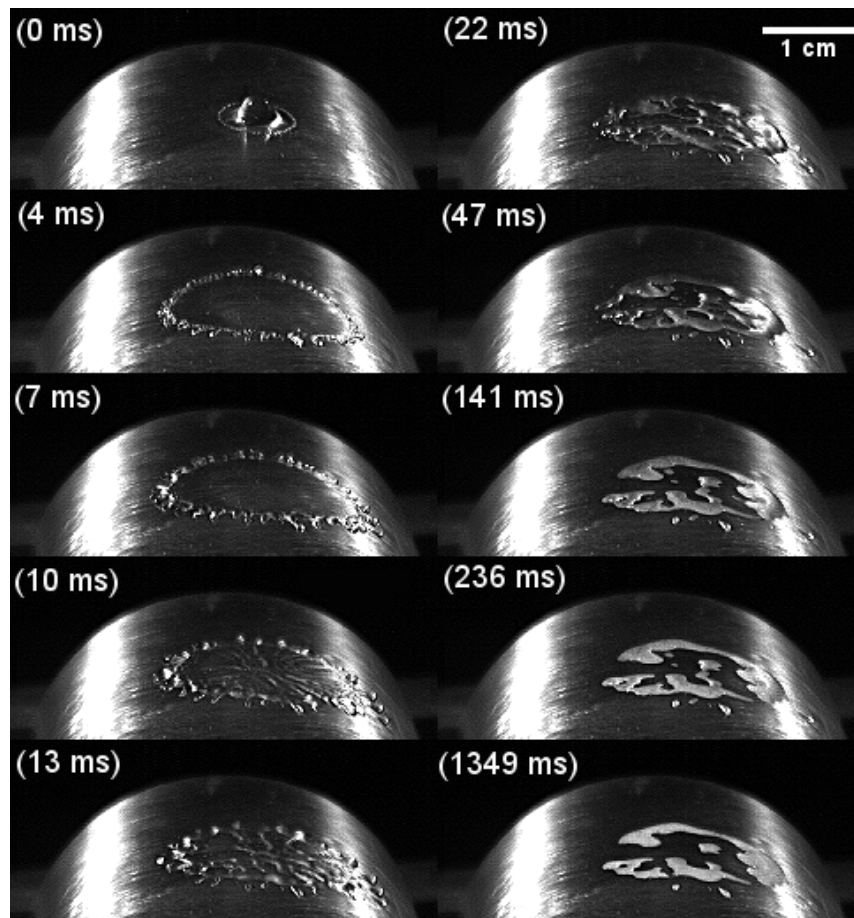


Figure 16 – Water droplet impact on a curved brass surface at $T_s = 100^\circ\text{C}$

With **Figure 16**, the outer edge showed the beginnings of initial droplet fragmentation at $t = 4$ ms and became more evident as the droplet spread. This was seen as small finger like droplets that extended away from the droplet's outer edge. Increasing surface temperature reduces surface tension that results in the fingering effect of the droplet minimizing its energy state by spreading over a greater surface area. This effect was also responsible for the non-uniform inward contraction of the droplet creating dry spots seen in frames $t = 10$ ms to 47 ms. The cohesive forces of the liquid were insufficient for the recoiling droplet to transverse the microscopic surface cavities and thus distinct regions of wetting and non-wetting were produced. Disintegration of the initial droplet was minimal in that the secondary droplets produced were very large, low in count and non-spherical. Secondary droplets were created from an inertia break up mechanism and lay quiescently on the specimen surface while absorbing surface heat. Comparing frames at $t = 47$ ms, 141 ms, and 236 ms, the secondary droplet fragments progressively became brighter, signifying the presence of tiny vapour bubbles arising from heterogeneous nucleate boiling.

Figure 17 depicts droplet impact on a surface at $T_s = 150^\circ\text{C}$ and showed the first signs of secondary droplet ejection due to splashing.

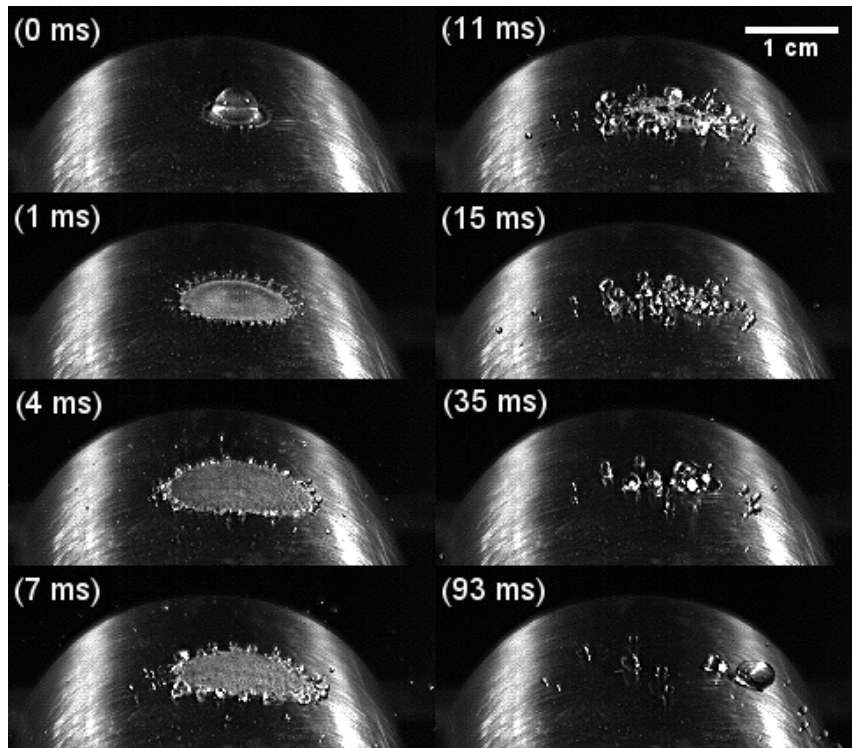


Figure 17 – Water droplet impact on a curved brass surface at $T_s = 150^\circ\text{C}$

The temperature reduction of the droplet's surface tension, in combination with the inertial energy dominance in the early impact stages, resulted in secondary droplet ejection occurring promptly at $t = 1$ ms in **Figure 17** from splashing. The liquid finger projections at the advancing edge of the spreading droplet appeared more spherical at $t = 4$ ms and 7 ms and lead to early formation of secondary droplets. The break up of the spreading droplet was the most severe during the recoil stage after it attained its maximum spread diameter on the surface at $t = 4$ ms. The initial droplet contracted and coalesced droplets from the outer edge with liquid in the interior from $t = 7$ ms to 15 ms. The secondary droplets evolved from the droplet contraction phase did not eject from the surface but moved laterally across it until they fell off the sides. The secondary droplets evolved from the recoil stage were much larger in diameter than the secondary droplets ejected during splashing.

As the specimen surface temperature was increased to $T_s = 200^\circ\text{C}$, secondary droplet ejection occurred from splashing and recoil break up. As the surface temperature was increased, a greater number of secondary droplets were observed to eject from the initial droplet periphery during splashing. Secondary droplets from splashing started at $t = 1$ ms and continued to $t = 4$ ms in **Figure 18**.

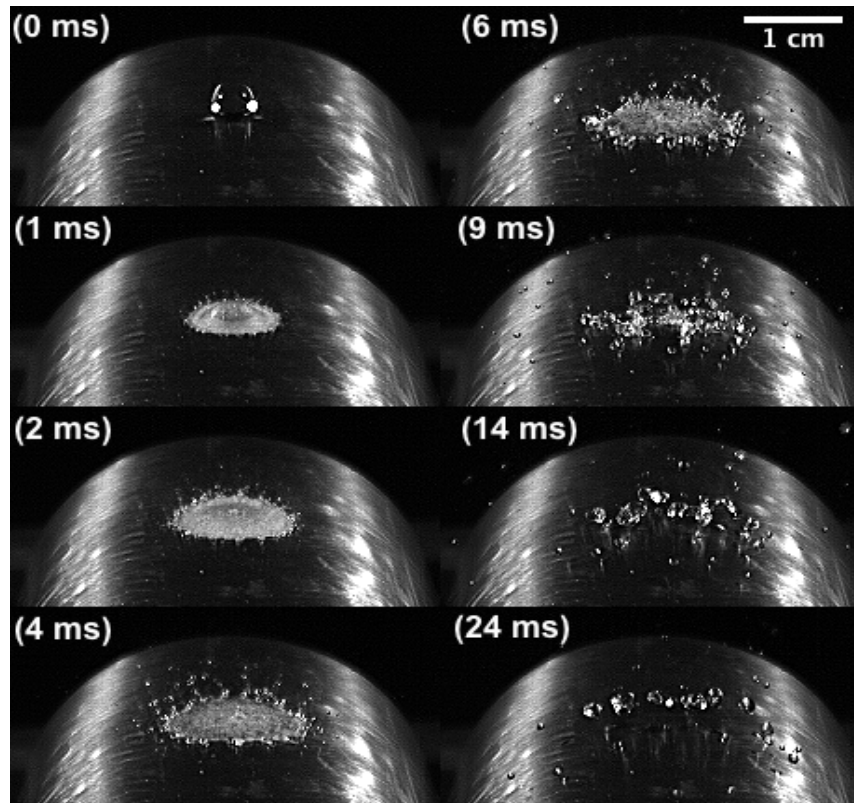


Figure 18 – Water droplet impact on a curved brass surface at $T_s = 200^\circ\text{C}$

The initial droplet was observed to contract inward again producing secondary droplets that ejected from the surface at this instance. The superheat was considered to be large enough that the evolution of vapour bubbles and their collapse had enough energy to lift secondary droplets off of the surface. The secondary droplets from splashing ejected more vertically than the larger secondary droplets from thermal break up. The time scale for splashing was much shorter than contraction break up and thus the secondary droplets evolved from splashing conserve greater initial kinetic energy and escape the surface with higher velocities. The kinetic energy was dissipated through the spreading and recoil of the droplet on the surface. Thus, secondary droplets ejected upwards after recoiling have lower escape velocities. The impact shown in **Figure 18** is an example where boiling effects contribute to the overall disintegration of the droplet. The roughening of the liquid surface due to vapour contributes to the early formation of secondary droplets that would be ejected towards the end of the impact outcome.

Once a surface temperature of $T_s = 250^\circ\text{C}$ was reached, depicted in **Figure 19**, the droplet contraction phase disappeared. Secondary droplets formed by the inward recoil of the droplet on itself were not observed at this surface temperature. Instead, the beginning of an explosive blow out of secondary droplets was observed to originate from the center during the spreading of the initial droplet.

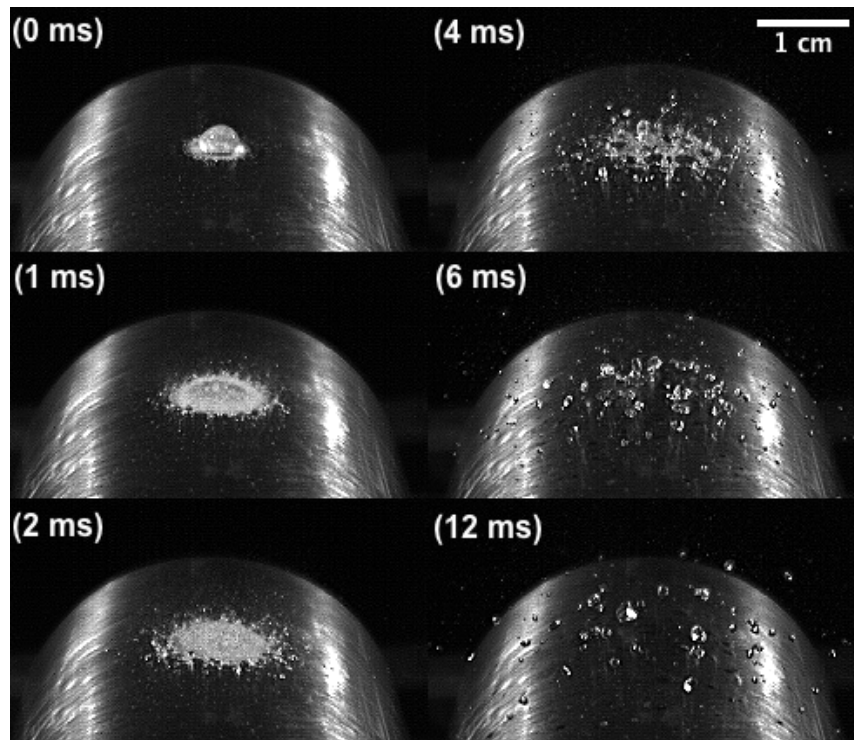


Figure 19 – Water droplet impact on a curved brass surface at $T_s = 250^\circ\text{C}$

The roughening of the liquid surface at $t = 2$ ms in **Figure 19** indicated the presence of vapour bubbles pushing upwards on the droplet. The higher nucleation rate attributed to higher surface superheats results in a more violent production and collapse of vapour bubbles that penetrate into the liquid layer. Complete disintegration of the initial droplet occurred at $t = 4$ ms with secondary droplet ejection occurring over a greater distributed area than previous surface temperature cases. This temperature case showed a break up mechanism that was influenced more by thermally induced effects of boiling. It should be noted that inertial break up was still present; only in the early stages of impact that produce secondary droplets from splashing. The majority of the initial droplet was however disintegrated by thermal effects. The thermal effects are much more energetic in that the secondary droplets eject with velocities greater than they would through splashing.

When the specimen surface temperature was at $T_s = 300^\circ\text{C}$, the most catastrophic disintegration of the droplet was observed on a very short time scale and is depicted in **Figure 20**. Morphological characteristics indicated that the droplet explosively boiled and agreed with the expectation that it would in the $T_s = 300\text{-}333^\circ\text{C}$ temperature range as shown in interface temperature graph in Section 5.1, **Figure 14**.

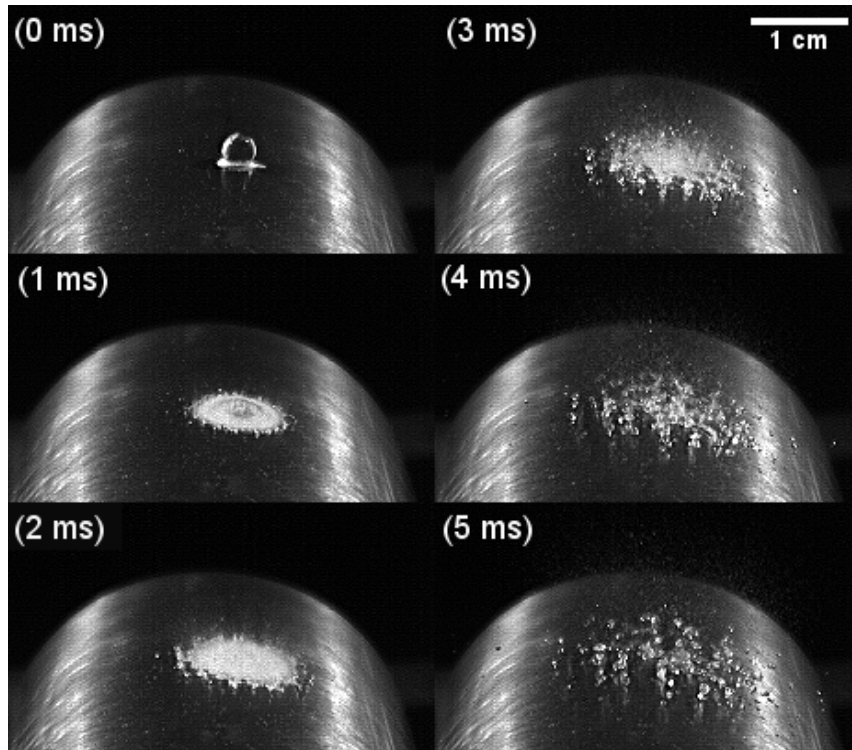


Figure 20 – Water droplet impact on a curved brass surface at $T_s = 300^\circ\text{C}$

The intensity of the boiling was the most vigorous as evidenced by the brightness of the droplet on the surface at $t = 1$ ms and 2 ms in **Figure 20**. A highly unstable liquid/solid interface was present at $t = 2$ ms where ripples were seen at the center of the droplet due to the high nucleation rate of vapour bubbles. Forceful ejection of vapour, normal to the surface, fragmented the liquid layer above and ejected a fine mist of secondary droplets in frame $t = 2$ ms. Fine secondary droplets were projected upwards with large velocities while larger secondary droplets ejected radially outwards from the periphery of the bulk droplet from $t = 3$ ms to 5 ms.

Fine secondary droplets were difficult to distinguish from the raw image sequences however image processing techniques highlighted their presence. Results of image processed sequences will be shown later in Section 5.3, which concern the estimation of explosive boiling force.

For $T_s = 300^\circ\text{C}$, the droplet achieved a maximum spread diameter of 1.13 cm with a residence time of 3 ms on the surface and were the lowest values obtained over the range of surface temperature studied. Thermally induced break up occurred the quickest at this surface temperature and produced secondary droplets that were as small or smaller than those evolved from splashing.

Figure 21 depicts a droplet impact on surface at $T_s = 350^\circ\text{C}$ and showed a less intense vapour explosion than at $T_s = 300^\circ\text{C}$. From **Figure 21** frames $t = 1$ ms to $t = 3$ ms, a clear demarcation of three different regions of the impacting droplet are seen.

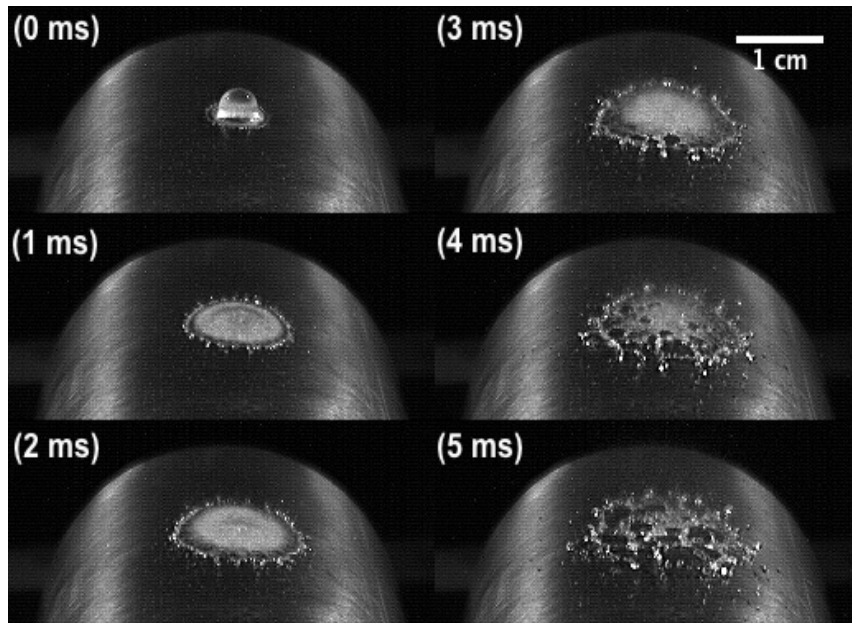


Figure 21 – Water droplet impact on a curved brass surface at $T_s = 350^\circ\text{C}$

First was the bright circular disk at the center, then a darker ring, and then a crown formation of splashing droplets at the periphery in **Figure 21**. The advancing edge of the bulk droplet spread to a maximum diameter of 1.6 cm, yet the interior circular disk remained constant at a diameter of 1.02 cm from $t = 1$ ms to 3 ms. This interior disk was a region of wetting where the liquid contacted the specimen surface resulting in a high heat transfer region. The darker ring around the interior disk indicated a region of low heat transfer due to a vapour layer insulating the liquid from the surface. As the droplet spread on the surface, the interfacial temperature decreased with time and the vapour layer was observed to reduce in size. The progression back to a nucleate boiling mode occurred when the liquid reestablished contact with the surface. The partial re-wetting of the dark ring region was observed as lighter bands or spots at $t = 2$ ms and $t = 3$ ms. At $t = 3$ ms, the interior disk shape appeared to distort as vapour began projecting upwards through the liquid layer finally breaking through and releasing fine secondary droplets at $t = 4$ ms.

From Section 5.1 **Figure 14**, a surface at $T_s = 350^\circ\text{C}$ for brass was outside the explosive boiling temperature range and suggests that the droplet will initially boil in the transition boiling regime. However, with sufficient liquid contact with the surface, the interfacial temperature can decrease with time and enter the superheat limit temperature bounds, creating a vapour explosion. The morphological outcome shown in **Figure 21** confirms this, as the central disk region of wetting is the origin of a less intense explosive boiling event.

Figure 22 depicts a droplet impact on a surface at $T_s = 400^\circ\text{C}$ and showed the beginnings of a departure from explosive blow out of fine secondary droplets with greater stability of the vapour layer formed in the circular disk region in the initial droplet. According to previous calculations, the droplet is still expected to be in the transition boiling regime. However, with an increase in temperature, surface wetting becomes increasingly difficult and more intermittent despite the interfacial temperature decrease.

Initial heat transfer to the liquid was the most intense at $t = 1$ ms and then subsequently lessens in later frames as seen by the gradual darkening of the center disk region. The light spots were regions where the liquid wetted the surface and thus boiled. The growth of the dark regions within the central disk from $t = 3$ ms to $t = 6$ ms was due to the coalescence of the vapour layer reducing the contact between the solid surface and the liquid. Fragmentation of the bulk droplet was mostly from the inward shrinking of the droplet after attaining maximal extension on the surface. The coalescence of secondary droplets from the outer periphery, a morphology that was observed in the $T_s = 200^\circ\text{C}$ surface temperature case, was also observed here. The blow out of fine secondary droplets from the center was considerably less in count and distributed area than the $T_s = 300^\circ\text{C}$ or 350°C case.

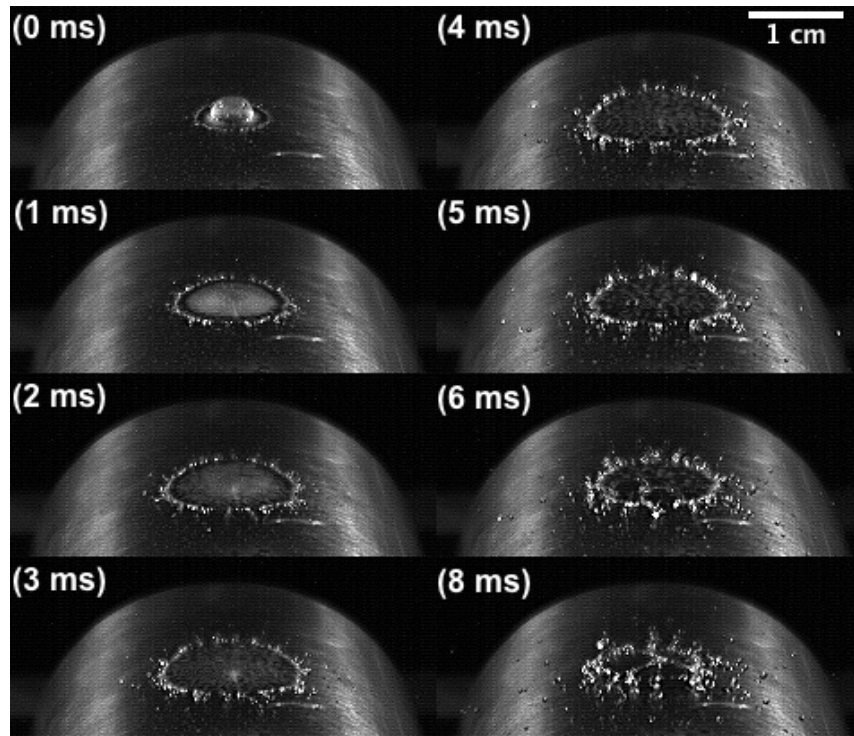


Figure 22 – Water droplet impact on a curved brass surface at $T_s = 400^\circ\text{C}$

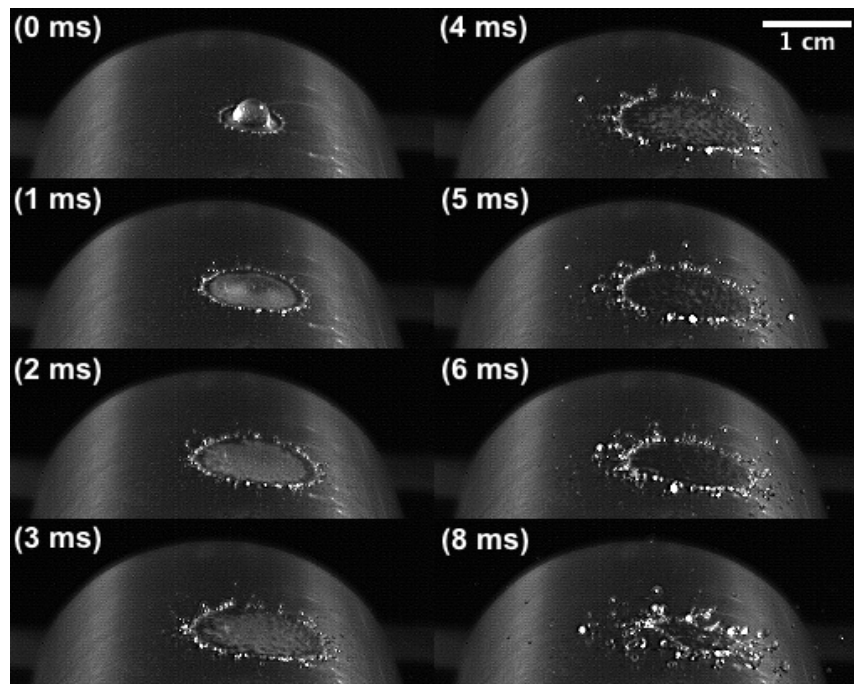


Figure 23 – Water droplet impact on a curved brass surface at $T_s = 500^\circ\text{C}$

As the surface temperature was raised well above the superheat limit of the droplet, the droplet impact characteristics become near identical due to the presence of an ever stable vapour layer that reduces thermal atomization effects. **Figure 23** shows a droplet impact on a surface at $T_s = 500^\circ\text{C}$. The vapour layer appeared to form quicker as the surface temperature was increased into the film boiling regime. Comparing frames $t = 5$ ms and $t = 6$ ms in both **Figure 22** and **Figure 23** show that the coalescence of vapour occurred quicker in the $T_s = 500^\circ\text{C}$ surface temperature case. This can be seen by the fewer number of wet spots in the spreading droplet at $T_s = 500^\circ\text{C}$. This morphology, in accordance with the Leidenfrost temperature of 450°C for brass, suggests that the impact occurred in the film boiling regime and that explosive boiling is no longer possible. Additionally, this means that thermal break up is no longer contributing to liquid disintegration and ejection of secondary droplets. Instead, inertial break up is allowed to dominate and is responsible once film boiling is stably developed.

The disappearance of wet regions initially appeared random until a surface temperature of $T_s = 550^\circ\text{C}$ was investigated and shown in **Figure 24**. At earlier impact times, the same regions of wetting and non-wetting with crown formation of secondary droplets in the periphery was observed.

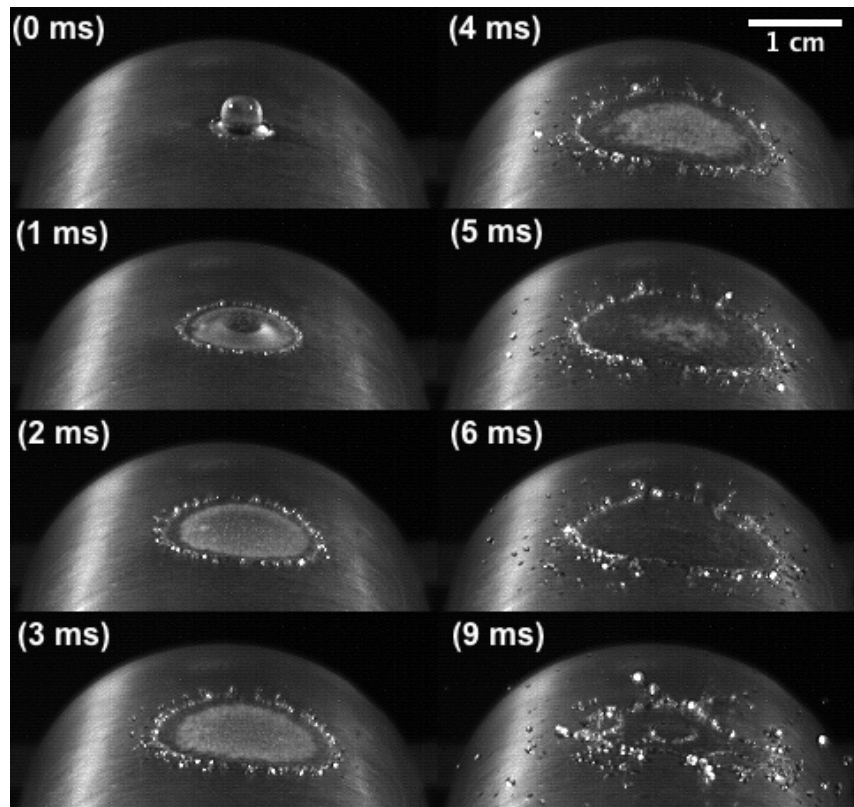


Figure 24 – Water droplet impact on a curved brass surface at $T_s = 550^\circ\text{C}$

However, in **Figure 24** after $t = 3$ ms, the center disk region of wetting appeared to shrink inwards followed by bulk droplet recoil and disintegration.

Figure 25 and **Figure 26** depicts droplet impacts at $T_s = 600^\circ\text{C}$ and $T_s = 700^\circ\text{C}$ respectively. From these impacts, it was observed that once the surface temperature was above $T_s = 550^\circ\text{C}$, the central wetted region lost contact with the surface beginning from the periphery and moved towards the center of the bulk droplet. The inward shrinking of the wetted region can also be seen from $t = 3$ ms to $t = 5$ ms in both **Figure 25** and **Figure 26**. The shrinking of the wetted area occurred quickest for the highest surface temperature case of $T_s = 700^\circ\text{C}$ where the formation of vapour is expected to be the fastest and the thickest during the droplet's residence time of the surface.

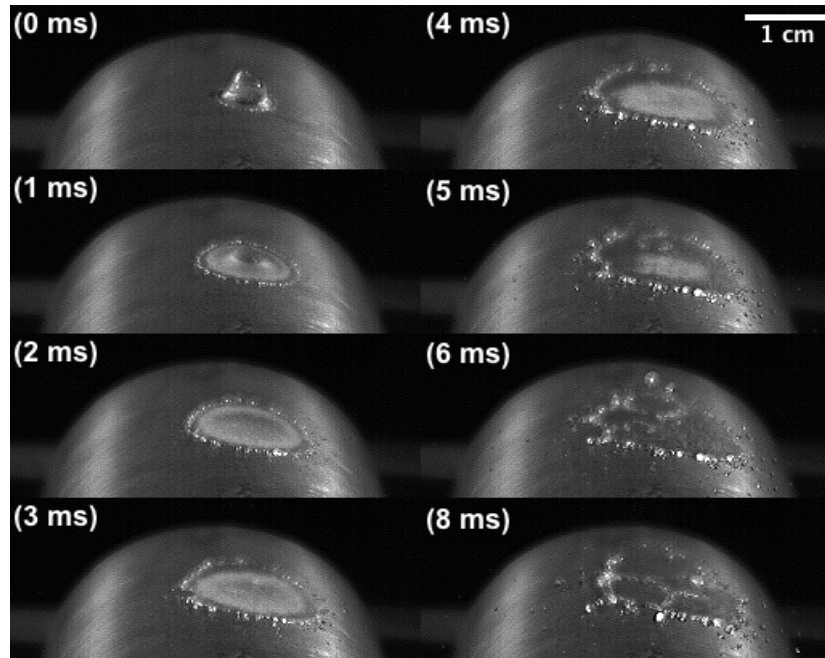


Figure 25 – Water droplet impact on a curved brass surface at $T_s = 600^\circ\text{C}$

In general for impacts occurring above 400°C , the initial circular disk region in which wetting the surface occurred was observed immediately after impact. Within 2 ms after impact, the combination of the droplet's inertial force and lack of stable vapour layer contributed to the presence of the wetted circular region. As the inertial energy was dissipated by the droplet periphery spreading on the surface so too does the wetted circular region. After this point, greater vapour production began to reduce liquid/surface contact and eventual recoil of the drop occurred atop the vapour layer.

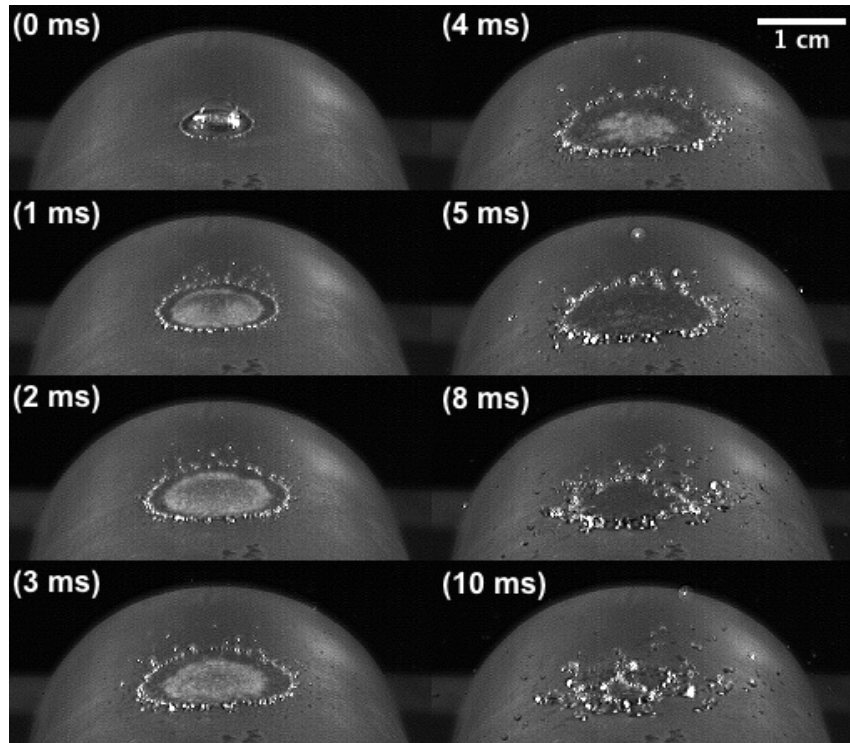


Figure 26 – Water droplet impact on a curved brass surface at $T_s = 700^\circ\text{C}$

The maximum spreading diameter of the droplet impacts in the film boiling regime was equivalent to those observed in low superheat temperatures in the nucleate boiling regime. Increases in surface temperature within the film boiling regime did not appear to affect maximum spreading diameter and the time at which complete droplet break up occurred.

The explosive blow out of fine secondary droplets was subdued in the film boiling regime. The secondary droplets that were formed are due to the recoiling of the initial droplet and coalescence of periphery droplets. The presence of a vapour layer drastically reduced the thermal atomization of secondary droplets. The ejection of small secondary droplets originating from the centre reduced as temperature was increased in the film boiling region. As a result, only large secondary droplets were formed during the late stages of initial droplet contraction. Secondary droplets ejected with lower velocities and distributed in a flatter trajectory once vapour regions appeared on the surface as the droplet spread.

5.2.2 Effect of Thermal Diffusivity

The effect of varying thermal diffusivity of a surface on droplet morphology can be observed in the figures provided in this section. The copper surface ($\alpha_{Copper} = 1.17 \times 10^{-4} \text{ m}^2/\text{s}$), featured the highest thermal diffusivity, followed by brass ($\alpha_{Brass} = 3.39 \times 10^{-5} \text{ m}^2/\text{s}$) then stainless steel ($\alpha_{Stainless\ Steel} = 3.48 \times 10^{-6} \text{ m}^2/\text{s}$).

The droplet impact shown in **Figure 27** shows a variance in impact outcomes within the nucleate boiling regime. The highest diffusivity surface of copper showed greater droplet break up from splashing at $t = 1 \text{ ms}$ and during droplet recoil compared to the lowest diffusivity surface of stainless steel. The secondary droplets produced on copper and brass were more numerous and fell off the surface compared to the secondary droplets on stainless steel that lay quiescently until evaporation. A likely cause was due to the proportional influence of diffusivity on the transient heat flux in to the droplet (Cossali et al., 2006). For copper, a higher diffusivity will result in the droplet absorbing more thermal energy quicker and attain boiling regimes faster than a droplet residing on a stainless steel surface. With this consideration, the temperature reduction of viscous forces is greater for the liquid on a copper surface than stainless steel, hence a greater degree of liquid break up on a copper surface.

Additionally, the time scale of morphological developments is also influenced by thermal diffusivity. The residence time of a droplet on a high diffusivity surface was less than a low diffusivity surface as seen in **Figure 28**. At 7 ms in **Figure 28**, the secondary droplets were well developed and have ejected from the surface for copper and brass yet a portion of the initial droplet remained in contact with the stainless steel surface.

The trend of earlier break time and severity continued for the high diffusivity surface in **Figure 29** where the surface temperature was the most favorable to explosive boiling conditions at $T_s = 300^\circ\text{C}$. By $t = 5 \text{ ms}$, complete break up of the droplet on the copper surface has already occurred while on stainless steel a small region in the center of the droplet was still spreading where secondary droplets have yet to fully depart the surface. This shows that though a droplet resides on the surface for a shorter time period, the heat deposition into the droplet is significantly greater during that time on a higher thermal diffusivity.

From **Figure 29**, the copper and brass surfaces exhibited very similar morphologies with very little visual differences stemming from the raw images. However in Sections 5.3 and 5.4, differences in explosive boiling force and secondary droplet characteristics that are not initially observed from the raw images will be highlighted.

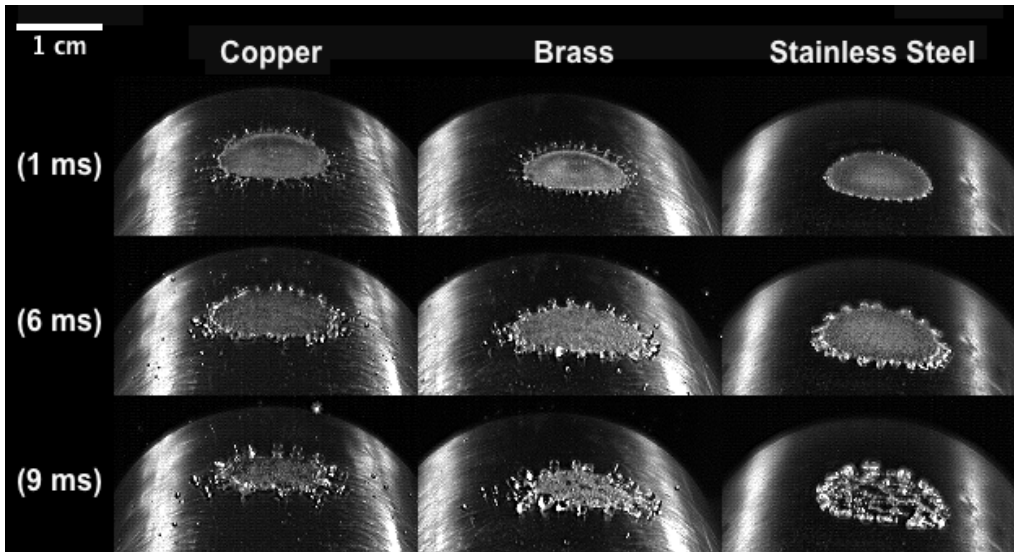


Figure 27 – Water droplet impacts on various heated surfaces at $T_s = 150^\circ\text{C}$

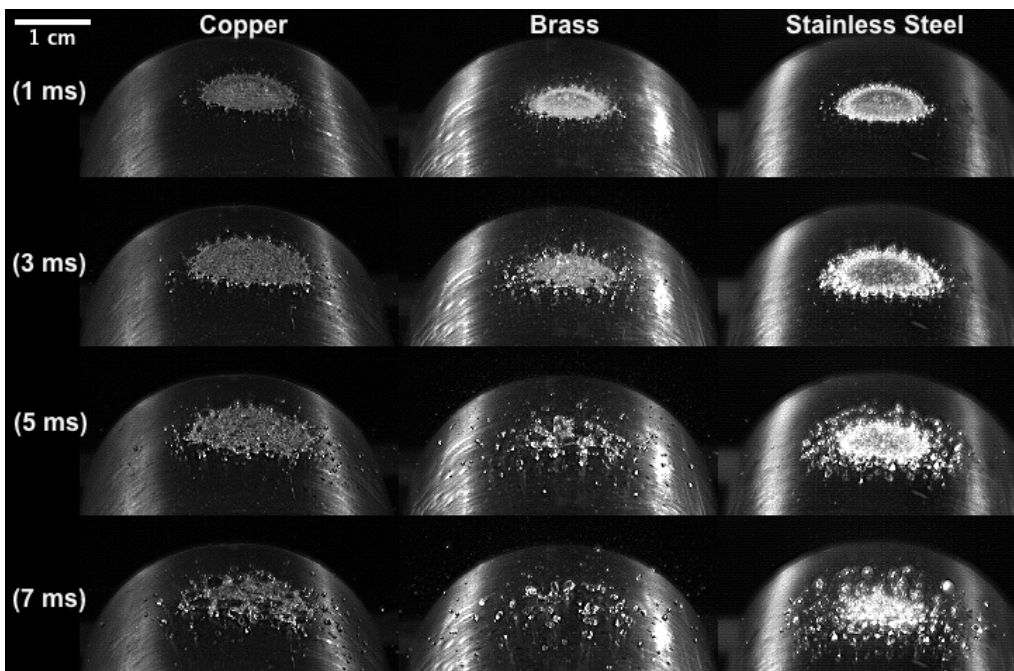


Figure 28 – Water droplet impacts on various heated surfaces at $T_s = 250^\circ\text{C}$

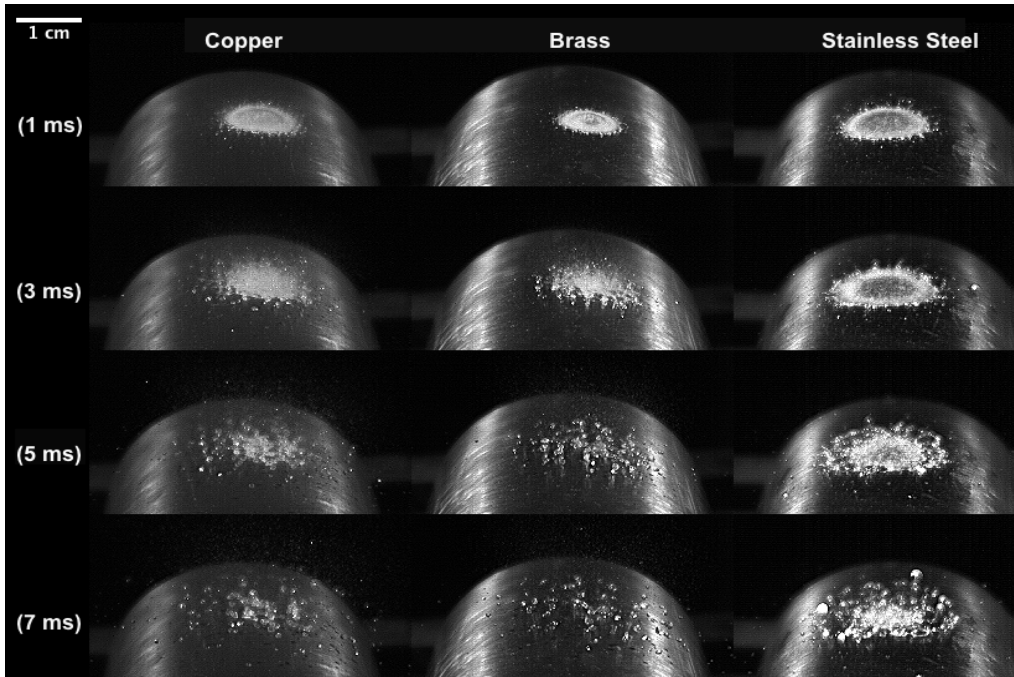


Figure 29 – Water droplet impacts on various heated surfaces at $T_s = 300^\circ\text{C}$

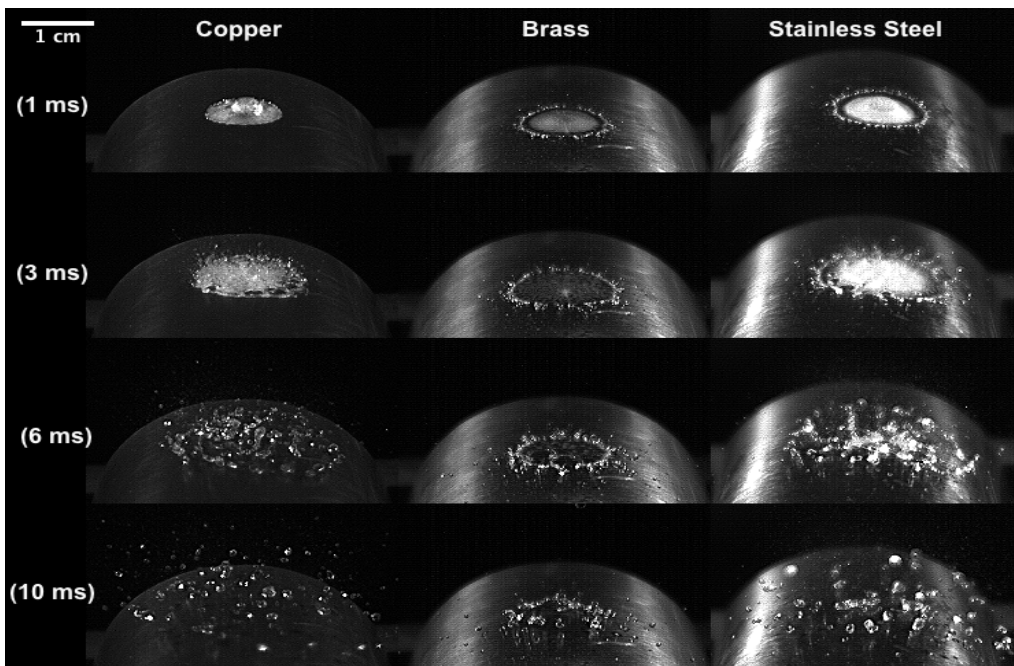


Figure 30 – Water droplet impacts on heated surfaces at $T_s = 400^\circ\text{C}$

As the surface temperature increased away from explosive boiling conditions, a variety of impact outcomes were observed due to the random nature and unpredictability of the liquid contact that is associated with the transition boiling regime, as shown in **Figure 30**. The stainless steel surface showed a much more energetic droplet break up than the others at $T_s = 400^\circ\text{C}$. An explosive blow out was observed to originate from the spreading droplet's center at $t = 3$ ms. The low thermal diffusivity of stainless steel caused a slower progression through the different boiling modes compared to copper. From **Figure 30**, it appears that the droplet was still within the explosive boiling temperature range for stainless steel despite its interface temperature being out of range of the superheat limit temperature bounds.

Brass clearly appeared to be past explosive boiling conditions evidenced by the regions of wetting and non-wetting as the droplet spread. An increasing presence of a vapour layer was observed to form and thus the break up of the droplet on the brass surface was less intense and slower. The copper surface would be expected to produce a similar result to brass since the thermal inertia of copper is higher. However, the droplet appeared to wet the copper surface and break up in a morphology conducive to explosive boiling, albeit in a slower timescale. Secondary droplets, large in nature, appeared to eject away from the surface with greater velocity than the impacts occurring on brass or stainless steel.

An explanation for this can be noted from **Figure 30** by the darkening of the copper surface that indicated the formation of an oxide layer. The thermal resistance of an oxide layer impedes heat transfer to a droplet residing on the surface (Wendelstorf, Spitzer, & Wendelstorf, 2008). As a result, the droplet impact on a copper surface at 400°C was similar to an impact outcome characteristic of a lower surface temperature in the nucleate boiling regime. Though copper has a higher thermal diffusivity than brass, the presence of a greater oxidized layer on the copper surface delayed progression of heat transfer into the transition boiling regime. The effect of oxide layers delaying the progression into the onset of transition boiling regime has been reported in literature (Negeed, Hidaka, Kohno, & Takata, 2013; Viscorova, Scholz, Spitzer, & Wendelstorf, 2006; Wendelstorf et al., 2008). This, in combination with the interfacial temperature reduction of a droplet on a copper surface, can provide enough liquid contact with the surface to just reach near the upper superheat limit bound. Furthermore, the Leidenfrost temperature is also higher when oxide layers form. Once a surface temperature of 450°C was attained for copper, the droplet appeared to boil in the transition boiling regime, characterized by the wetted and non-wetted regions as the droplet spread.

Once the surface temperature increased past the Leidenfrost point, vapour layer production was more prominent in droplet impacts for all surfaces. A higher thermal diffusivity resulted in the quicker formation of a vapour layer that

supported the liquid before break up. This can be seen by comparing the brass and stainless steel surfaces in **Figure 31** at $t = 3$ ms and 5 ms. The central region of the spreading droplet appeared to grow darker on the brass surface, signifying a growing vapour layer due to its higher diffusivity than stainless steel. Droplet recoil on the vapour layer and subsequent disintegration also occurred quicker on the higher diffusivity material.

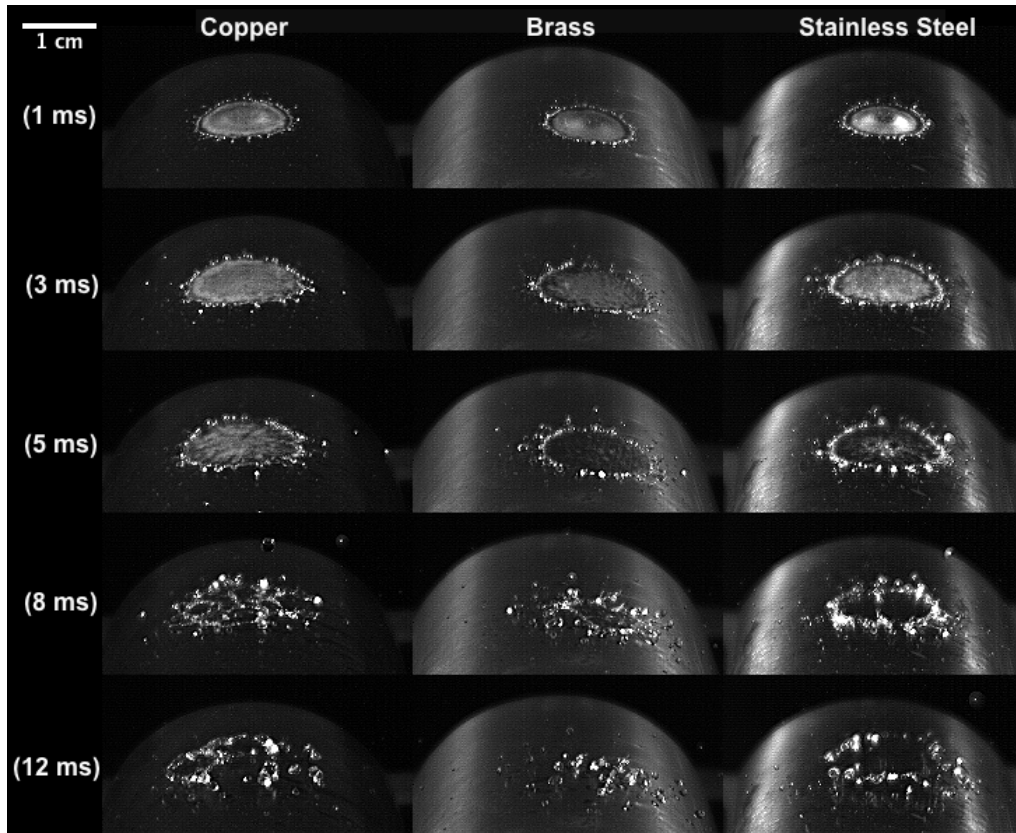


Figure 31 – Water droplet impacts on heated surfaces at $T_s = 500^\circ\text{C}$

At $T_s = 600^\circ\text{C}$, depicted in **Figure 32**, brass and stainless steel surfaces further showed examples of vapour layer production and coalescence. Interestingly, the droplet appeared to explode on the copper surface at 600°C and was not expected. A possible explanation can be attributed to oxide layer being thinner and allowing a greater amount of heat to penetrate through to the surface at this temperature. A study by Wan, Wang, Sun, Li, Zhang, & Wu (2012) investigated copper oxidation at high temperatures using differential scanning calorimetry. A minimum point was obtained at 580°C in their calorimetry analysis to which the authors suggested it occurred because the oxide layer broke away from the copper specimen. A similar phenomena is postulated to have occurred in this present

study where the copper surface allowed for re-initiation of explosive boiling at 600°C.

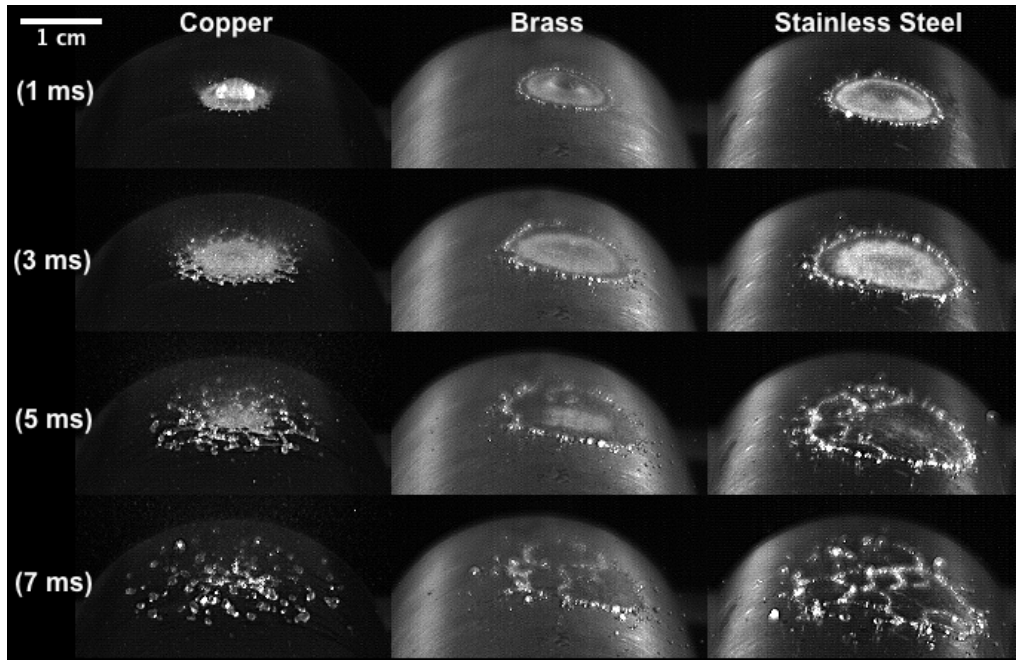


Figure 32 – Water droplet impacts on heated surfaces at $T_s = 600^\circ\text{C}$

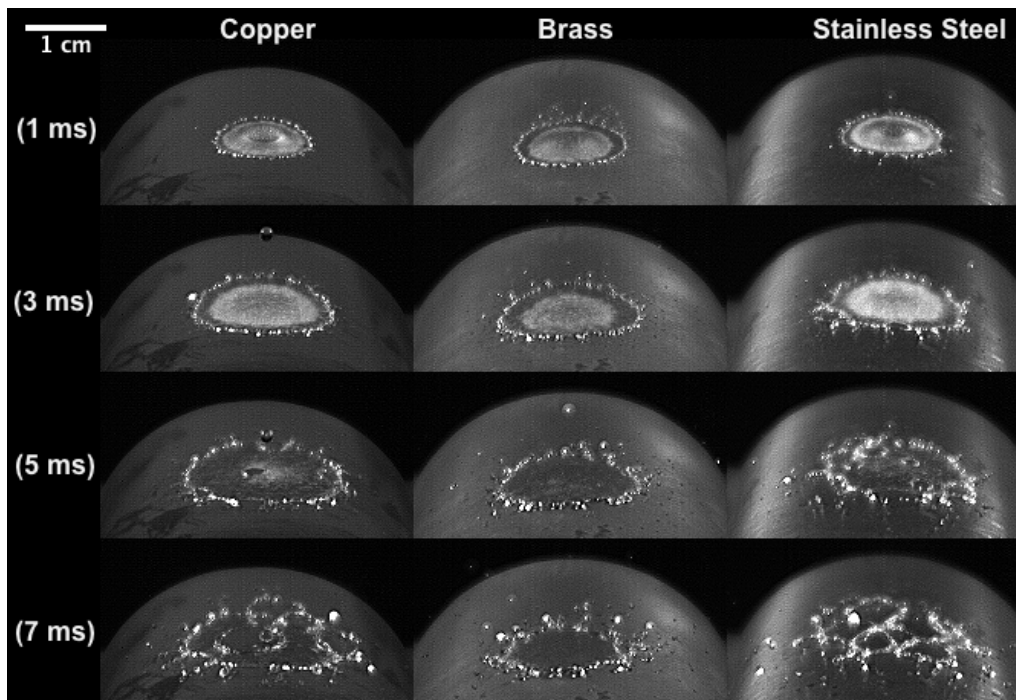


Figure 33 – Water droplet impacts on various heated surfaces at $T_s = 700^\circ\text{C}$

An alternate explanation may be that the impact velocity of the droplet and the development of vapour bubbles could provide enough inertial energy to break up the oxide scale or at least reduced its thickness. In this case, microscopy of the copper surface would reveal structural features of the oxide layer and help draw insight to this special case. Further recommendations will be left for Chapter 7.

The influence of thermal diffusivity on droplet morphology was difficult to determine at the highest surface temperature of $T_s = 700^\circ\text{C}$, shown in **Figure 33**, due to oxidation of all surfaces. The degree of surface oxidation was unknown with the heat transfer reaching the droplet varying with the surface material. However, it appeared that the formation of the vapour layer was fully developed after $t = 5$ ms for all surfaces, after which the droplet recoiled inward and then disintegrated. It is difficult to determine the influence of thermal diffusivity of secondary droplet characteristics from raw images presented in this section. The results of image processing and analyses on secondary droplet properties provided a clearer interpretation of the influence of thermal diffusivity and are presented in Section 5.4.

5.2.3 Effect of Surface Shape

Impact morphologies were primarily influenced in the spreading dynamics of the droplet when the surface shape was altered. The curvature of a surface allows an impacting droplet to spread over a greater area than a flat surface. The effect of gravity pulls the spreading droplet edges to contour it along the curved surface thereby thinning out the liquid. This allows greater dissipation of the initial droplet's kinetic energy.

The effect of surface curvature was especially noticeable from ambient conditions to a surface temperature of $T_s = 150^\circ\text{C}$. Observing **Figure 34** for an impact at $T_s = 150^\circ\text{C}$, surface tension forces allowed the droplet to recoil inward on itself on both surfaces. However, the curvature of the hemisphere caused secondary droplets to fall off the edges while majority of the initial droplet remained intact on the flat surface. The flat surface allowed the droplet to scuttle across it while maintaining heat transfer that flung small secondary droplets into the air until complete evaporation of the bulk droplet occurred 696 ms after impact. By comparison, the residence time of the droplet on the curved surface was only 45 ms.

From surface temperatures of $T_s = 200^\circ\text{C}$ (**Figure 35**) and beyond, droplet impact morphologies became visually similar. One difference was that the droplet had a 1-2 ms longer residence time on a flat surface than a curved surface at a given temperature above $T_s = 200^\circ\text{C}$.

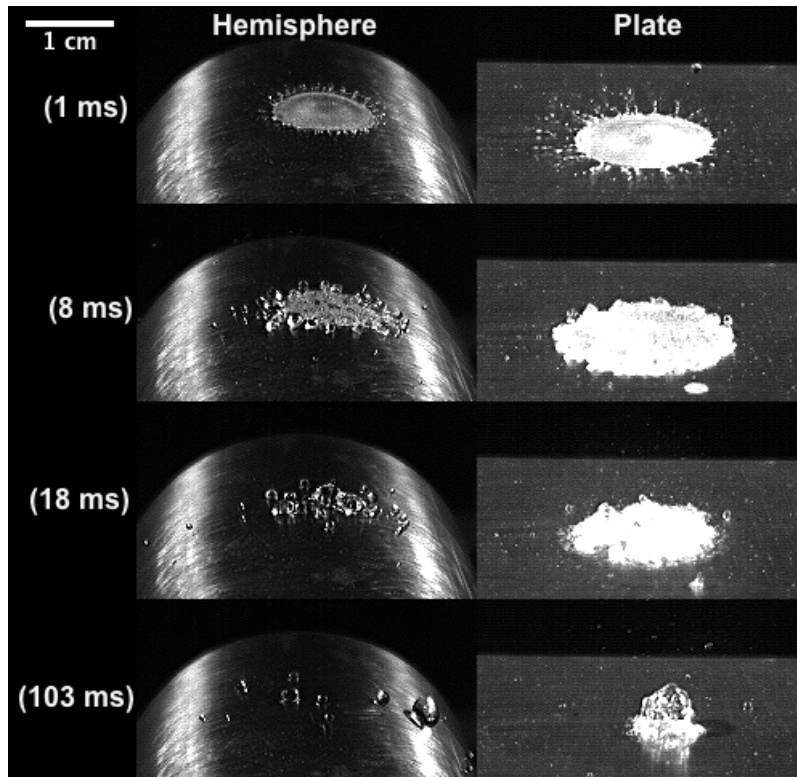


Figure 34 – Water droplet impacts on curved and flat brass surfaces at $T_s = 150^\circ\text{C}$

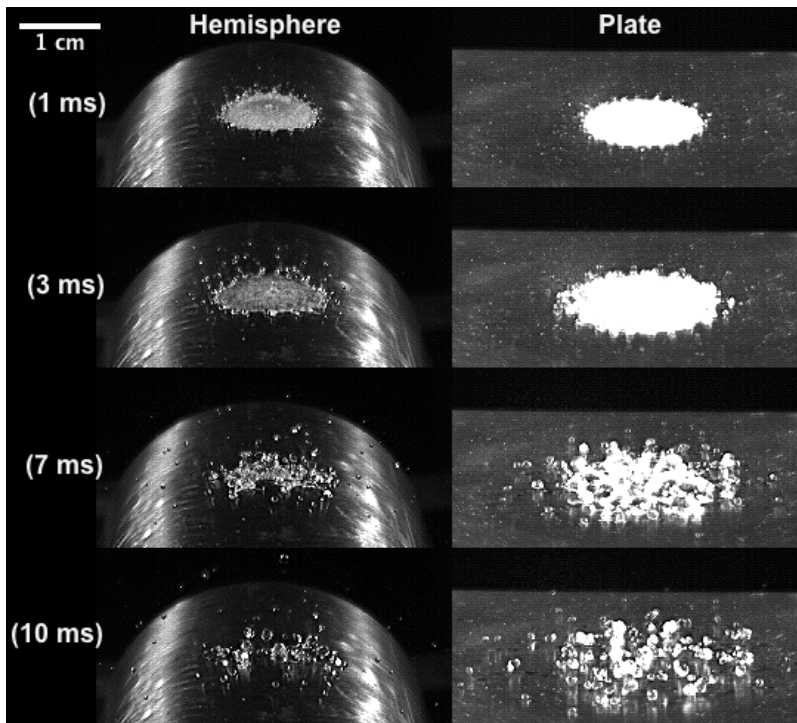


Figure 35 – Water droplet impacts on curved and flat brass surfaces at $T_s = 200^\circ\text{C}$

For droplet impacts that ejected secondary droplets, the curved surface allowed the secondary droplets to fall off easier than the flat surface. Variances in secondary droplet characteristics with surface shape will be further discussed in Section 5.4.

5.3 Explosive Boiling Force

A quantitative estimation of the force responsible for the explosive blow out of secondary droplets is given in this section.

An energy balance analysis on spray cooling heat transfer, developed by Liu, Morsi, & Van Der Walt (1998), was adopted in this study and used to estimate the explosive boiling force. The model is appropriate since it is a mass balance involving the change in liquid mass before and after the impact. A portion of the initial liquid mass is converted to vapour mass, which is the driving force for vapour explosions and can be calculated. The ejected secondary droplets account for the remaining liquid mass unconverted in to vapour. The process was assumed to occur at atmospheric pressure with the secondary droplets leaving the surface at 25°C. This was a reasonable assumption since water has a high heat capacity and the thermal gradient induced in the water droplet is localized to only the bottom layers of molecules closest to the hot surface. The liquid layers at the interface will undergo phase change and vapour superheating while the outer most liquid layers, furthest from the surface, would be unaffected (Yushen et al., 2001).

The total heat flow from the surface into the initial droplet is consumed in three ways; bringing the initial droplet temperature from 25°C up to saturation, evaporation of the droplet into vapour, and superheating the escaping vapour. An energy balance on the droplet with the three heat consumption terms yields Equation (9) (Jourhara & Axcell, 2009; Liu et al., 1998).

$$Q_T = Q_{sat} + Q_{evap} + Q_{sv} \quad (9)$$

Q_T is the total heat absorbed by the droplet during interaction with the hot surface and is equal to the heat flux, q'' , that was estimated by Equation (8).

Q_{sat} is the heat required to bring the droplet up to saturation and is given as Equation (10),

$$Q_{sat} = \dot{m}_L C_{p,liq} (T_{sat} - T_d) \quad (10)$$

where \dot{m}_L is the liquid mass flux, $C_{p,liq}$ is the liquid heat capacity, T_{sat} is the saturation temperature of water at atmospheric pressure and T_d is the initial

droplet temperature of 25°C. The liquid mass flux was taken to be the liquid mass flow rate in and out of a cross-sectional area defined by the spread area of the droplet on the surface and is estimated by Equation (11).

$$\dot{m}_L = \frac{1}{A} \frac{dm}{dt} = \frac{m_2 - m_1}{A_{avg} t^*} \quad (11)$$

Recalling that upon contact with the surface, a droplet will flatten into a circular disk that expands and contracts in diameter as its kinetic energy is dissipated. The spreading area is therefore changing with time. Because of this, the cross-sectional area is represented as an averaged spread area, A_{avg} , over the duration the droplet is in contact with the surface, t^* . ImageJ directly measured the diameter of the liquid disk in each frame from which spread area was calculated and averaged.

There is a difference in liquid mass as it interacts with the cross-sectional area where the initial droplet mass before impact is m_1 and after impact, the remaining liquid mass is m_2 . Specifically, m_2 is the total mass of secondary droplets evolved just after the moment where majority of the secondary droplets have left the region of the thermocouple. This entails secondary droplets that moved away from thermocouple region by radially spreading away or droplets that have ejected away from the specimen surface. The masses of the initial droplet and secondary droplets were calculated by using ImageJ. The apparent areas of each individual droplet were recorded in every frame from which a diameter was calculated. Assuming the droplet volume was a sphere with a constant density gave droplet mass.

Continuing with the heat consumption terms, Q_{evap} is the heat consumed for evaporation of the liquid at the liquid-solid interface, given by Equation (12),

$$Q_{evap} = \dot{m}_V h_{fg} \quad (12)$$

where \dot{m}_V is the vapour mass flux evolving at the interface and h_{fg} is the latent heat of vapourization.

Finally, the Q_{sv} is the heat absorbed by the vapour that is responsible in superheating it to the average vapour temperature before leaving the surface. It is given in Equation (13),

$$Q_{sv} = \dot{m}_V C_{p,vap} (T_{vap} - T_{sat}) \quad (13)$$

where \dot{m}_V is the vapour mass flux, $C_{p,vap}$ is the vapour heat capacity, evaluated at average vapour temperature and T_{vap} is the temperature of the superheated vapour.

Combining Equations (11) to (13) with $Q_T = q''$, yields Equation (14).

$$q'' = \dot{m}_L C_{p,liq} (T_{sat} - T_d) + \dot{m}_V h_{fg} + \dot{m}_V C_{p,vap} (T_{vap} - T_{sat}) \quad (14)$$

Since the driving force for explosive boiling is the creation of vapour at the droplet-surface interface, the equation above is rearranged to solve for the vapour mass flux.

$$\dot{m}_V = \frac{q'' - \dot{m}_L C_{p,liq} (T_{sat} - T_d)}{h_{fg} + C_{p,vap} (T_{vap} - T_{sat})} \quad (15)$$

From the vapour mass flux calculated by Equation (15), the total vapour mass created during a droplet impact event was determined by multiplying the vapour mass flux by the average liquid-solid interfacial area, A_{avg} , and the residence time, t^* . The explosive force generated in a droplet impact was related with a simple mass and acceleration relationship, shown in Equation (16),

$$F = m_{vap} a \quad (16)$$

where m_{vap} was the vapour mass and a was the average acceleration of the secondary droplets.

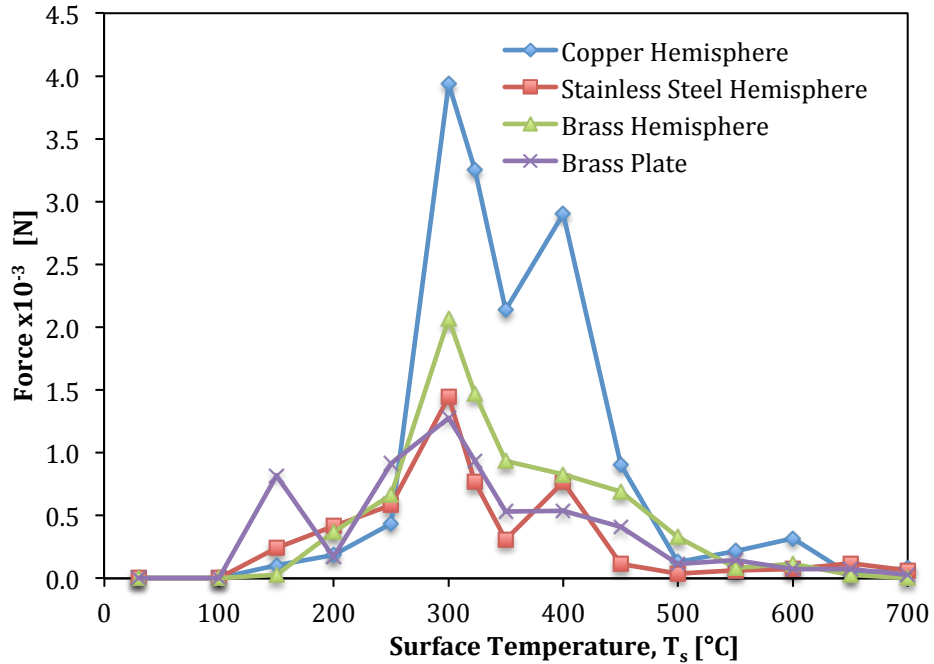


Figure 36 – Explosive boiling force of a water droplet at $T_d = 25^\circ\text{C}$ impacting surfaces of copper, brass, and stainless steel at various initial temperatures

The position of individual secondary droplets could be tracked in each frame and the acceleration of the droplets evolved from an explosive boiling event could be estimated. The results of boiling force estimations of all material types with respect to surface temperature are plotted in **Figure 36**.

5.3.1 Propagation of Uncertainties in Estimates

Experimental equipment uncertainties were previously reported as absolute errors in **Table 4** in Section 3.3 and were used to determine the relative errors propagated through mathematical estimation of the explosive boiling force and on secondary droplet properties.

The time dependence of the liquid and vapour mass flux contributed a minor source of error given that the sample rate for both temperature measurements and camera capture rate was 1000 samples/s, giving an absolute error of $\pm 5 \times 10^{-3}$ s. This was the limiting variable in terms of accurate estimation of droplet residence times.

The most significant source of error comes from the estimation of the mass of liquid after an impact, m_2 in Equation (11). m_2 is underestimated and is dependent on the lower limit of detectable droplet sizes in this study. Equipment and analysis limitations impose a lower limit of droplet sizes of 0.2 mm in diameter. The masses of droplets with sizes under this limit are excluded. The error associated with m_2 therefore propagates through the estimation of the liquid mass flux and eventually to the boiling force.

This error is evident when applying a mass conservation around the impact event of a droplet. The mass conservation states that the liquid mass before the impact is equal to the sum of the mass of liquid after impact plus the mass of vapour. However, the equality of the mass balance is not upheld due to the underestimation of the post-impact liquid mass and the dependence of the vapour mass on the heat balance calculated by Equation (14) and (15). As a result, the vapour mass is overestimated and the explosive boiling force was estimated to have an average relative error of about 30% and is represented in in **Figure 37**.

An additional consideration is that more intense explosive boiling events result in the creation of smaller droplets. This effectively pushes the distribution of secondary droplet sizes further outside the detectable range and further increases the boiling force error for those impacts. Detailed and extended uncertainty analysis for boiling force estimation provided in Appendix C.

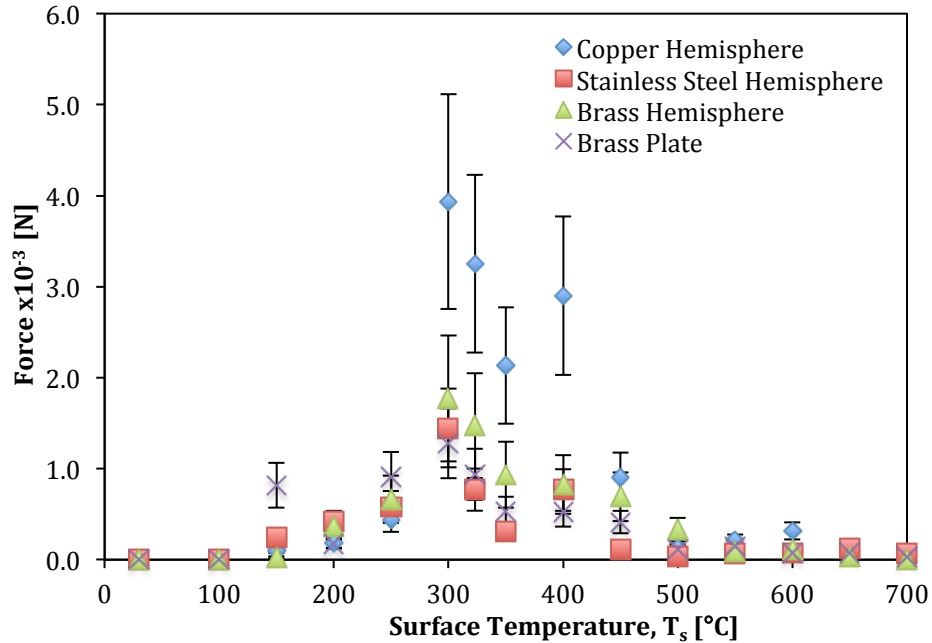


Figure 37 – Error bars for estimated explosive boiling force of a water droplet on various surfaces

5.3.2 Effect of Surface Temperature

The explosive force exerted on a droplet during impact is expected to scale with the heat flux and the boiling regime at the liquid-solid interface. The boiling force was zero up to the saturation point of water ($T_s \leq 100^\circ\text{C}$). Nucleate boiling does occur in a droplet on a 100°C surface, as seen in the raw images of **Figure 16**. However, vapour bubble production occurs quiescently and their collapse is too weak to disintegrate the droplet or eject secondary droplets. Above the saturation point, disintegration of the droplet produced secondary droplets and began at $T_s = 150^\circ\text{C}$ for all surfaces, seen in **Figure 27**. The force was still relatively small due to the dominance of inertial break up creating secondary droplets with minor contributions from thermal atomization.

Referring to **Figure 36**, the boiling force exerted to disintegrate the droplet gradually increased with the wall heat flux up to $T_s = 250^\circ\text{C}$ for hemisphere surfaces. The nucleation rate of vapour bubbles at the liquid-solid interface increased with wall superheat where the strength of collapsing vapour bubbles increased and penetrated the liquid layer disintegrating it more intensely. The disintegration into clouds of smaller bubbles is known to occur and is due to the development of Rayleigh – Taylor instabilities (Shepherd et al., 1982; Zhao et al.,

2000). This process describes one of thermal atomization where the vapour, created at the interface, is accelerated into the liquid. Visual analysis confirmed that finer secondary droplets were atomized with increasingly higher count, ejection velocities, and distributed area as surface temperature was increased towards the superheat limit for water. Thermal atomization in droplet break up could be distinguished by the increased amount of fine secondary droplets with ejection trajectories that were vertical to the surface. **Figure 38** depicts the image processed visualization of secondary droplet atomization.

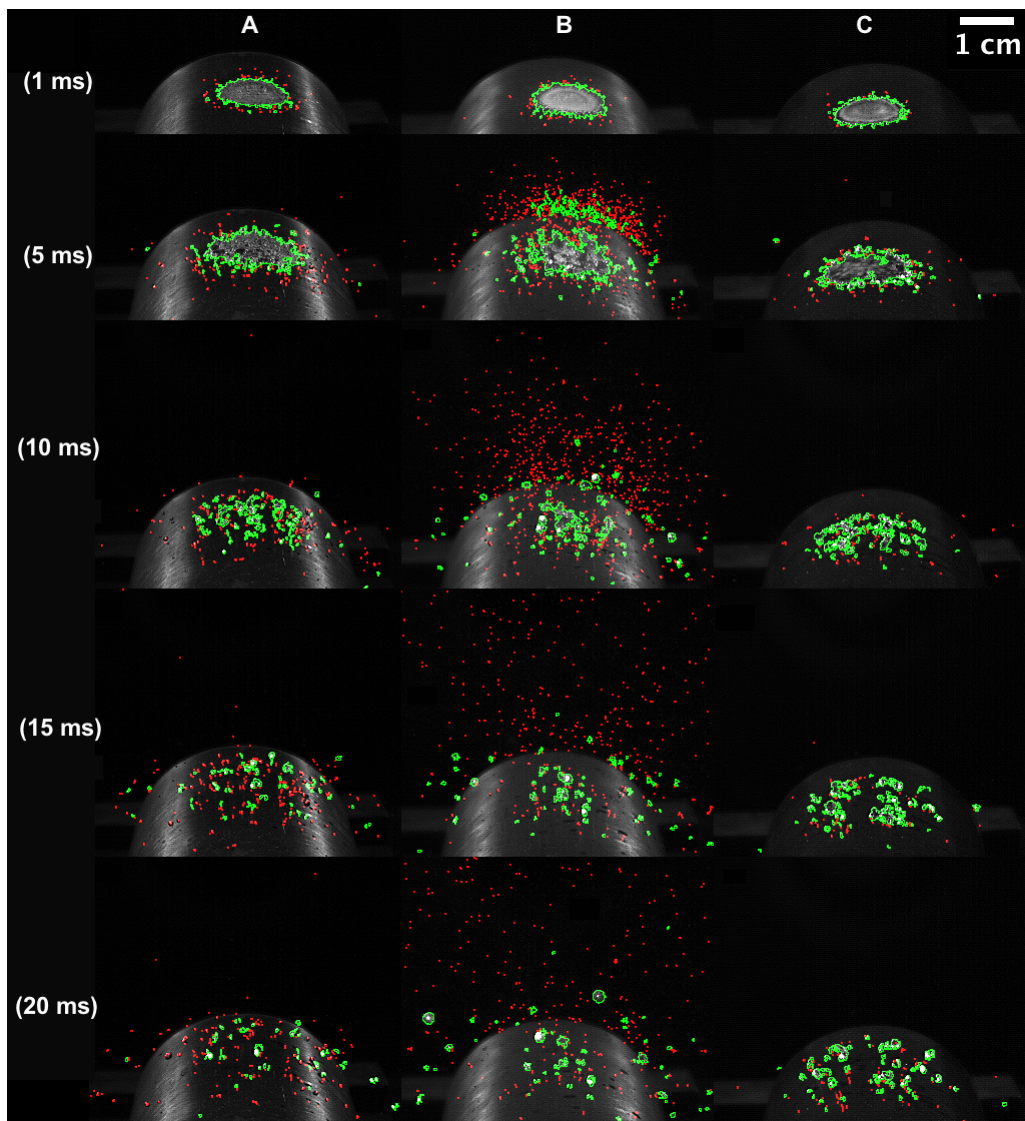


Figure 38 – Secondary droplet visualization on a copper surface at surface temperatures: column A – $T_s = 200^\circ\text{C}$; column B - $T_s = 300^\circ\text{C}$; column C - $T_s = 500^\circ\text{C}$

Fine droplets are shown in red with diameters 0.2-0.4 mm and large droplets are shown in green with diameters greater than 0.4 mm.

From **Figure 38** – column A ($T_s = 200^\circ\text{C}$), large secondary droplets evolved from the spreading and recoil break up of the droplet while fine secondary droplets evolved from splashing at earlier times and from thermal atomization, occurring later on in the impact. This suggests that both inertia and thermal effects are responsible for secondary droplet formation.

From **Figure 36**, the explosive boiling force reached a maximum near the superheat limit of water at around $T_s = 300^\circ\text{C}$ for hemisphere surfaces, except for the brass plate which occurred earlier at $T_s = 250^\circ\text{C}$. The raw image sequence of **Figure 29** depicts the thermal detonation of the droplet on the three different hemisphere surfaces and was the most severe near the superheat limit. From morphological and image processing analyses, defining characteristics of the most intense explosive boiling event occurring at the superheat limit were determined to be: 1) the spreading diameter of the droplet on the surface was at a minimum; 2) no recoil of the spreading droplet on the surface; 3) droplet residence time on the surface was at a minimum; 4) droplet disintegration occurring in the quickest time after impact; 5) secondary droplet counts, velocity and distribution area were the largest; 6) upward projection of fine secondary droplets. **Figure 38** – column B ($T_s = 300^\circ\text{C}$), shows the development of a large number of fine secondary droplets at earlier times after impact compared to the previous temperature cases.

At the superheat limit, fine secondary droplets were ejected the most vertically and distributed over the largest area while larger secondary droplets ejected radially outwards with less velocity due to their larger mass. This is expected given that the maximum heat flux occurs in the region of the superheat limit and yields an intense and violent boiling mode, of which explosive boiling is also at maximum. Studies by Yushen et al. (2001) and Lee & Merte (1996) showed the acceleration of the liquid layers closest to the hot surface significantly increases once a superheat limit temperature was reached. Their findings agree with the results of morphological analyses and large estimated boiling force at the superheat limit temperature in this study.

The decline in explosive boiling force above the superheat limit temperature was due to the increasing presence of a vapour layer that acts to separate the liquid layer from the hot surface. Regions of vapour coalesce more readily as the surface temperature was increased in the transition boiling regime. Bubble collapse will not penetrate the liquid when a region of vapour impedes it (Moreira et al., 2007). Thermal denotation was therefore reduced to regions where the liquid only contacts the surface. As a result, the explosive boiling force was observed to decrease in **Figure 36** once the surface temperature exceeded the superheat limit

($T_s > 300^\circ\text{C}$). From morphological analyses, it was shown that thermal atomization and thermally induced break up of the initial droplet occurred but was delayed in time with reduced secondary droplet production and distributed area compared to an impact at the superheat limit.

Oxide layer formation was observed to occur in **Figure 30** at $T_s = 400^\circ\text{C}$ for all surfaces and resulted in peaks of explosive boiling force for copper and stainless steel surfaces in **Figure 36**. Surface oxidization returned the droplet impact to conditions favourable to explosive boiling. Since heat transfer is impeded through the oxide layer, the outer surface, or the interface that the droplet encounters is at a lower temperature – one that is close to the superheat limit temperature. As the surface temperature increased past $T_s = 400^\circ\text{C}$, the heat flux through the oxide layer was sufficient to support film boiling and was responsible for the decline in explosive boiling force. This can be observed in **Figure 38** – column C ($T_s = 500^\circ\text{C}$) where film boiling of the droplet was established and very few fine secondary droplets were formed in favour of larger ones.

5.3.3 Effect of Thermal Diffusivity

From **Figure 36**, the effect of thermal diffusivity on explosive boiling force was pronounced in the surface temperature region from $T_s = 300^\circ\text{C}$ to $T_s = 450^\circ\text{C}$. Plotting this temperature region with respect to thermal diffusivity yields **Figure 39**. For surface temperatures outside of the temperature range of $300^\circ\text{C} \leq T_s \leq 450^\circ\text{C}$, **Figure 40** is presented. Surface temperatures for ambient conditions and 100°C are not shown since their boiling force was effectively zero.

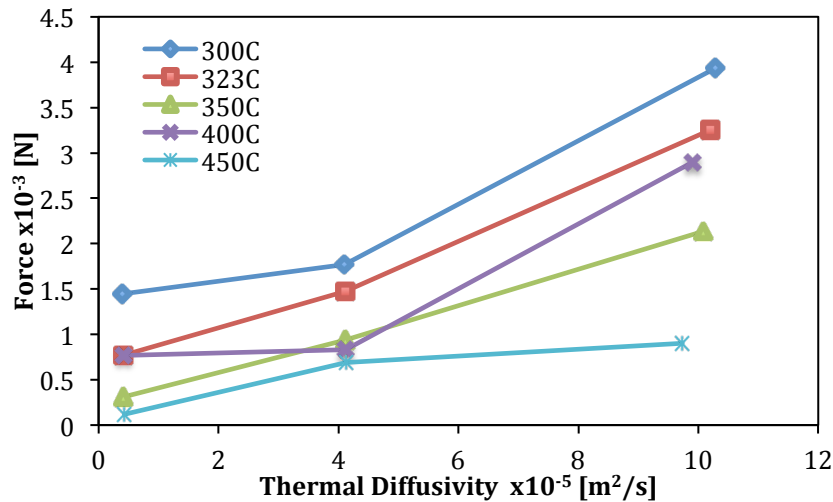


Figure 39 – Explosive boiling force as a function of thermal diffusivity for the most energetic boiling surface temperatures

By comparing the two figures, it can be immediately seen that explosive boiling force increases with increasing thermal diffusivity with a positive correlation in the region of $300^{\circ}\text{C} \leq T_s \leq 450^{\circ}\text{C}$. This is because a higher thermal diffusivity results in quicker deposition of heat into the droplet. It was shown in raw images and from Section 5.2.2, that this temperature region had the most intense explosive boiling events. Since the catastrophic disintegration of a droplet that undergoes explosive boiling is solely from thermal break up, the intensity of explosion is sensitive to surface thermal diffusivity.

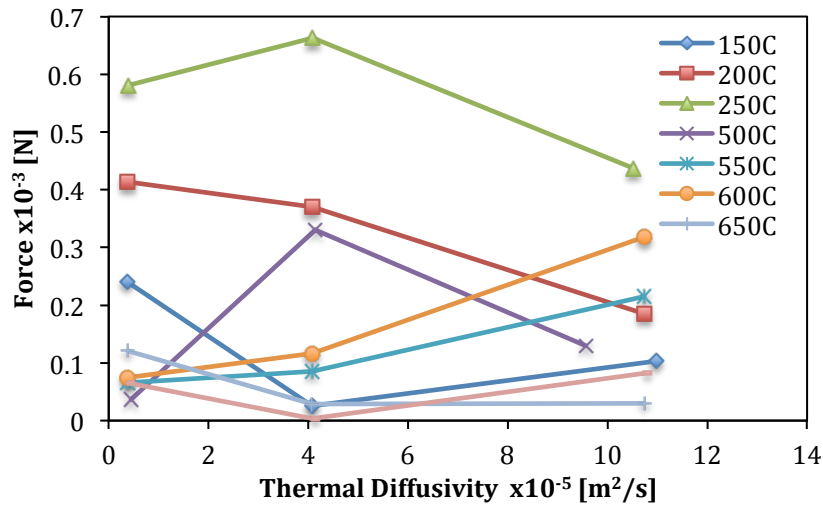


Figure 40 – Explosive boiling force as a function of thermal diffusivity for the surface temperatures with decreased boiling intensity

Elsewhere for other surface temperatures, shown in **Figure 40**, inertial break up is greater than thermal break up, hence thermal diffusivity variations are neither insignificant on boiling force nor on droplet disintegration mechanisms. In other words, thermal diffusivity only affected the thermal break up mechanism that is only encountered in the region of the superheat limit.

Applying linear trend lines to both sets of data for each temperature in **Figure 39** and **Figure 40** revealed that the magnitude of the slope was an indication of the degree to which thermal break up contributed to droplet break up over inertial break up. A larger and more positive slope indicated that thermal break up was more sensitive to increases in thermal diffusivity. Linear trend lines had very poor agreement with the surface temperatures in **Figure 40** where near zero or negative slopes meant that thermal break up was minimal because inertial break up dominated.

The best agreements to the linear trend lines were for the temperature region of $300^{\circ}\text{C} \leq T_s \leq 450^{\circ}\text{C}$. A linear regression was performed for this region giving a $y = 26.7x$ trendline fit shown in red in **Figure 41** with $R^2 = 0.832$ and $p < .001$. This shows that the explosive boiling force has a positive linear sensitivity to increasing thermal diffusivity.

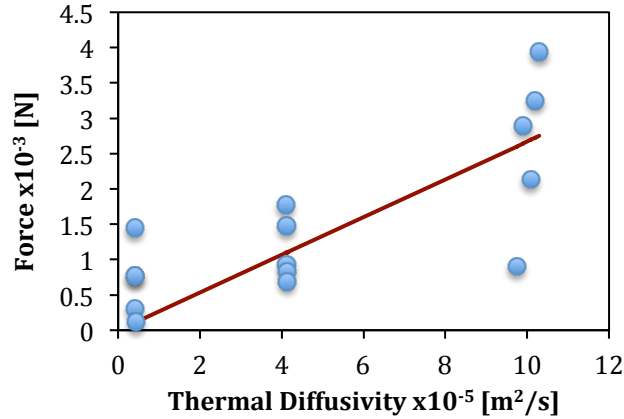


Figure 41 – Linear regression line fit plot

The effect of thermal diffusivity on the intensity of explosive boiling can be seen in **Figure 42** for a surface at $T_s = 300^{\circ}\text{C}$. The thermal diffusivities of the three surfaces rank as follows: $\alpha_{\text{Copper}} > \alpha_{\text{Brass}} > \alpha_{\text{Stainless Steel}}$. In a similar manner that the thermal diffusivities rank, so too does the intensity of the explosion in **Figure 42**. Copper with the highest thermal diffusivity showed greater break up of the droplet with greater number of fine secondary droplets and distribution over the brass surface, which was greater than the lowest thermal diffusivity surface of stainless steel. Copper induces a faster rate of heat transfer to a droplet on the surface in a given instant of time. The rate and the amount of vapour produced was the largest for copper and expanded against the liquid layers and collapses violently, atomizing the droplet into small secondary droplets the quickest. The rapidity of heat transfer to the droplet can be seen and is most pronounced when comparing the frame-by-frame development of droplet disintegration for copper to stainless steel in **Figure 42**.

Copper (highest thermal diffusivity material) had the largest maximum explosive blowout force that was 4 times as large as stainless steel (lowest thermal diffusivity material) at $T_s = 300^{\circ}\text{C}$. An F-test for variances showed that explosive boiling force was significantly larger for copper than stainless steel with an F ratio of 11.28, $p < .001$. Similarly, the copper surface showed significance in the explosive boiling force over the brass hemisphere with an F ratio of 5.35, $p =$

.002. F-test analysis also showed that brass hemisphere did not show a statistical significant effect on explosive boiling force compared to the stainless steel surface with an F ratio of 2.11, $p = .088$. However, given the clear differences in the image sequence between the two surfaces, the p value is small enough to say a thermal diffusivity is relevant for brass and stainless steel.

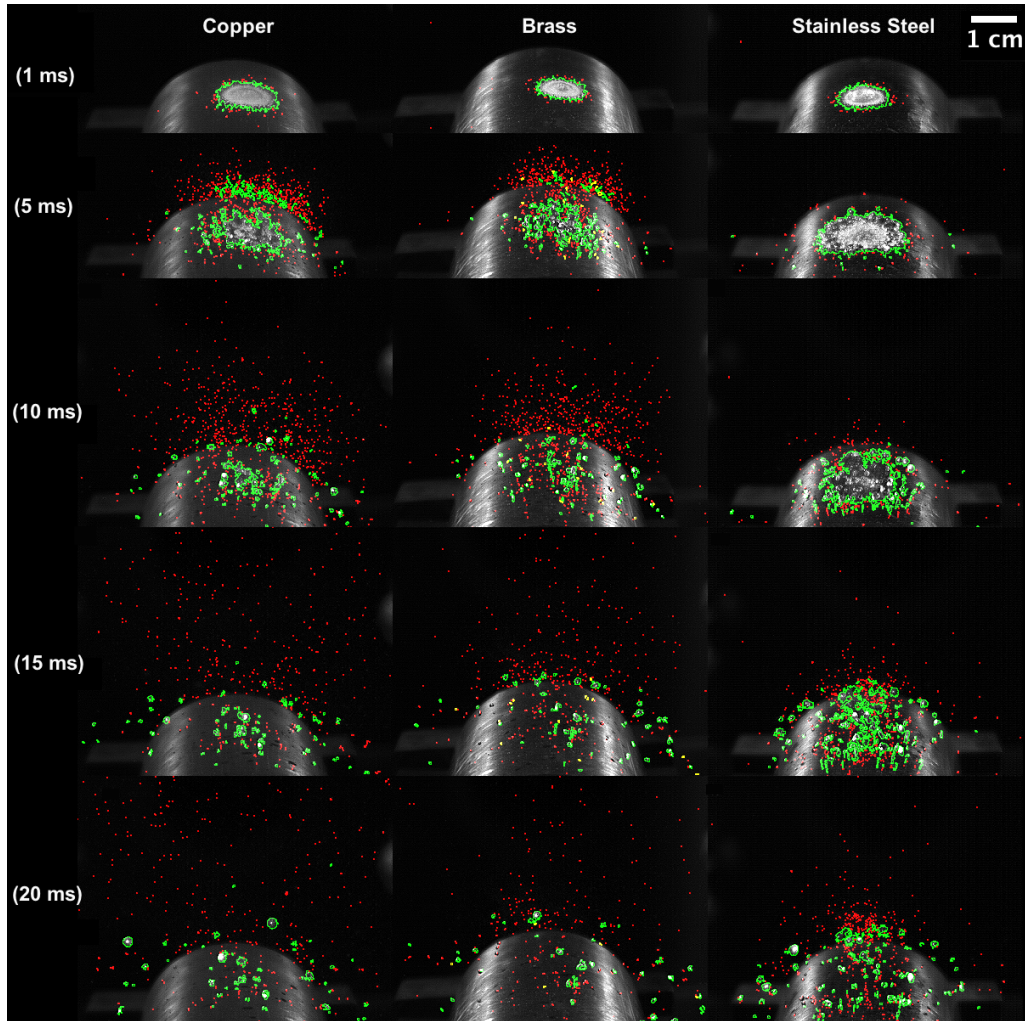


Figure 42 – Image processed sequences of droplet explosion on various heated surfaces at $T_s = 300^\circ\text{C}$ with varying thermal diffusivity

The explosive boiling force was insensitive to variances in thermal diffusivity below a surface temperature of 250°C and greater than 450°C . This was due to the mechanism of droplet disintegration being interially dominated while thermal atomization was suppressed.

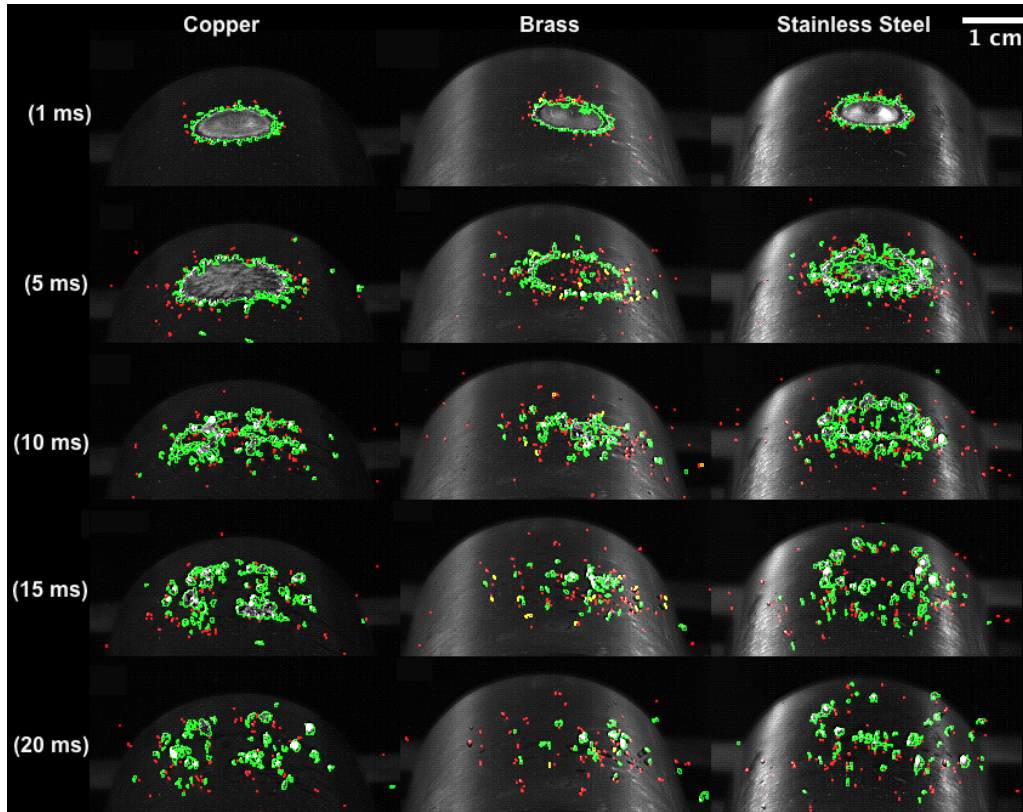


Figure 43 – Image processed sequences of droplet explosion on various heated surfaces at $T_s = 500^\circ\text{C}$ with varying thermal diffusivity

Up to a surface temperature of $T_s = 250^\circ\text{C}$, though thermal atomization is present, it is overshadowed by the dominance of inertial break up. Above $T_s = 450^\circ\text{C}$, thermal atomization is drastically suppressed where thermal diffusivity only affects the formation rate of the vapour cushion (Cossali et al., 2006). This can be seen in **Figure 43** for surfaces in the film boiling regime. Larger secondary droplets are produced with flatter trajectories as a result of inertial dominated droplet break up.

5.3.4 Effect of Surface Shape

From **Figure 36**, an early effect of surface shape on explosive boiling can be seen at $T_s = 150^\circ\text{C}$, where the boiling force was larger on the flat plate compared to the curved hemisphere. Droplet morphology showed that the secondary droplets fell off the surface in the curved surface case. However, for the flat surface, the droplet maintained its initial form after impact and resided on the surface while absorbing heat. Boiling force is therefore larger for the droplet on the flat surface since the

effect of nucleate boiling is fully realized as the droplet is permitted to stay on the hot surface. From $T_s = 300^\circ\text{C}$ to $T_s = 500^\circ\text{C}$, explosive boiling force was consistently higher on the curved surface. This was because the curved surface allows the droplet to spread out to a larger diameter thereby thinning out the liquid layer through which a greater surface area improved heat transfer. The curved surface promotes the droplet to spread to its maximum diameter quicker than on a flat surface since gravity contours the droplet edges. Once film boiling is realized ($T_s \geq 500^\circ\text{C}$), explosive boiling was very insensitive to surface shape.

It should be noted that F-test analysis showed that surface shape did not show statistical significance at the 5% significance level with the F ratio at 1.90, $p = .12$. The F-test result should be considered with the fact that the explosive boiling force was essentially the same for both surface types at surface temperatures below $T_s = 300^\circ\text{C}$ and above $T_s = 500^\circ\text{C}$. As a result, surface shape is considered to have little effect varying the explosive boiling force.

5.4 Explosive Boiling On Secondary Droplet Characteristics

Image processing allowed evaluation of secondary droplet counts, size and distribution with respect to surface temperature and surface material. The following sections discuss the relationship between secondary droplet properties and the degree of explosive boiling.

The full distribution of droplet sizes is not represented due to experimental equipment limitations where droplets 0.2 mm in diameter and greater are detectable. The results presented below are considered with this restriction in mind. Comparisons of secondary droplet count and size with thermal diffusivity were the most influenced by the detection limit, showing low statistical significance. Clear trends were observed in the properties with respect to surface temperature since comparisons are supported by the explosive boiling force curve.

5.4.1 Secondary Droplet Count

Effect of Surface Temperature

From the onset of nucleate boiling at $T_s = 100^\circ\text{C}$, increases in surface temperature created more vapour bubbles from heterogeneous nucleate boiling. The growth and collapse of the bubbles in the remaining liquid from the initial droplet is responsible for the thermally induced atomization of secondary droplets. As superheat is increased in the nucleate boiling regime, the maximum secondary

droplet count increased towards the superheat limit of water, around $T_s = 300^\circ\text{C}$, as depicted in **Figure 44**.

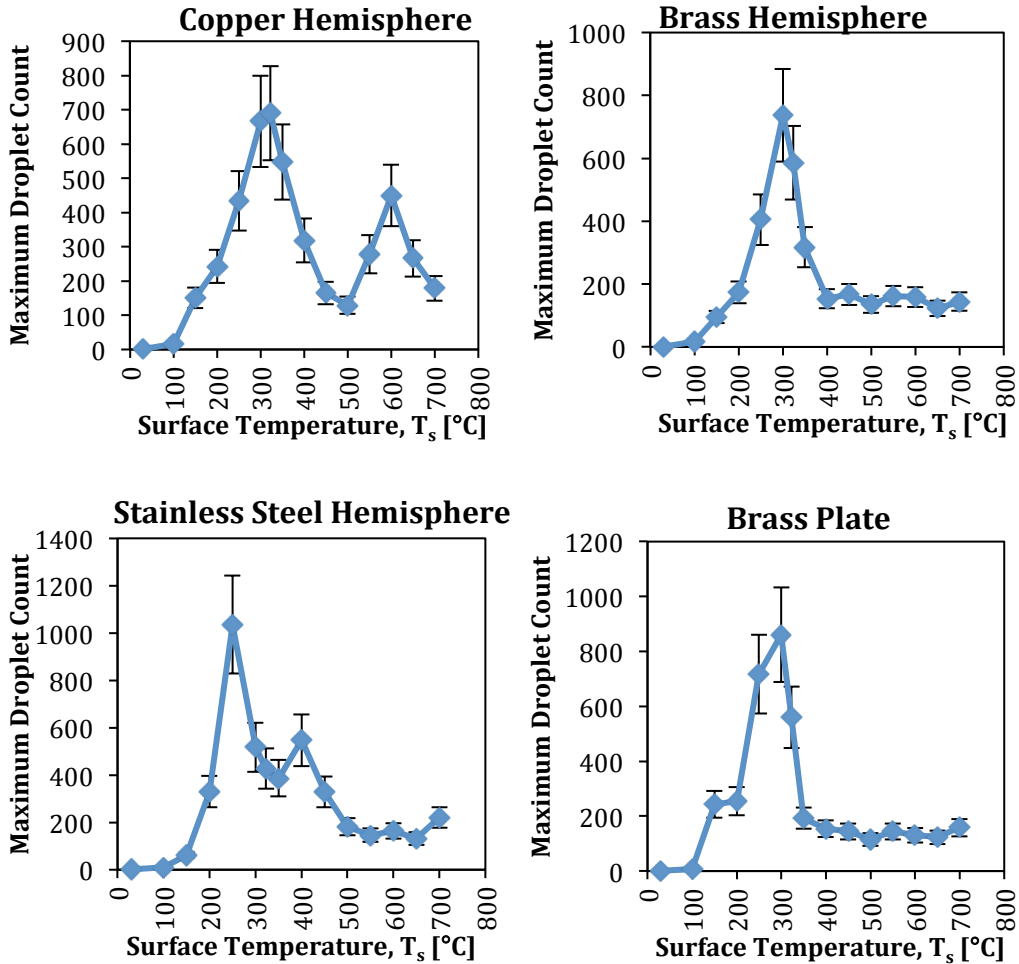


Figure 44 – Maximum secondary droplet counts for various surfaces

In general, when the explosive boiling force was at a maximum, the evolution of vapour fragmented the liquid most intensely. As a result, fine secondary droplets were produced in greater number and increased the total secondary droplet count to a maximum value. A peak in the secondary droplet count occurred at $T_s = 300^\circ\text{C}$ for copper and brass hemispheres and was consistent with the highest explosive boiling force estimated at that surface temperature. However, the maximum boiling force and the maximum droplet count did not coincide at the same surface temperature for the stainless steel hemisphere and the brass plate. For stainless steel, the maximum boiling force occurred at $T_s = 300^\circ\text{C}$ with the

peak secondary droplet count occurring at $T_s = 250^\circ\text{C}$. For the brass plate, the maximum boiling force occurred at $T_s = 250^\circ\text{C}$ with the peak secondary droplet count occurring at $T_s = 300^\circ\text{C}$. These discrepancies can be attributed to the camera setup and the error in the detectable range of the droplet sizes. For the stainless steel surface at $T_s = 300^\circ\text{C}$, the image area appeared slightly out of focus at the point of droplet contact with the surface. The brass plate surface at $T_s = 300^\circ\text{C}$ was increased in the camera shutter speed in an attempt to correct for the background noise. Because of this, the detectable range of secondary droplets was reduced resulting in counts that were lower than expected.

Droplet counts dropped once transition and film boiling was present. A vapour layer isolates the liquid from vapour bubble collapse and thus atomization of fine secondary droplets is reduced. A second peak in the droplet count was observed for copper and stainless steel at $T_s = 600^\circ\text{C}$ and $T_s = 400^\circ\text{C}$ respectively and was due to jump in the explosive boiling force occurring from oxide layer formation, as mentioned earlier.

Effect of Thermal Diffusivity

The effect of varying thermal diffusivity on droplet counts was difficult to distinguish when the counts were plotted against each other in **Figure 45**. An analysis of variance showed that thermal diffusivity did not have a statistical significance at the 5% significance level on explosive boiling with an F ratio of 0.54, $p = .59$. A study by Cossali et al. (2006) proposed that secondary droplet counts increased with thermal diffusivity at a given initial surface temperature. This was because at a given instant in time, a greater amount liquid from the initial droplet will vapourize on the high thermal diffusivity surface. Within nucleate boiling regime, this means greater vapour bubble production whose collapse ejects a greater number of secondary droplets. In this present study, a greater vapour mass flux was reported for a higher diffusivity surface than a lower one at a given surface temperature. However, this did not translate into higher secondary droplet counts. It should be noted that Cossali et al. (2006) only provided a visual count of secondary droplets and not through software aided analyses of secondary droplets like this present study.

The difference in results again comes from the detectable sizes of secondary droplets by the setup used in this study. Studies by Cossali et al. (2002), Richter et al. (2005) and Moreira et al. (2007) have reported secondary droplet sizes as small as $20\ \mu\text{m}$, a magnitude lower than the secondary droplet sizes reported in this study. As a result, secondary droplet counts can be quite different with minor changes in thermal diffusivity in the superheat limit region. The recommendations section will discuss the methods for more accurate secondary droplet analyses.

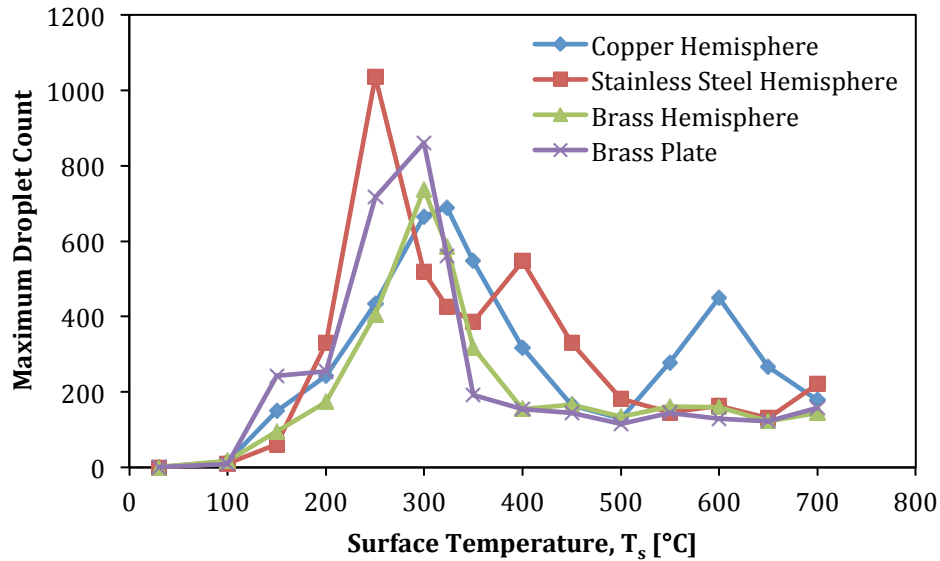


Figure 45 – Comparison of secondary droplet counts between various surfaces

Effect of Surface Shape

The creation of a greater number of droplets at $T_s = 150^\circ\text{C}$ in **Figure 45** on the flat surface to the curved surface is confirmed by morphological analysis. The initial droplet is permitted to reside on the flat surface rather than fall off on the curved surface. The droplet absorbs a greater amount of superheat and flings off a larger amount of secondary droplets compared to a droplet impact on the curved surface. The differences in counts seen at $T_s = 250^\circ\text{C}$ and $T_s = 300^\circ\text{C}$ in **Figure 45** were attributed to the larger mass of the initial droplet on the flat surface cases. Otherwise, from $T_s = 300^\circ\text{C}$ and on, surface shape did not effect secondary droplet counts. An f-test confirms this with an F ratio of 1.53, $p = .22$.

5.4.2 Secondary Droplet Size

Effect of Surface Temperature

Secondary droplet diameters were estimated from the apparent areas of the droplets from image processing analyses. Secondary droplet diameters were averaged for the course of an impact with a surface at a given surface temperature and plotted in **Figure 46** with error bars reported in **Figure 47**. The horizontal dotted line in **Figure 46** represents the size limit of detectable droplets by the experimental equipment.

In general, a decrease in the secondary droplet diameters was observed as the wall superheat increased towards the superheat limit. This was due to an increasing influence of thermal atomization creating a greater number of smaller secondary droplets resulting from vapour bubble collapse. This is in agreement with the morphological analysis reported earlier.

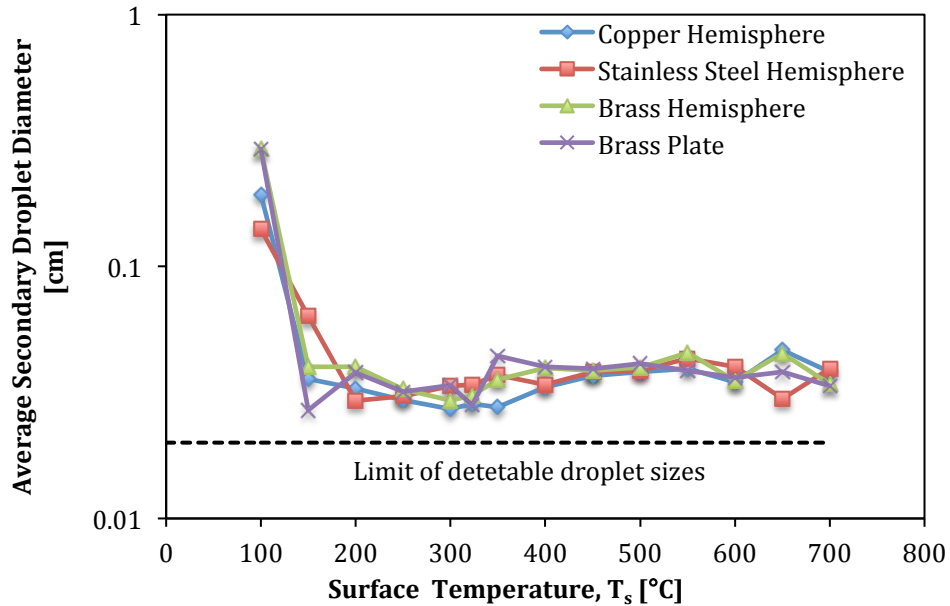


Figure 46 – Average secondary droplet diameters as a function of surface temperature for various surfaces

The secondary droplet diameters reached a minimum at $T_s = 300^\circ\text{C}$, with the exception of the stainless steel surface. This is expected given that the explosive boiling force was the greatest and contributes to the most violent fragmentation of the liquid, producing large quantities of fine secondary droplets of diameters 0.2 mm or less. As the surface temperature extends beyond the superheat limit, secondary droplet diameters increased.

The presence of a vapour layer resulting from transition or film boiling suppresses thermal atomization of fine secondary droplets. Instead, secondary droplet production occurred from the break up caused by the spreading and inward recoiling of the initial droplet as it transversed the dry, non-wetted regions of vapour on the surface. Larger secondary droplets are evolved from the coalescence and break up of the inward collapsing liquid.

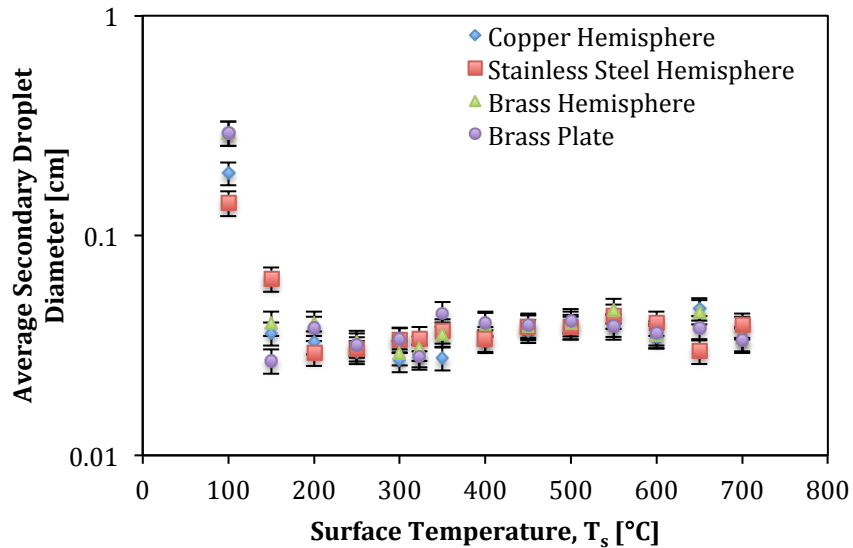


Figure 47 – Error bars for average secondary droplet diameters for various surfaces

Effect of Thermal Diffusivity

From **Figure 46**, thermal diffusivity of a surface does not vary the secondary droplet diameters significantly over the range of surface temperatures tested. An analysis of variance confirmed this, showing no statistical significance with an F ratio of 0.20, $p = .82$. This result was also reported in a study by Cossali et al. (2006) who investigated secondary droplet sizes by varying thermal diffusivity of an impact surface. However, their study did not test droplet impacts occurring near the superheat limit region. From previous discussions in this present study, the superheat limit region featured large variations in explosive boiling force with respect to variances in thermal diffusivity. Thus, a discussion about this region of superheat is necessary and relevant.

Expanding the superheat limit region of **Figure 46**, yields **Figure 48** and shows a clearer significance of thermal diffusivity differences on secondary droplet diameters in the range of surface temperatures from $T_s = 300$ - 350°C . Average secondary droplet sizes are smaller on the higher diffusivity material at a given surface temperature. Copper yielded the smallest secondary droplets, followed by brass then stainless steel in a similar manner that their thermal diffusivities rank. This result is expected given that the explosive boiling force scaled with thermal diffusivity in the same temperature region as **Figure 48**. Below a surface temperature of $T_s = 300^\circ\text{C}$ and above $T_s = 350^\circ\text{C}$, the average secondary droplet diameter is rather insensitive to thermal diffusivity.

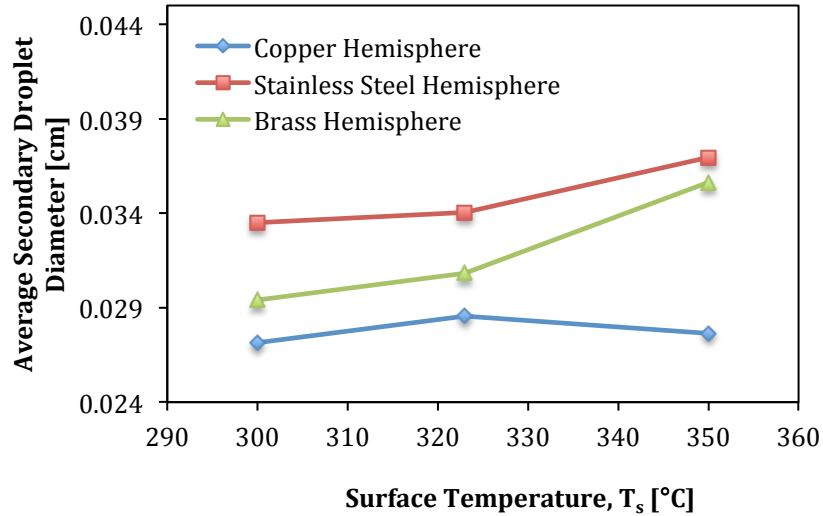


Figure 48 – Average secondary droplet diameters in the superheat limit region for various hemisphere surfaces

Effect of Surface Shape

From **Figure 46**, the effect of surface shape did not have a significant influence on secondary droplet diameter. Using an *f*-test, no statistical significance was reported at the 5% significance level with an *F* ratio of 1.0, $p = .49$. The only confirmed difference between droplet sizes occurred at $T_s = 150^\circ\text{C}$ with smaller droplets being produced on the flat surface compared to the curved surface as seen in the raw images sequence of **Figure 34**.

5.4.3 Secondary Droplet Distribution

Effect of Surface Temperature

The spatial distribution of ejected secondary droplets was measured on an *x-y* coordinate scale in image processing. The vertical and horizontal components of a traveling secondary droplet were separated and analyzed individually. The vertical component (*y*-direction) describes the upward trajectory of a droplet away from the surface and is reported in **Figure 49**. It is measured as the average height the secondary droplets attained above the impact surface. In terms of the horizontal component, the initial droplet impacts the surface at the middle of the *x*-coordinate scale in a given image. The horizontal distribution of ejected secondary droplets was measured in relation to the median and is shown in **Figure 50**.

Trends in secondary droplet trajectories can be identified by first referring to **Figure 38**, **Figure 42** and **Figure 43**, and realizing that secondary droplet size influences its ejection velocity and thus its spatial position. Small secondary droplets distribute over larger areas since thermal atomization creates smaller mass droplets with high escape velocities.

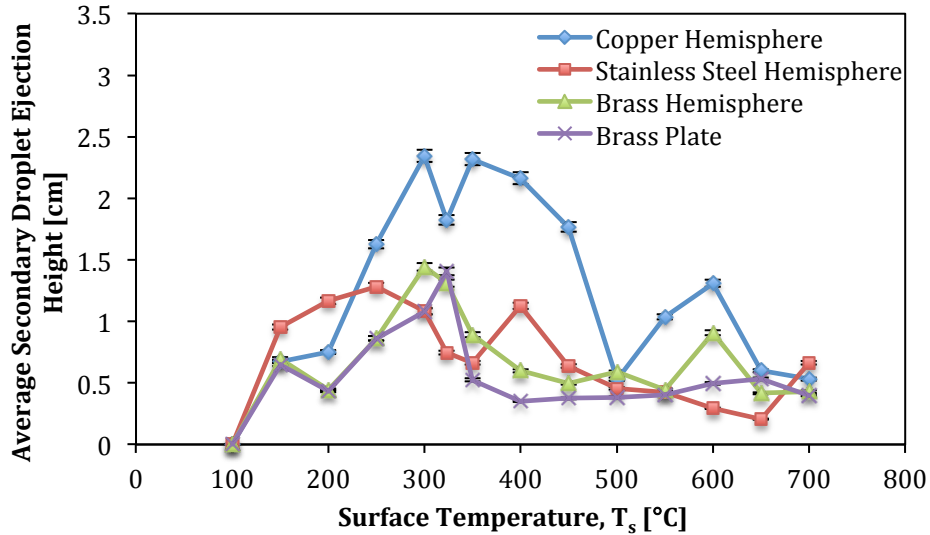


Figure 49 – Average vertical secondary droplet ejection height as a function of surface temperature for various surfaces

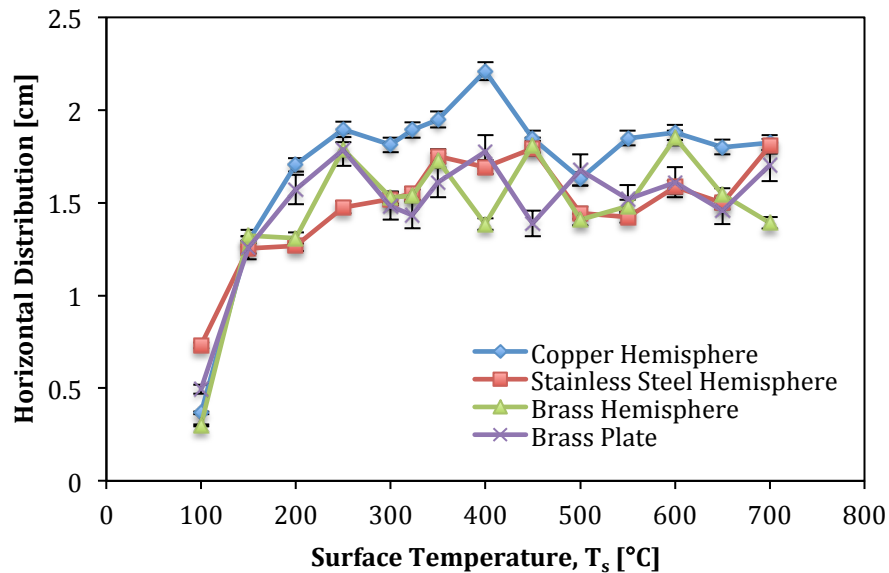


Figure 50 – Average horizontal distribution of secondary droplets ejected from various surfaces with surface temperature

The defining characteristic of thermal atomization was that secondary droplet counts increase and have greater vertical trajectories. As a result, the average height of the ejected secondary droplets is observed to increase in **Figure 49** and the horizontal distribution is larger in **Figure 50** up to the superheat limit.

The maximum vertical height the secondary droplets attained was at the superheat limit and is expected due to the explosive boiling force being at a maximum. The horizontal distribution of droplets at the superheat limit does not peak. This is because explosive boiling creates a large amount of small secondary droplets whose average trajectory occurs normal to the surface. Explosive boiling is less influential on the creation of large droplets since they are evolved primarily from inertial effects related to droplet spreading and recoiling. Large secondary droplets from inertial break up eject radially outwards with trajectories flatter to the impact surface. Inertial effects are predominant in droplet break up at surface temperatures above and below the superheat limit region.

Once transition and film boiling occurs, small secondary droplets are produced less because of decreased thermal atomization, with preference given to large secondary droplets instead. As a result, the vertical ejection heights decrease. In terms of the horizontal distribution, it increases slightly above the superheat limit temperature from $T_s = 300^\circ\text{C}$ to $T_s = 350^\circ\text{C}$ in **Figure 50**. This is because secondary droplet counts are reduced and those droplets that are produced generally have larger diameters. Those droplets eject radially with trajectories that were flat and are conducive to a greater horizontal spreading. Above $T_s = 350^\circ\text{C}$, the horizontal distributions trends are difficult to determine with respect to surface temperature. For copper and stainless steel, a clear decrease in horizontal distribution exists until $T_s = 500^\circ\text{C}$, after which it increases slightly with surface temperature. However, the horizontal distribution varies wildly for the brass surfaces above $T_s = 350^\circ\text{C}$. The small rise in vertical height and horizontal distribution at $T_s = 600^\circ\text{C}$ for the surfaces at which it occurs is attributed to the explosive boiling force which also increased.

Effect of Thermal Diffusivity

The effect of thermal diffusivity is once again realized in the region that spans $T_s = 250\text{-}400^\circ\text{C}$ for the vertical ejection heights and $T_s = 250\text{-}400^\circ\text{C}$ for the horizontal distributions. The difference in vertical and horizontal ejections is especially noticeable between copper and stainless steel since the largest thermal diffusivity difference exists between the two. An f-test showed strong significance in 5% significance region (F ratio of 3.79, $p = .01$) that the copper surface featured greater trajectories than stainless steel. However, the brass surface trend lines were located at irregular positions given the expectation that they would lie between the copper and stainless steel ones. An analysis of variance showed that

brass and stainless steel surfaces did not show statistically significant effect on droplet trajectories.

Effect of Surface Shape

The effect of surface shape between the curved and flat brass surfaces was shown to be statistically unvaried on secondary droplet trajectories. An f-test for the y-direction and x-direction trajectories featured an F ratio of 1.19, $p = .38$ and F ratio of 1.40, $p = .28$ respectively.

Chapter 6: Conclusions

Given the potentially destructive nature of explosive boiling during nuclear reactor accidents, this present study investigated the explosive boiling force of a single water droplet impacting hot solid surfaces of copper, brass and stainless steel over a range of temperatures spanning ambient conditions to film boiling temperatures. Droplet impacts were visualized using a high-speed camera and image processing techniques to investigate impact morphology and secondary droplet characteristics. Boiling force estimation was made by; using a transient one dimensional heat transfer model, estimating mass flux changes of liquid and vapour from pre-impact and post-impact droplet counts and sizes, and tracking secondary droplet acceleration.

Morphological observations showed that secondary droplets are produced after a droplet impacts a surface and disintegrates by a combination or exclusively by two mechanisms; inertial or thermally induced break up. Inertial break up was observed in impact outcomes where splashing occurred or when the droplet spread radially outward and then recoiled inward on itself. Thermal break up was observed in impact outcomes where boiling effects of vapour bubble production and collapse occurred. Thermal induced break up was increasingly prominent as surface temperature was raised past the onset of nucleate boiling. Conversely, inertial effects were reduced as seen by the decrease in maximum spread diameter and residence time of a droplet on a surface. Increasing influence of thermal break up lead to the explosive boiling force increasing with wall superheat in the nucleate boiling regime.

At the critical heat flux, near the superheat limit of water ($\sim 300^{\circ}\text{C}$), droplet disintegration occurred purely from thermal break up with the explosive boiling force reaching a large maximum value. Morphological observations showed liquid surface roughening from the large nucleation rate of vapour with the residence time of the droplet being at a minimum. Further increases in surface temperature resulted in the droplet progressing into transition boiling and a decrease in explosive boiling due to intermittent liquid contact with the surface. A delay in thermal detonation was observed with inertial effects being re-introduced into droplet break up.

Once film boiling was established ($\sim 450\text{-}500^{\circ}\text{C}$) a vapour layer cushion severely reduced the ability of vapour bubble collapse from rupturing the liquid layer. As a result thermal break up was greatly suppressed and explosive boiling reached near zero values. Morphological analyses showed the droplet breaking up under inertial related influence as the droplet spread and recoiled atop the vapour layer. Subsequent peaks in explosive boiling were attributed to oxide layer formation.

Secondary droplet characteristics scaled with explosive boiling force. Greater force resulted in violent disintegration of the initial droplet where secondary droplet counts and ejected distribution areas increased while sizes decreased. At the critical heat flux, droplet counts and distributed areas were at a maximum while sizes were at a minimum. The progression into transition and film boiling resulted in secondary droplets counts and distributed area to decrease while sizes increased again. The results suggest that secondary droplet characteristics were insensitive to an inertial break up mechanism and instead scaled with the thermal effects of the boiling mode present.

Varying the thermal diffusivity of an impact surface on droplet impacts was also studied. Quicker progression to the different boiling modes was noted with a large thermal diffusivity compared to a lower one. A timescale influence was noted from morphological impacts where quicker initiation of thermal break up and quicker formation of a vapour layer occurred on the high thermal diffusivity surface at a given initial temperature. Thermal diffusivity affects the deposition rate of heat into the droplet and thus shows great influence when thermal break up is present. The effect of thermal diffusivity was the most prominent on explosive boiling force and secondary droplet characteristics in the superheat limit temperature region only. An increase in thermal diffusivity resulted in a larger explosive boiling force. Additionally, secondary droplet sizes decreased with the counts and vertical ejection heights increased with a higher diffusivity surface than a lower one.

Varying the surface shape between a curved and flat surface only affected the spreading dynamics of the droplet after impact. A curved surface promotes quicker and greater spreading of a droplet that allows increased interfacial area for heat transfer. This effect was especially noticeable near the superheat limit to the film boiling regime where the curved brass surface showed slightly higher explosive boiling force compared to the flat surface. Secondary droplet counts, size and trajectory were unaffected by surface shape.

The results of this study can be used to build the knowledge base of droplet interactions with hot surfaces. Droplet impact morphology with secondary droplet analyses over a wide range of temperatures provides visualization and characterizations of impact outcomes similar to those encountered during quench cooling processes. Specifically, the temperature region of the superheat limit is of particular interest for nuclear reactor accidents given the explosive boiling force produced. Explosive boiling force estimations provide insight to the mechanical energy that is exerted on external structures during accident scenarios and can be used in the development of nuclear reactor safety design and methodology.

Chapter 7: Recommendations

From the present study, the complexity of studying and understanding the mechanisms of explosive boiling from a single droplet impact on a heated surface are numerous. Given that explosive boiling interactions involve several phenomena rooted in fluid dynamics, heat transfer, liquid atomization, and superheating, certain phenomena can be suppressed in favour of studying others. Careful experimental design and testing procedures are therefore required to investigate specific phenomena. Using the experimental design, observations and results in this study as a contribution to understanding explosive boiling, recommendations for future studies will be suggested.

In terms of experimental equipment, high-speed cameras capable of high resolutions and high frame rates are ideal for droplet impacts given the necessity of visualizing droplets of small size and the relative time scale of micro-seconds which impact phenomena develop. The possibility of using a second overhead camera to visualize impact sequences can help identify interactions at the liquid-solid interface. Preference should also be given to cameras with CCD (charge coupled device) light sensors given their ability to produce high quality images with minimal background noise. In comparison, the high-speed camera used in this study featured a CMOS (complementary metal oxide semiconductor) light sensors and is susceptible to larger amounts of background noise. Improvements to droplet measurement techniques include the use of Phase Doppler Anemometry (PDA), also known as Particle Dynamics Analysis, is relevant for secondary droplet analyses on size, count, velocity and distribution. PDA analyses offer greater distribution of detectable droplets sizes, specifically micro-metric sizes that can be measured with high precision.

Using a two dimensional transient heat conduction analysis can make improvements to the heat flux model. The contact area through which heat travels into the droplet is a dynamic property as the droplet spreads or recoils on the surface after initial impact and should be reflected in the heat transfer model. Given that the range of test surface temperatures extends to 700°C, consideration to radiation heat transfer should be accounted for and to include surfaces that are highly polished with certain degrees of surface oxidation. Improvements to heat transfer model translates to better estimation of the explosive boiling force. Further refinement of the explosive boiling force estimation can be made by providing improvements to the terms in the energy balance equation around the droplet. Additional considerations in the energy balance include; the energy used to sustain the vapour film layer during film boiling and the heat transfer through the vapour layer to the liquid. This involves the empirical estimation of the heat transfer coefficient of the vapour layer.

Analyzing the microstructure of the boiling surface offers insight into the surface characteristics that influence droplet impact outcomes with boiling effects. Surface spectroscopy offers investigation of chemical adsorption, surface chemical composition and chemistry. Surface microscopy techniques can visualize surface features such roughness, deformations and oxidation scale formation. These features affect the wettability, cavity size, shape and distribution of nucleation sites from which vapour bubbles are generated. The influence of surface features extends to vapour bubble generation and hence heat transfer rates in the liquid.

Recommendations for future study that extends the work in this present study should aim to:

- Study explosive boiling on a surface specific to nuclear reactor fuel sheath material (Zr-2.5%-Nb composition)
- Study the effect of initial droplet sub-cooling on explosive boiling force
- Study the effect of varying initial droplet properties such as density, surface tension and viscosity
- Study the effect of varying initial droplet velocity on explosive boiling
- Study the effect of surface roughness on explosive boiling
- Study the effect of surface oxidation on explosive boiling
- Study the effect sequential impacts of multiple droplets on explosive boiling
- Study the effect of simultaneous multiple droplet impacts on different surface locations on explosive boiling
- Evaluate the advancing velocity of spreading or recoil of a droplet after impact with a surface
- Develop empirical correlations for explosive boiling force with respect to varied parameters of surface temperature, thermal diffusivity and surface curvature

Bibliography

Akhtar, S. W., & Yule, A. J. (2001). Droplet Impaction on a Heated Surface at High Weber Numbers. *In: Proc of the ILASS-Europe*. Zurich.

Araki, K., & Moriyama, A. (1982). Deformation Behaviour of a Liquid Droplet Impinging on a Hot Metal Surface. *2nd ICLASS*, 389-396.

Arcoumanis, C., Whitelaw, D. S., & Whitelaw, J. H. (1997). Gasoline Injection Against Surfaces and Films. *Atom Sprays*, 7, 437-456.

Avedisian, C. T. (1985). The Homogeneous Nucleation Limits of Liquids. *J. Phys. Chem. Data*, 14, 695-742.

Bernardin, J. D., Stebbins, C. J., & Mudawar, I. (1997). Effects of Surface Roughness on Water Droplets Impact History and Heat Transfer Regimes. *International Journal of Heat and Mass Transfer*, 40, 73-88.

Blander, M., & Katz, J. L. (1975). Bubble Nucleation in Liquids. *AIChE J.*, 21, 833-848.

Borishansky, V. M. (1953). Heat Transfer to a Liquid Freely Flowing Over a Surface Heated to a Temperature Above the Boiling Point. *Problems of heat transfer during a change of state (e. S.S. Kutateladze)*, 109-144.

Coassali, G. E., Marengo, M., & Santini, M. Multiple Drop Impacts on Heated Surface. *Proceeding of the 9th International Conference Liquid Atom and Spray Systems* (p. 2003). Sorrento, Italy: ICLASS-2003.

Cossali, G. E., Marengo, M., & Santini, M. (2005). Secondary Atomisation Produced by Single Droplet Vertical Impacts onto Heated Surfaces. *Experimental Thermal and Fluid Science*, 29, 937-946.

Cossali, G. E., Marengo, M., Santini, M., & Fest, S. (2006). Effect of Wall Effusivity on Thermally Induced Secondary Atomisation of Single Drop Impacting onto a Tilted Surface. *ICLASS-2006*. Kyoto, Japan.

Cossali, G. E., Marengo, M., Santini, M., & Watanabe, J. (2002). Secondary Droplet Atomisation from Single Drop Impact on Heated Surfaces. *ILASS-Europe*. Zaragoza.

Cronenberg, A. W. (1980). Recent Developments in the Understanding of Energetic Molten Fuel-Coolant Interactions. *Nucl. Safety*, 21, 319-337.

Fletcher, D. F., & Theofanous, T. G. (1997). Heat Transfer and Fluid Dynamic Aspects of Explosive Melt-Water Interactions. *Advances in Heat Transfer*, 29, 129-213.

Fujimoto, H., Oku, Y., Ogihara, T., & Takuda, H. (2010). Hydrodynamics and Boiling Phenomena of Water Droplets Impinging on Hot Solid. *International Journal of Multiphase Flow*, 26, 62-642.

Glod, S., Poulikakos, D., Zhao, Z., & Yadigaroglu, G. (2002). An Investigation of Microscale Explosive Vapourization of Water on an Ultrathin Pt Wire. *International Journal of Heat and Mass Transfer*, 45, 367-379.

Gradeck, M., Seiler, N., Ruyer, P., & Maillet, D. (2013). Heat Transfer for Leidenfrost Drops Bouncing onto a Hot Surface. *Experimental Thermal and Fluid Sciences*, 47, 14-25.

Inada, S., & Yang, W. J. (1996). Mechanisms of Miniaturization of Sessile Drops on a Heated Surface. *International Journal of Heat and Mass Transfer*, 6, 1505-1515.

Incropera, F., & DeWitt, D. (2002). *Introduction of Heat Transfer*, 4th ed. Toronto, Ontario, Canada: John Wiley & Sons.

Jourhara, H., & Axcell, B. P. (2009). Film Boiling Heat Transfer and Vapour Film Collapse on Spheres, Cylinders and Plane Surfaces. *Nuclear Engineering and Design*, 239, 1885-1900.

Kudryashov, S. I., & Allen, S. D. (2006). Submicrosecond Dynamics of Water Explosive Boiling and Lift-Off from Laser-Heated Silicon Surfaces. *Journal of Applied Physics*, 100.

Lee, H. S., & Merte, H. (1996). Spherical Vapour Bubble Growth in Uniformly Superheated Liquids. *International Journal of Heat and Mass Transfer*, 39, 2427-2447.

Liu, G., Morsi, Y. S., & Van Der Walt, J. P. (1998). A Mathematical Model to Predict Spray Cooling Heat Flux. *13th Australian Fluid Mechanics Conference*. Melbourne, Australia: Monash University.

Marin, E. (2007). The Role of Thermal Properties in Periodic Time-Varying Phenomena. *European Journal of Physics*, 28, 429-445.

- Moita, A. S., & Moreira, A. N. Characterization of Hydrodynamics and Heat-Transfer Processes of Drop Impacts Against Surface Enhanced Heated Targets as an Application to Microelectromechanical Cooling Devices. *6th International Conference on Multiphase Flow*, (p. 2007). Leipzig, Germany.
- Moita, A. S., & Moreira, A. N. (2009). Development of Empirical Correlations to Predict the Secondary Droplet Size of Impacting Droplets onto Heated Surfaces. *Experimental Fluids*, *47*, 755-768.
- Moita, A. S., Sauer, S., & Moreira, A. N. Secondary Atomization of Micrometric Fuel Droplets Impinging onto Heated Targets. *16th International Symposium on Applications of Laser Techniques to Fluid Mechanics*, (p. 2012). Lisbon, Portugal.
- Moreira, A. N., & Moita, A. S. (2007). Drop Impacts onto Cold and Heated Rigid Surfaces: Morphological Comparisons, Disintegration Limits and Secondary Atomization. *International Journal of Heat and Fluid Flow*, *28*, 735-772.
- Moreira, A. N., Moita, A. S., & Cossali, G. E. (2007). Secondary Atomization of Water and Isooctane Drops Impinging on Tilted Heated Surfaces. *Experimental Fluids*, *43*, 297-313.
- Moreira, A. N., Moita, A. S., & Pano, M. R. (2010). Advances and Challenges in Explaining Fuel Spray Impingement: How Much of Single Droplet Impact Research is Useful? *Process in Energy and Combustion Science*, *36*, 554-580.
- Negeed, E. R., Hidaka, S., Kohno, M., & Takata, Y. (2013). High Speed Camera Investigation of the Impingement of Single Water Droplets on Oxidized High Temperature Surfaces. *International Journal of Thermal Sciences*, *63*, 1-14.
- Nematollahi, M. R. (2008). Evaluation of Exerting Force on the Heating Surface Due to Bubble Ebullition in Subcooled Flow Boiling. *World Academy of Science, Engineering and Technology*, *17*.
- Nguyen, V. T., Furzeland, R. M., & Iipelaar, M. M. (1998). Rapid Evaporation at the Superheat Limit. *International Journal of Heat and Mass Transfer*, *31*, 1687-1700.
- Park, H. C., Byun, K. T., & Kwak, H. Y. (2005). Explosive Boiling of Liquid Droplets at Their Superheat Limits. *Chemical Engineering Science*, 1809-1821.
- Reid, R. C. (1983). Rapid Phase Transitions from Liquid to Vapour. *Advances in Chemical Engineering*, *12*, 105-208.

- Rein, M. (1993). Phenomena of Liquid Droplet Impact on Solid and Liquid Surfaces. *Fluid Dynamics Research*, 12, 61-93.
- Richter, B., Dullenkopf, K., & Bauer, H. J. (2005). Investigation of Secondary Droplet Characteristics Produced by an Isooctane Drop Chain Impact onto a Heated Piston Surface. *Experiments in Fluids*, 39, 351-363.
- Rioboo, R., Tropea, C., & Marengo, M. (2001). Outcomes from a Drop Impact on Solid Surfaces. *Atomization and Sprays*, 11, 155-165.
- Samenfink, W., Elsaber, A., Dullenkopf, K., & Wittg, S. (1999). Droplet Interaction With Shear-Driven Liquid Films: Analysis of Deposition and Secondary Droplet Characteristics. *International Journal of Heat and Fluid Flow*, 20, 462-469.
- Shepherd, J. E., & Sturtevant, B. (1982). Rapid Evaporation at the Superheat Limit. *J. Fluid Mech.*, 121, 379-402.
- Shusser, M., & Weihs, D. (1999). Explosive Boiling of a Liquid Droplet. *International Journal of Multiphase Flow*, 25, 1561-1573.
- Sreekumar, K., & Vaidyan, V. K. (2007). Dual-reference Photothermal Imaging for the Estimation of Thermal Effusivity of Solids. *Measurement Science and Technology*, 18, 1939-1946.
- Takashima, T. (2008). Observations of Initiation Stage of Spontaneous Vapour Explosions for Droplet Scale. *Heat Transfer - Asian Research*, 37, 41-55.
- Trujillo, M. F., Matthews, W. S., Lee, C. F., & Peters, J. E. (2003). Experimental Investigations of Spray/Wall Impingement. *Atom Sprays*, 13, 223-242.
- Viscorova, R., Scholz, R., Spitzer, K. H., & Wendelstorf, J. (2006). Spray Water Cooling Heat Transfer Under Oxide Scale Formation Conditions. *9th International Conference of Advanced Computational Methods and Experimental Measurements in Heat and Mass Transfer*. New Forest, UK.
- Wahcters, L. J., & Westerling, N. J. (1966). The Heat Transfer from a Hot Wall to Impinging Water Droplets in the Spheroidal State. *Chem Eng Sci*, 21, 1047-1056.
- Wahcters, L. J., Smulders, L., Vermeulen, J. R., & Kleiweg, H. C. (1966). The Heat Transfer From a Hot Wall to Impinging Mist Droplet in the Spheroidal State. *Chemical Engineering Science*, 21, 1231-1238.

- Wan, Y., Wang, X., Sun, H., Li, Y., Zhang, K., & Wu, Y. (2012). Corrosion Behavior of Copper at Elevated Temperature. *Int. J. Electrochem. Sci.*, 7, 7902-7914.
- Wang, A. B., Lin, C. H., & Cheng, C. C. (2005). Pattern Analysis of a Single Droplet Impinging onto a Heated Plate. *Heat Transfer - Asian Research*, 34.
- Watanabe, H., Suzuki, Y., Harada, T., Matsushita, Y., Aoki, H., & Miura, T. (2010). An Experimental Investigation of the Breakup Characteristics of Secondary Atomization of Emulsified Fuel Droplet. *Energy*, 35, 806-813.
- Wendelstorf, R., Spitzer, K. H., & Wendelstorf, J. (2008). Effect of Oxide Layers on Spray Water Cooling Heat Transfer at High Surface Temperatures. *International Journal of Heat and Mass Transfer*, 51, 4892-4901.
- Yarin, A. L., & Weiss, D. A. (1995). Impact of Drops on Solid Surfaces: Self-Similar Capillary Waves and Splashing as a New Type of Kinematic Discontinuity. *Journal of Fluid Mechanics*, 283, 141-173.
- Yushen, D., Zhilgilei, L. V., Winograd, N., & Garrison, B. J. (2001). Explosive Boiling of Water Films Adjacent to Heated Surfaces: A Microscopic Description. *J. Phys. Chem.*, 105, 2748-2755.
- Zhao, Z., Glod, S., & Poulikakos, D. (2000). Pressure and Power Generation During Explosive Vapourization on a Thin-Film Microheater. *International Journal of Heat and Mass Transfer*, 43, 281-296.
- Zhilin, V. G., Zeigarnik, Y. A., Ivochkin, Y. P., Oksman, A. A., & Belov, K. I. (2009). An Experimental Investigation of the Characteristics of Explosive Boiling of Subcooled Water on a Hot Surface Under Conditions of Change of Boiling Modes. 47, 856-663.

Appendix A

A1: Image Processing

ImageJ reports measurements of objects in an image in pixel lengths. The pixel length of an object whose distance was previously known was used to determine the scale on an SI unit basis. The pixel conversions to SI units are shown in **Table A.1** for each surface material. The analyses for secondary droplets were carried out using these ratios for all temperatures of that specific surface material.

Table A.1 – Pixel to length ratios of objects in images analyzed by ImageJ

Specimen Material	Pixel-to-Length Ratio [pixels/cm]
Copper Hemisphere	57.2
Stainless Steel Hemisphere	54
Brass Hemisphere	53
Brass Plate	57

A2: Experimental Equipment Details

Item	Supplier	Description/Specifications
Specimen System		
Thermocouples	Omega	Type: K Style: Quick Disconnect Mini Sheath: Inconel 600 Length: 24” Diameter: 0.040” Junction: Ungrounded Maximum deviation: $\pm 0.8^{\circ}\text{C}$ at 650°C
Thermocouple Extension Wire	Omega	PFA Coated Wire Extension Cable for K-type thermocouples Length: 25’
Brazing/Flux material	LucasMilhaupt	Braze051 Brazing Material Composition: Silver $5.0\% \pm 0.5\%$ Copper $58.0\% \pm 1.0\%$ Zinc $37.0\% \pm 1.0\%$

Brazing/Flux material (continued)		Other Elements (Total) 0.15% Max Hi-Temp095 Flux Material Composition: Copper 52.5% ± 1.0% Nickel 9.5% ± 1.0% Manganese Remainder Other Elements (Total) 0.50% Max
Specimen Holding System	McMaster-Carr	Stainless Steel (Grade 304) - Refer to Figure A.1 for drawings and dimensions
Mounted Pillow Block Bearings	McMaster-Carr	Cast iron base-mounted babbitt-lined bearing, split for 1" shaft diameter
Stainless Steel (Grade 316) Specimens	Mr. Metal	Hemisphere: 2" OD, L = 2"
Copper (Grade 110) Specimens	Metal Supermarkets	Hemisphere: 2" OD, L = 2"
Brass (Grade 360) Specimens	Mr. Metal	Hemisphere: 2" OD, L = 2" Plate: 1" x 2" x 2"
Water Valve System		
Mariotte Siphon	Cognisys Inc.	Schedule 40 PVC clear pipe (12" length, 1" diameter) with 1/4" orifice
Solenoid Valve	STC Valve	2P025 Series Valve - 2 way, normally closed, direct acting - 2 mm orifice - 1/8" to 1/4" port size - 12V
Solenoid Valve Controller	StopShot from Cognisys Inc.	Electronic timing device that controls the water valve with selectable pulse width durations for single or multiple drop impacts
Nozzles	Home Depot	Brass body, hose barb adapters: - 1/4" barb x 1/4" connector (male) - 3/8" barb x 1/4" connector (male)
Quench tank	Metal Supermarkets	Three stainless steel sheets (4 ft x 8 ft) with wall thickness of 0.32 cm
Data Acquisition System		
DAQ (SCXI-1000)	National Instruments	Maximum sampling rate: 500kSamples/s
High Speed Imaging System		
High Speed Camera	Photron	FAST CAM-X PCI 1024 - Maximum resolution: 1 M pixel at 1000

High Speed Camera (continued)		fps - Maximum speed: 109,500 fps at 128x16 pixels - CMOS (complementary metal oxide semiconductor) light sensor
Camera Lens	HSI - High Speed Imaging	12.5 mm – 75 mm, F 1.8
Light Sources	Lowel	Halogen type
Furnace		
Furnace	PSH Kilns and Furnaces	Size: 92 cm x 92 cm x 92 cm box furnace, maximum temperature: 1000°C, 11 cm diameter port size for specimen holder
Software		
LabView	National Instruments	Version 8.5, single channel temperature data logging
PFV Viewer	Photron	Version 4, High-speed camera recording environment
ImageJ	National Institutes of Health, USA	Version 1.46r, Java based image processing for visual analyses

A3: Specimen Holder System Drawings

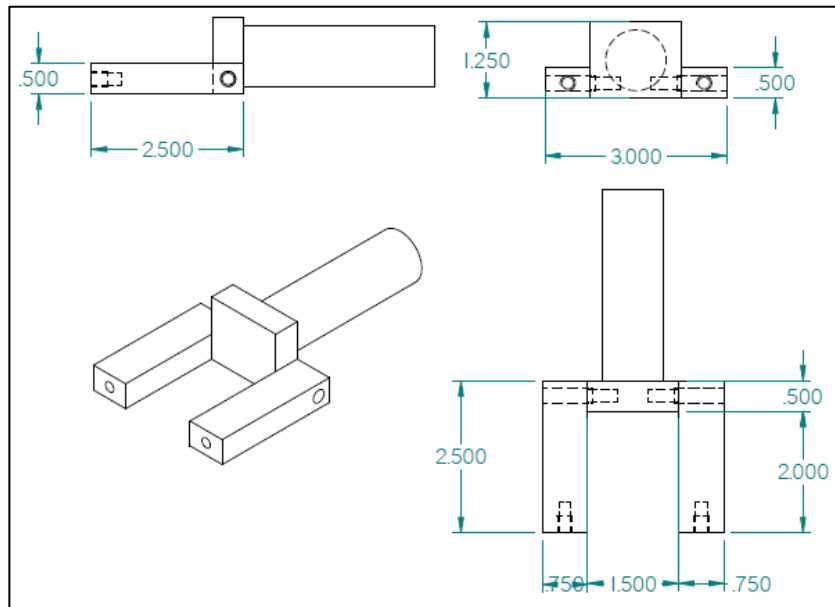


Figure A.1 – Design drawings of specimen holder system (dimensions reported in inches)

Appendix B – Raw Data

Table B.1 – Copper hemisphere raw data

T_s [°C]	k [W/m-k]	ρ [kg/m ³]	C_p [J/kg-K]	α [m ² /s]	t_i [s]	T_i [°C]	t_f [s]	T_f [°C]	t^* [s]	q'' [W/m ²]
100	395.149	8933	393.777	1.123E-04	0.761	100.14	2.426	99.682	1.665	7.47E+03
150	391.398	8933	399.289	1.097E-04	0.705	149.889	0.719	149.041	0.014	1.51E+05
200	387.874	8933	404.323	1.074E-04	0.778	200.225	0.785	199.449	0.007	1.96E+05
250	384.432	8933	409.24	1.052E-04	0.914	249.398	0.917	248.78	0.003	2.39E+05
300	380.888	8933	414.303	1.029E-04	0.741	300.025	0.7445	299.271	0.0035	2.70E+05
323	379.303	8933	416.567	1.019E-04	0.819	322.673	0.823	321.892	0.004	2.62E+05
350	377.495	8933	418.853	1.009E-04	0.737	350.161	0.741	349.441	0.004	2.41E+05
400	374.229	8933	422.872	9.907E-05	0.79	400.395	0.795	399.736	0.005	1.98E+05
450	371.131	8933	426.684	9.737E-05	0.76	448.055	0.769	447.055	0.009	2.24E+05
500	367.913	8933	430.656	9.564E-05	0.749	497.572	0.757	496.536	0.008	2.46E+05
550	364.676	8933	434.702	9.391E-05	0.817	545.908	0.824	544.73	0.007	2.99E+05
600	360.989	8933	439.443	9.196E-05	0.833	598.588	0.838	597.495	0.005	3.28E+05
650	357.431	8933	444.018	9.011E-05	1.653	649.419	1.659	648.108	0.006	3.60E+05
700	354.007	8933	448.42	8.838E-05	0.843	698.33	0.851	696.749	0.008	3.76E+05

Table B.2 – Stainless steel hemisphere raw data

T_s [°C]	k [W/m-k]	ρ [kg/m ³]	C_p [J/kg-K]	α [m ² /s]	t_i [s]	T_i [°C]	t_f [s]	T_f [°C]	t^* [s]	q'' [W/m ²]
100	14.718	8238	494.354	3.614E-06	0.756	100.14	6.4	97.644	5.644	4.59E+03
150	15.554	8238	509.252	3.708E-06	0.788	149.836	2.257	140.384	1.469	3.55E+04
200	16.328	8238	520.744	3.806E-06	0.777	199.798	1.999	177.482	1.222	9.53E+04
250	17.107	8238	532.29	3.901E-06	0.735	250.002	0.743	246.84	0.008	1.73E+05
300	17.879	8238	543.748	3.991E-06	0.922	299.817	0.928	295.979	0.006	2.50E+05
323	18.241	8238	549.12	4.032E-06	0.846	323.174	0.8515	319.887	0.0055	2.27E+05
350	18.645	8238	552.988	4.093E-06	0.771	349.988	0.777	346.629	0.006	2.25E+05
400	19.396	8238	559.495	4.208E-06	0.696	400.038	0.701	398.252	0.005	1.35E+05
450	20.133	8238	565.887	4.319E-06	0.715	449.211	0.721	447.393	0.006	1.28E+05
500	20.859	8238	572.181	4.425E-06	0.758	497.622	0.764	496.114	0.006	1.09E+05
550	21.635	8238	579.007	4.536E-06	0.742	550.13	0.755	547.401	0.013	1.37E+05
600	22.313	8238	585.082	4.629E-06	0.67	596.864	0.678	595.168	0.008	1.11E+05
650	23.079	8238	591.95	4.733E-06	0.631	649.694	0.635	648.425	0.004	1.20E+05
700	23.896	8238	599.276	4.840E-06	0.816	706.046	0.822	704.156	0.006	1.50E+05

Table B.3 – Brass hemisphere raw data

T_s [°C]	k [W/m-k]	ρ [kg/m ³]	C_p [J/kg-K]	α [m ² /s]	t_i [s]	T_i [°C]	t_f [s]	T_f [°C]	t^* [s]	q'' [W/m ²]
100	129.76	8530	390.978	3.891E-05	0.974	100.185	5.027	98.302	4.053	1.10E+04
150	138.384	8530	398.46	4.071E-05	0.971	150.069	1.016	148.94	0.045	6.51E+04
200	141.371	8530	405.928	4.083E-05	0.752	199.853	0.761	198.716	0.009	1.50E+05
250	144.364	8530	413.409	4.094E-05	0.818	249.725	0.823	248.824	0.005	1.62E+05
300	147.367	8530	420.918	4.104E-05	0.82	299.787	0.823	299.139	0.0035	1.54E+05
323	148.698	8530	424.245	4.109E-05	0.836	321.964	0.84	320.97	0.004	2.06E+05
350	150.405	8530	428.513	4.115E-05	1.094	350.423	1.099	349.413	0.005	1.89E+05
400	153.366	8530	435.915	4.125E-05	0.883	399.768	0.892	398.958	0.009	1.15E+05
450	156.276	8530	443.191	4.134E-05	0.781	448.273	0.791	447.572	0.01	9.61E+04
500	159.254	8530	450.636	4.143E-05	0.787	497.908	0.797	496.798	0.01	1.55E+05
550	162.392	8530	458.479	4.152E-05	0.773	550.192	0.7825	548.896	0.0095	1.89E+05
600	165.191	8530	465.478	4.160E-05	0.833	596.855	0.843	595.424	0.01	2.07E+05
650	168.253	8530	473.133	4.169E-05	0.605	647.884	0.615	646.246	0.01	2.41E+05
700	171.075	8530	480.187	4.177E-05	0.676	694.911	0.686	693.397	0.01	2.26E+05

Table B.4 – Brass plate raw data

T_s [°C]	k [W/m-k]	ρ [kg/m ³]	C_p [J/kg-K]	α [m ² /s]	t_i [s]	T_i [°C]	t_f [s]	T_f [°C]	t^* [s]	q'' [W/m ²]
100	129.857	8530	391.032	3.893E-05	0.863	100.544	6.4	99.124	5.537	7.09E+03
150	138.369	8530	398.422	4.071E-05	1.851	149.812	2.547	139.893	0.696	1.45E+05
200	141.372	8530	405.929	4.083E-05	0.819	199.861	0.828	198.657	0.009	1.58E+05
250	144.353	8530	413.383	4.094E-05	0.868	249.55	0.874	248.151	0.006	2.30E+05
300	147.471	8530	421.177	4.105E-05	0.815	301.509	0.819	300.738	0.004	1.58E+05
323	148.755	8530	424.369	4.109E-05	0.789	322.924	0.795	321.668	0.006	2.12E+05
350	150.34	8530	428.351	4.115E-05	0.835	349.338	0.847	348.063	0.012	1.54E+05
400	153.392	8530	435.98	4.125E-05	0.784	400.203	0.796	399.305	0.012	1.10E+05
450	156.252	8530	443.131	4.134E-05	0.846	447.87	0.862	446.538	0.016	1.44E+05
500	159.379	8530	450.948	4.143E-05	0.956	499.987	0.97	498.752	0.014	1.46E+05
550	162.179	8530	457.948	4.152E-05	1.705	546.652	1.717	545.198	0.012	1.88E+05
600	165.258	8530	465.644	4.161E-05	0.779	597.961	0.7895	596.388	0.0105	2.22E+05
650	168.45	8530	473.625	4.170E-05	0.769	651.169	0.781	649.302	0.012	2.51E+05
700	171.104	8530	480.261	4.177E-05	0.955	695.405	0.965	693.916	0.01	2.22E+05

Appendix C – Uncertainty Analysis

The main variables obtained from the experimental equipment are the temperature readings from the thermocouple and images from the high-speed camera. From these, quantities such as the heat flux, residence time, interfacial area, droplet diameter, droplet mass, droplet counts and position, to name a few, are calculated. The uncertainty from the obtained data as it progresses through calculated and estimated variables is discussed in the following sections and supports the results and discussion presented early in this study.

C1: Temperature

The removal process of a specimen from the furnace to a position underneath the water valve results in the temperature drop of the surface. As much as a drop of 15°C could be experienced in the 4 s it takes to remove the specimen from the furnace initially at 700°C. The actual temperature of the surface just before droplet impact is therefore always smaller than the desired surface temperature. This would skew the results, as the droplet would impact a surface at a lower temperature than expected. In order to accurately say that the droplet impacted a surface at the specified temperature, the specimen was heated slightly above the desired impact temperature in the furnace. That way, by the time the specimen was removed and cooled by the surroundings, its actual surface temperature was close to the desired one.

For example, by referring to **Table B.1** to **Table B.4**, for a desired surface temperature of $T_s = 300^\circ\text{C}$, the specimens were heated to approximately 304°C in the furnace prior to removal. The actual initial surface temperature (T_i), as taken from the raw measurement of the thermocouple, just before droplet impact was 300.025°C for the copper hemisphere, 299.817°C for the stainless steel hemisphere, 299.787°C for the brass hemisphere and 301.509°C for the brass plate. This gives an expected surface temperature of $300^\circ\text{C} \pm 1.5^\circ\text{C}$. Considering all surface temperatures for all specimens, the relative error is very small and only amounts to a maximum of $\pm 0.8\%$ for stated values of T_s in this present study. It should be noted that this uncertainty is eliminated in any calculations involving surface temperature. This is because the exact values, or raw thermocouple readings, are used in any subsequent calculations that require initial temperature.

Given that the thermocouple is at a depth of 1 mm from the droplet impact surface, the thermocouple readings are assumed to be the temperature of the impact surface at any given instant of time. Applying the lumped capacitance

method from Incropera et al. (2002), with a characteristic length of 1 mm, the Biot number is 0.0013. This implies that the temperature gradients in the within the solid, specifically the region from the impact surface to the thermocouple tip, are negligible. The delay time of the thermocouple responding to a temperature change is about 0.2 s. Within this time a surface may change up to $\pm 0.2^\circ\text{C}$. For high initial surface temperatures ($>400^\circ\text{C}$) the delay time was almost non-existent and temperature variations were minimal, as read by the thermocouple.

Concerning the interfacial temperature, based on the assumptions and model given in Equation (6), the raw thermocouple readings (T_i values), from **Table B.1** to **Table B.4**, were directly used to calculate T_{int} . The uncertainty in the interfacial temperature is therefore the deviation of the thermocouple junction plus the temperature deviation caused by the thermocouple response time. The deviation in the thermocouple junction, as reported by the manufacturer, is $\pm 0.8^\circ\text{C}$ (Appendix A2), giving a total of variance of $\pm 1.0^\circ\text{C}$. This uncertainty in the interfacial temperature could possibly be the difference in determining whether a droplet can attain the superheat limit temperature and explosively boil or not. However, the use of image sequences and quantification of secondary droplet properties can confirm whether an interfacial temperature is sufficient to result in explosive boiling and the degree of its intensity.

The thermocouple deviation factors into the heat flux (q'') calculation as well. However, referring to Equation (8), the greatest amount of uncertainty originated from the estimation of the droplet residence time on the surface, t^* . The next section describes the uncertainty associated with the residence time, as it was determined from high-speed camera images.

C2: High-Speed Imaging and Processing

The high-speed camera recorded images at a frequency of 1000 images/s with a resolution of 0.001 s in the time domain. This indicates that in a given frame, the time mark will have an absolute error of $\pm 5 \times 10^{-4}$ s. At the superheat limit where the droplet boils the most explosively, at a surface temperature of roughly 300°C in this study, the residence time is the shortest at 3 ms. The relative error is therefore the largest at this temperature and amounts to $\pm 17\%$. Residence times increase for surface temperatures where impacts are known to deviate away from explosive boiling conditions. The error for those surface temperatures is therefore known to decrease. For example, for 150°C and 700°C the relative error amounts to $\pm 0.1\%$ and $\pm 5.9\%$ respectively for the droplet residence time.

In the estimation of heat flux, the residence time gives the largest uncertainty at a surface temperature of 300°C for all specimens. Given the short nature of droplet

contact with the surface at this temperature, heat flux can vary as much as $\pm 1.7 \times 10^4 \text{ W/m}^2$ or alternatively, $\pm 8.5\%$. For larger residence times, the uncertainty in the time domain lessens which then translates to a lower uncertainty in the heat flux. The uncertainty in the heat flux is still relatively small due to the residence time being square rooted in Equation (8).

Through image processing, described in Section 4.1, background noise accounted for less than $\pm 1\%$ relative error in droplet identification by the software at surface temperatures below 150°C . A low error is encountered here since droplets are large and clearly distinguishable. However, the error increases once surface temperatures reach 150°C and above due to the increased intensity of atomization that creates very small sized droplets, detectable only with the aid of image processing. The background noise for surface temperatures $\geq 150^\circ\text{C}$ ranged from, on average; ± 6 droplets for less intense atomization impacts (150°C & $\geq 500^\circ\text{C}$) to ± 15 droplets for intense atomizations ($200\text{-}450^\circ\text{C}$). This results in an increase to almost $\pm 10\%$ relative error in droplet counts for more energetic impacts.

Given the optical limitations of the high-speed camera and image processing techniques in this study, droplets with sizes less than 0.2 mm in diameter were not detectable. The effect of their absence on the propagation of uncertainty to secondary droplet property measurements and explosive boiling force was difficult to determine. Some insight can be gained by plotting the detectable distribution of droplet sizes by ImageJ in a log histogram as seen in **Figure C.1**.

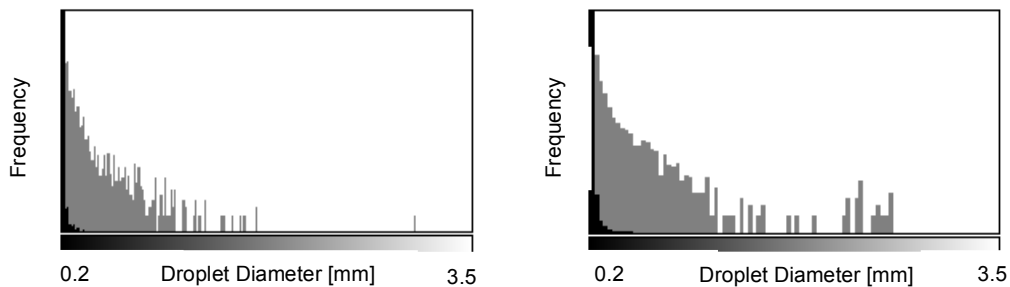


Figure C.1 – Histogram of detectable droplet sizes for surfaces; stainless steel hemisphere at 300°C (left), copper hemisphere at 700°C (right)

From **Figure C.1**, the detectable range of droplet sizes follows a half-normal distribution, specifically the right side of a normal distribution. Assuming that atomization does in fact produce a full normal distribution of droplet sizes, the left side of the normal distribution appears to be missing from the figures above. The left side of the normal distribution would therefore represent the droplet sizes

smaller than 0.2 mm that were not detected in the experiment. It is not clear in what percentage the detected droplet shown above represents the full spectrum of droplets sizes.

The droplet size distributions obtained in the study by Moreira et al. (2007) showed that droplet sizes were positively skewed in the normal distribution. Their setup allowed for a greater range of droplet size detection than this present study. When one considers the limitations of high-speed cameras and detection techniques, there is always a limit to the smallest size detectable. In addition, as the range of detectable sizes becomes smaller, the probability of more background noise being produced is increased. Therefore a slightly, positively skewed normal distribution of sizes is expected. Though the distribution of detectable droplet sizes represented above is only a portion of the full droplet size spectrum, trends in secondary droplet counts, sizes and position were obtained successfully. Authors such as Cossali et al. (2006), Moita et al. (2012), Moreira et al. (2007) and Richter et al. (2005) have also drawn insightful results given the limitations of imaging in their studies. Secondary properties as they vary with surface temperature, thermal diffusivity and surface shape can be quantified given the detectable range of droplets from the equipment in this present study and are discussed previously in Section 5.4.

The uncertainty in the secondary droplet counts includes background noise particles and surface reflection effects and amounts to roughly $\pm 10\%$. Surface reflection effects are minimal since maximum droplet counts are reported in this study and occur in time where majority of the droplets are well developed and have moved away from the specimen surface.

The uncertainty associated with the size of the droplets that are detectable is a result of the image processing software interpreting the spherical nature of a droplet. Since light reflection off droplets can be non-uniform, they appear non-circular to the imaging software. Corrections were made to represent their shape as perfect spheres. The error of this correction was most prominent for impacts where larger droplet sizes were created. For example, a stainless steel hemisphere at 400°C can have as many as ± 78 droplets that are corrected. Averaging for all surfaces and temperatures gives an uncertainty of approximately $\pm 13\%$.

Secondary droplet position was the most accurately tracked property and was dependent on the resolution and image processing power of the computer used. In general, the maximum deviation of the centroid of a droplet on an x-y coordinate system was ± 0.175 mm. Translating this to estimated distances the droplets have away from the origin of the coordinate scale, the error is quite small at $\pm 2.2\%$. This uncertainty is also associated with the error in making length measurements of objects in a given image using ImageJ.

C3: Explosive Boiling

In the evaluation of the vapour mass flux from Equation (15), restated below, the largest uncertainty lies with the determination of the liquid mass flux, \dot{m}_L .

$$\dot{m}_v = \frac{q'' - \dot{m}_L C_{p,liq}(T_{sat} - T_d)}{h_{fg} + C_{p,vap}(T_{vap} - T_{sat})} \quad (15)$$

The liquid mass flux calculation was dependent on the masses of the droplets. Specifically, the mass of the droplet before impact and the total mass of secondary droplets just after the moment they evacuate the surface (i.e., leave the region of the thermocouple). The initial droplet mass was easily measured by ImageJ since its size was fixed and large enough to detect. The uncertainty lies in the total secondary droplet mass created due to atomization since a portion of the droplet size distribution is missing, as discussed in Section C2 of Appendix C.

In order to understand the error associated with post impact masses, a mass conservation balance around the event of a droplet impact and atomization is considered first. The initial mass of liquid as it interacts with a hot surface is transformed in to vapour mass and the remaining liquid mass are the secondary droplets. It is necessary to include the mass of the droplets that are undetected by the experimental equipment as well. The overall mass balance is shown below as Equation (18).

$$m_{liq,before} = m_{liq,after} + m_{vap} + m_{miss} \quad (18)$$

The total mass of the initial droplet before impact is $m_{liq,before}$ and is equal to the total mass of the secondary droplets evolved after impact, $m_{liq,after}$, plus the mass of evolved vapour, m_{vap} , plus the mass of missing droplets, m_{miss} . Only the mass of the missing droplets is unknown and is the bulk source of error in determining mass values for vapour and total secondary droplets. Respectively. The error in mass estimations is expected to be the largest at the superheat limit. This is because atomization is the most intense and creates a large amount of small sized droplets that can potentially fall outside the detectable limit of the equipment. For a brass hemisphere surface at 300°C, the total mass of secondary droplets and vapour was calculated to be 1.46×10^{-5} kg and 6.39×10^{-6} kg respectively. For a fixed initial droplet mass of 6.53×10^{-5} kg, the error resulting from the missing droplets amounts to $\pm 67\%$. For surface temperatures that result in less intense vapour explosions, the change in the mass before and after the impact is reduced. For example, a copper hemisphere at 500°C, the error in the mass amounts to $\pm 12\%$.

Ultimately, the uncertainty in the mass is the one that is dominant and propagates to the estimation of explosive boiling force. The uncertainty in the estimation of acceleration of the secondary droplets is related back to the positional error of associated with ImageJ tracking. The positional error, mentioned above, was only $\pm 2.2\%$ with almost no uncertainty in the time domain due to the relative nature of tracking the position-time combination from one frame to another. Droplet trajectories were tracked as early as possible from the point in which they ejected from the bulk liquid mass. This ensures the droplet's trajectory is one that is experiencing acceleration and not deceleration which occurs at the end of a droplet's parabolic flight path. Given difficulties in tracking droplets manually from background noise or interference from neighboring droplets, the uncertainty in acceleration was estimated to reach as high as $\pm 10\%$. Visual images provided the best source to compare droplet escape accelerations. Especially for intense explosive boiling events, the escaping secondary droplet velocities are well captured. It is only until less violent boiling is encountered in film boiling impacts where surface temperature variations produce visually similar droplet escape velocities.

The resultant uncertainty in combining the vapour mass and droplet acceleration can vary greatly depending on the surface temperature. Collectively the biggest uncertainty occurs for the explosive boiling force near the superheat limit temperature. A droplet explosively boiling on a copper hemisphere surface at 300°C can reach a disintegrating force of $3.93 \times 10^{-3} \text{ N} \pm 1.9 \times 10^{-3} \text{ N}$. Less uncertainty was encountered for droplets with a near zero boiling force, typically around 150°C , with a relative error of $\pm 10\%$. Taking an overview of estimates, uncertainties for explosive boiling force are usually $\pm 40\text{-}50\%$ near the superheat limit and are $\pm 30\%$ for impacts occurring in the transition or film boiling regime temperatures. With the addition of supporting images sequences and image-processed sequences of droplet impacts, both sets of data; quantified values and visual analyses; gives a solid basis from which to draw the main findings of this study.

C4: Repeatability Analysis

This section gives analysis on the repeatability of key measurements of in this study. Droplet impacts were repeated for instances where impact conditions were less than ideal. Such events included; multiple droplets being released from the valve, undersized or oversized initial droplets, the droplet not impacting perpendicular to the surface, temperature transients not being recorded by the thermocouple, or distorted high-speed camera images. The repeatability of key variables was excluded in the findings and analyses presented in the results and discussion section in favour identifying clear trends with surface temperature, thermal diffusivity and surface shape.

The quantification and discussion of repeatability of key measurements of force is presented here. The explosive boiling force curve shown in **Figure C.2** includes the repeat measurements that were performed in this study.

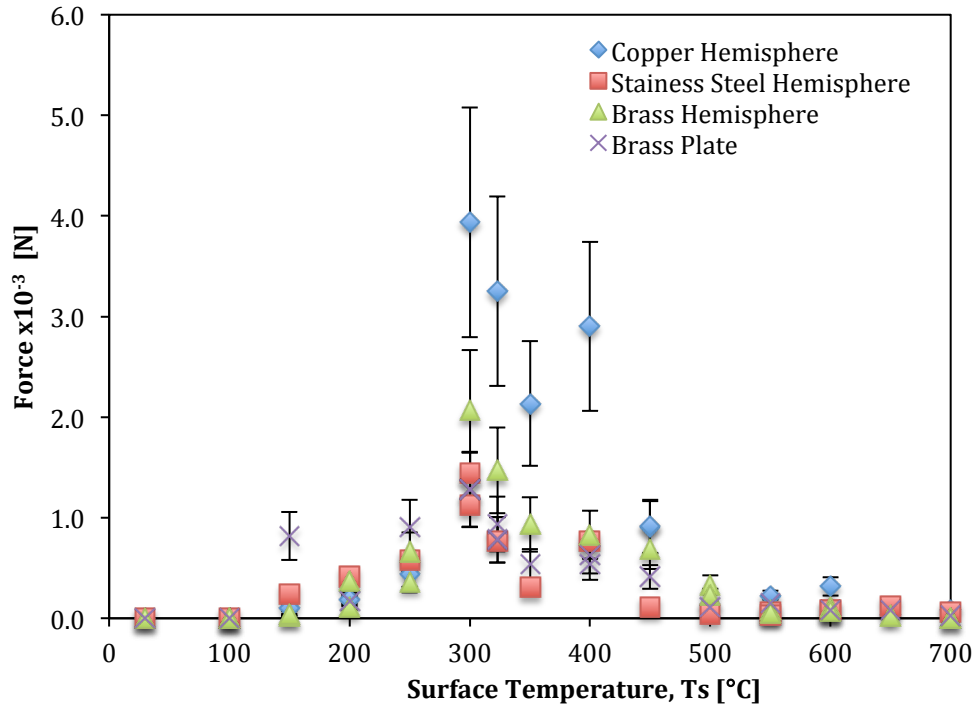


Figure C.2 – Explosive boiling force of a water droplet with repeat measurements

The difference in the explosive boiling force at a given surface temperature is attributed to variances in instrumentation and methodology of obtaining and analyzing the repeat measurements. An analysis of variances (ANOVA) was applied to the data set concerning force calculations. Repeatability is concerned with the difference in the boiling force values within a specific surface temperature for a specific surface material. A maximum variance in the repeatability was determined to be 8.88×10^{-6} . This is a very small number in relation to the boiling force values shown in **Figure C.2**.

The mean squared values between the groups and within the groups were 0.5569 and 0.0042 respectively. The largest source of variations in these two numbers comes from the difference in force values between the different surface temperature and surface materials. 98% of the variances determined by the ANOVA analysis is due to the variances between the groups and suggests that the

experiments produced repeatable values in force. The pooled standard deviation of the repeatability in the force measurements was determined to be 6.5×10^{-5} .

Appendix D – Thermal Penetration Depth

This section gives an insight into the thermal gradient that is created within the body of liquid after it establishes contact with a heated surface. Treating the droplet as a semi-infinite body upon instantaneous contact with the surface, a one-dimensional, transient heat conduction model is applied to describe the temperature profile within the droplet as a function of position and time. This assumption is a useful idealization of the approximate transient response of a water droplet after encountering a hot solid surface.

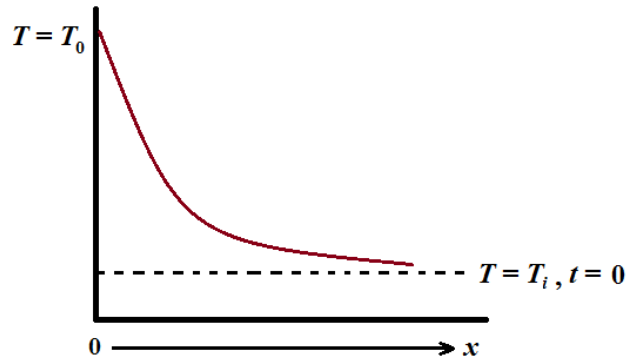


Figure D.1 – Heat conduction in a semi-infinite water droplet

The temperature distribution within the droplet is described in **Figure D.1**. A water droplet with a size ($x > 0$) is initially at a temperature T_i . At the instant the droplet impacts the heated surface at $t = 0$, a temperature increase is experienced in the liquid layers closest to the heated surface starting at $x = 0$. The temperature of the liquid far from the impact surface is unaffected and remains at a constant initial temperature. Assuming, no internal energy generation in the droplet and constant thermal conductivity, the governing heat diffusion equation is given as Equation (19) (Incropera et al., 2002).

$$\frac{\partial^2 T(x,t)}{\partial x^2} = \frac{1}{\alpha} \cdot \frac{\partial T(x,t)}{\partial t} \quad (19)$$

with boundary conditions:

$$T(x,t) = T_0 \quad x = 0, t = 0 \quad (20)$$

$$T(x,t) = T_i \quad x \Rightarrow \infty, t > 0 \quad (21)$$

$$T(x,t) = T_i \quad x > 0, t = 0 \quad (22)$$

The solution method involves using a separation of variables and the use of a similarity variable, defined as $\eta \equiv x/(4\alpha t)^{0.5}$ (Incropera et al., 2002). The similarity variable allows Equation (19) and its boundary conditions to be that of an ordinary differential equation. The result of the transformation becomes

$$\frac{d^2T}{d\eta^2} = -2\eta \frac{dT}{d\eta} \quad (23)$$

with $T(\eta = 0) = T_0$ and $T(\eta \Rightarrow \infty) = T_i$ as the boundary conditions. Integrating yields

$$\frac{dT}{d\eta} = C_1 \exp(-\eta^2)$$

Integrating a second time and applying a dummy variable, u yields

$$T = C_1 \int_0^\eta \exp(-u^2) du + C_2$$

Applying both boundary conditions and evaluating the definite integral will give the temperature distribution within the droplet as

$$\frac{T - T_0}{T_i - T_0} = \frac{2}{\pi^{0.5}} \int_0^\eta \exp(-u^2) du \equiv \text{erf } \eta$$

Replacing the similarity variable then gives the final form of the temperature distribution, Equation (24), which will be evaluated.

$$\frac{T(x,t) - T_0}{T_i - T_0} = \text{erf} \left(\frac{x}{\sqrt{4\alpha t}} \right) \quad (24)$$

Before applying Equation (24), some physical constraints are discussed first. From Section 5.1.1, both the heated solid and liquid droplet are treated as semi-infinite bodies coming in contact at $t = 0$. An instantaneous interface temperature is assumed and it follows that $T_0 = T_{int}$ at $x = 0$ for the droplet.

T_i is equal to the initial droplet temperature of 25°C. Since the liquid layers closest to the surface experience the temperature increase the most, liquid properties are therefore evaluated at the average fluid temperature; $T_{avg} = (T_{int} + T_i)/2$.

Given that nucleation rates during an explosive boiling event are very fast, the metastable state of the liquid layers closest to the surface exists for a very short period of time. The development of explosive boiling occurs in the first 100-200 μs (Shusser & Weihs, 1999). This value will provide better approximation in how far the temperature transient will penetrate into the droplet than the 1-3 ms of explosive boiling development time used in this current study. Lastly, the initial water droplet was 0.5 cm in diameter. This value represents that upper bound in thickness the droplet has upon contact with the solid surface.

The temperature distribution, $T(x,t)$, is plotted with respect to the position, x , within the liquid from the impact surface in the figures below. The temperature distribution profile represents the positional depth at which a heat penetrates into the liquid droplet.

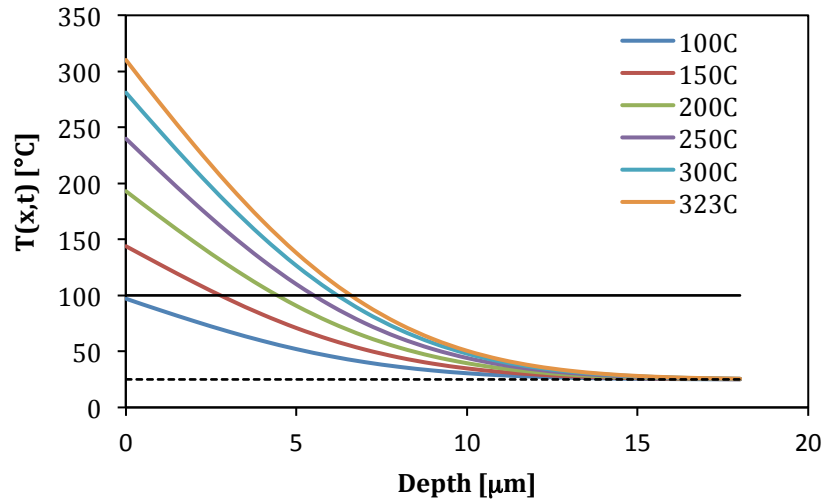


Figure D.2 – Temperature distribution in droplet for various initial surface temperatures (Copper surface, $t = 100 \mu\text{s}$)

Within a fixed time of 100 μs after the droplet first contacts the heated surface, the temperature profiles for various initial surface temperatures are shown and compared in **Figure D.2**. The horizontal dotted line at $T(x,t) = 25^\circ\text{C}$ represents the initial droplet temperature and shows that the temperature profiles all converge at a point 18 μm into the droplet. The solid horizontal line at $T(x,t) = 100^\circ\text{C}$ is the saturation temperature of liquid water at atmospheric conditions. Above this line, a superheated liquid is present in a metastable state. This liquid state exists up to a depth that is defined by the intersection point of the temperature distribution with the solid horizontal line. Comparisons show that the superheated metastable state exists at the greater depth in the droplet when the interface temperature is higher. For example, in **Figure D.2**, a droplet impacting a surface at 323 $^\circ\text{C}$, the

superheated layer exists up to a depth of 6.8 μm , however at 150°C it is only 2.8 μm .

This result shows that because of liquid water’s low thermal diffusivity that thermal energy from the solid surface only penetrates a few micrometers into the droplet and superheats a very small portion of liquid. The phase change occurring in the superheated layer is responsible for the explosive energy that violently disintegrates the rest of the liquid. It follows that droplets’ with an interface temperature within the spontaneous nucleation temperature, such as the ones occurring at 300°C or 323°C in **Figure D.2**, will possess a larger volume of liquid that is superheated and is permissible to transform into vapour.

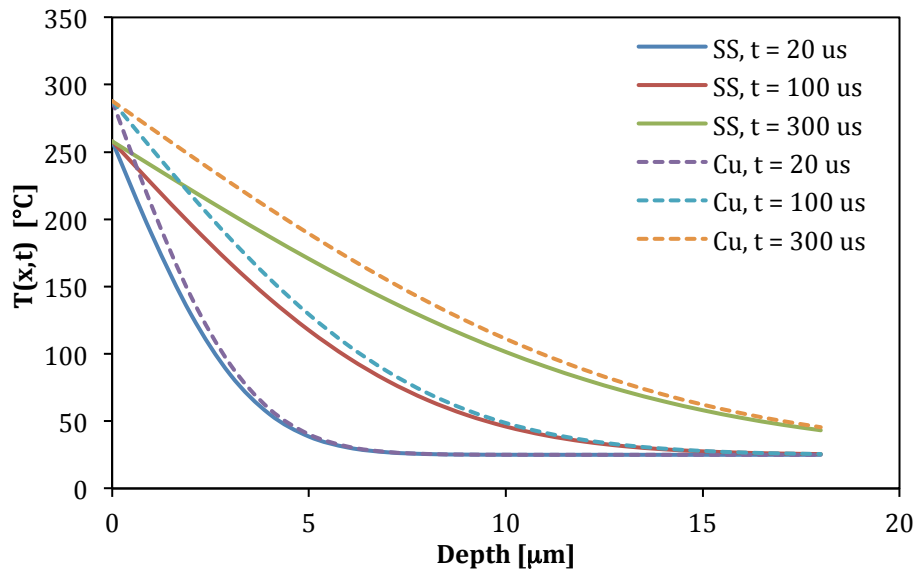


Figure D.3 – Temperature distribution for different surfaces and absorption times ($T_s = 300^\circ\text{C}$, SS – Stainless Steel, Cu – Copper)

The temperature profiles for surface temperatures above 323°C were excluded due to progression of the boiling mode into the transition and film boiling regimes. The presence of vapour acts as a thermal resistance barrier through which thermal energy transfer to the liquid is impeded. The investigation of temperature gradients thusly requires extension of the model to account for vapour layer thermal conductivity and thickness. This is reserved for future work.

The time dependence of the thermal penetration depth in the droplet is shown in **Figure D.3**. A larger time frame for the thermal energy to transfer through the droplet results in a larger portion of the liquid being superheated. A more intense vapour explosion would be expected in such a case. The time dependence of the

thermal energy deposition rate due to the difference in surface material appeared to be minor in **Figure D.3**. Only the water properties are considered in the temperature profiles equations with minor contribution of the impact surface material's properties in the form of the interfacial temperature. As a result, thermal diffusivity variations of the impact surface are less pronounced on the temperature profiles. The influence surface thermal diffusivity is much more evident in comparison to the explosive boiling force curve which shows a strong effect.